Reduced Dimensionality Transition State Theory with Multi-Dimensional Tunnelling



Yee Ching Kwan

St Edmund Hall

Department of Physical and Theoretical Chemistry

A thesis submitted for the degree of

Masters of Science by Research in Physical and Theoretical Chemistry

University of Oxford

Trinity 2016

Acknowledgements

I would like to thank my supervisor Professor Sir David Clary F.R.S for his patience, support, encouragement and guidance. I am also particularly thankful for Dr. Xiao Shan, for his scientific input, guidance, and unending patience during the course of these two years. I would also like to thank the current member of the Clary research group, Mr. Samuel Greene, for his help in answering the questions that I had about my research project, and also for his patience and friendship that have contributed to my joy being in Oxford. I would also like to thank Mr. Eyad Al-Samra for his generosity in sharing his knowledge and friendship in the research lab. Many thanks also goes to friends and family from Singapore who were in Oxford and London who made me feel at home as an international student.

Finally, I would like to thank God for His love and providence in all aspects of my life in Oxford, without which the completion of this thesis would not be possible.

Reduced Dimensionality Transition State Theory with Multi-Dimensional Tunnelling

Yee Ching Kwan, St Edmund Hall

A thesis submitted in partial fulfilment of the requirements for the degree of Master of Science by Research of the University of Oxford

Trinity Term, 2016

Abstract

Full-dimensional quantum reactive scattering (QRS) calculations provide the most accurate dynamical results which include the rate constants for a chemical reaction. However, the computational costs involved in the calculations scale significantly with the size of the reacting system. Transition State Theory with Multi-Dimensional Tunnelling (TST/MT) and Reduced Dimensionality (RD) methods are two methods that are more efficient in computing reaction rate constants for general polyatomic reacting systems. In RD methods, only a subset of degrees of freedom are treated explicitly in calculations. In TST/MT, reaction rate constants are obtained by multiplying the TST reaction rate constants with a transmission coefficient, calculated based on the adiabatic ground state potential energy and other relevant properties obtained along the minimum energy path.

In this thesis, TST with zero-, small-, and large-curvature tunnelling approximations (abbreviated as TST/ZCT, TST/SCT and TST/LCT respectively) were applied to previously constructed RD potential energy surfaces (RD PES) with and without a mapped interpolation (MI) procedure. They were applied to the reactions $CH_4 + H$, $C_2H_6 + H$, cyc-$C_3H_6 + H$, $CH_4 + CH_3$, $CH_3D + CH_3$ and $CD_4 + CD_3$ to test the TST/MT methods against accurate QRS calculations on the same PESs on these reactions. The use of MI improved the results by correcting the shape of the adiabatic ground state potential energy curves and the threshold energies of the reactions. TST/ZCT (MI) shows poor agreement with QRS results due to the lack of accounting for reaction path curvature, and TST/LCT (MI) shows moderate agreement for $CH_4 + CH_3$ with large reaction path curvature. For all reactions, TST/SCT (MI) shows the best agreement to QRS results and experimental data. Such agreement suggests the potential applicability of the TST/MT methods to larger polyatomic systems under the RD framework.

Primary kinetic isotope effects (KIE) for $CH_4 + CH_3$ are shown to be significant due to the substitution of the exchanged hydrogen atom with a much heavier deuterium isotope. Secondary KIE for $CH_3D + CH_3$ are shown to be less significant and do not contribute much to the reaction rate constants in the case of $CD_4 + CD_3$.

Contents

Contents **i**

1 Introduction **1**

2 Theory **13**

2.1 Classical Transition State Theory 13

2.2 Multi-Dimensional Tunnelling 15

2.2.1 Outline of Multi-Dimensional Tunnelling 16

2.2.2 Minimum Energy Path 16

2.2.2.1 Steepest Descent Path 17

2.2.2.2 Calculation of the Adiabatic Ground State Potential Energy Curve 19

2.2.3 Zero- and Small-curvature Tunnelling 22

2.2.4 Large Curvature Tunnelling 28

2.2.5 Mapped Interpolation 37

2.3 Reduced Dimensionality 41

2.3.1 Reduced Dimensionality Potential Energy Surfaces 41

2.3.2 Reduced Dimensionality-Adapted Calculations 43

3 Computational Details **47**

3.1 Reduced Dimensionality-Adapted Program 47

3.1.1 Transition State Properties 49

3.1.2 Minimum Energy Path 50

3.1.3 Reaction Rate Constants 51

3.2 Potential Energy Surfaces 52

4 Hydrogen Abstraction Reactions **55**

4.1 $CH_4 + H \longrightarrow CH_3 + H_2$ 56

4.1.1 Without Mapped Interpolation 56

4.1.1.1 Minimum Energy Path 56

4.1.1.2 Reaction Rate Constants 60

4.1.1.3 Cumulative Reaction Probability 62

4.1.2 With Mapped Interpolation 65

4.1.2.1 Minimum Energy Path 65

4.1.2.2 Cumulative Reaction Probability 66

4.1.2.3 Reaction Rate Constants 69

4.1.3 Summary for $CH_4 + H \longrightarrow CH_3 + H_2$ 71

4.2 $C_2H_6 + H \longrightarrow C_2H_5 + H_2$ 72

4.2.1 Without Mapped Interpolation 73

4.2.1.1 Minimum Energy Path 73

4.2.2 Reaction Rate Constants 76

4.2.3 Cumulative Reaction Probability 78

4.2.4 With Mapped Interpolation 79

4.2.4.1 Minimum Energy Path 79

4.2.5 Cumulative Reaction Probability 82
4.2.6 Reaction Rate Constants 84
4.2.7 Summary for $C_2H_6 + H \longrightarrow C_2H_5 + H_2$ 86
4.3 cyc-$C_3H_6 + H \longrightarrow$ cyc-$C_3H_5 + H_2$ 87
4.3.1 With Mapped Interpolation 87
4.3.1.1 Minimum Energy Path 87
4.3.2 Reaction Rate Constants 91
4.3.3 Summary for cyc-$C_3H_6 + H \longrightarrow$ cyc-$C_3H_5 + H_2$ 92
4.4 Conclusion for Hydrogen Abstraction Reactions 93

5 Hydrogen Exchange Reactions **95**

5.1 $CH_4 + CH_3 \longrightarrow CH_3 + CH_4$ 96
5.1.1 Transition State Theory with Small-Curvature Tunnelling 97
5.1.1.1 Minimum Energy Path 97
5.1.2 Transition State Theory with Large-Curvature Tunnelling 103
5.1.2.1 Minimum Energy Path 103
5.1.2.2 LCT Tunnelling Path 104
5.1.2.3 Reaction Rate Constants 107
5.1.3 Summary for $CH_4 + CH_3 \longrightarrow CH_3 + CH_4$ 111
5.2 $CH_3D + CH_3 \longrightarrow CH_3 + CH_3D$ 111
5.2.1 Minimum Energy Path 112
5.2.2 Reaction Rate Constants 116
5.2.2.1 Primary Kinetic Isotope Effect 118
5.2.3 Summary for $CH_3D + CH_3 \longrightarrow CH_3 + CH_3D$ 119
5.3 $CD_4 + CD_3 \longrightarrow CD_3 + CD_4$ 120

5.3.1 Minimum Energy Path 121
5.3.2 Reaction Rate Constants 124
5.3.2.1 Secondary Kinetic Isotope Effect 126
5.3.3 Summary for $CD_4 + CD_3 \longrightarrow CD_3 + CD_4$ 127
5.4 Conclusion for Hydrogen Exchange Reactions 128

6 Conclusion **129**

Bibliography **133**

The abbreviations used in this thesis are presented here.

BS	Basis Set
CD-SCSAG	Centrifugal Dominant Small-Curvature Semi-Classical Adiabatic Ground State
CMD	Centroid Molecular Dynamics
CVTST	Canonical Variational Transition State Theory
HLH	Heavy-Light-Heavy
KIE	Kinetic Isotope Effect
LAG	Least-Action Ground State
LCG	Large-Curvature Adiabatic Ground State
LCT	Large-Curvature Tunnelling
LOT	Level of Theory
μOMT	Microcanonical Optimised Multi-Dimensional Tunnelling
MCPVA	Marcus-Coltrin-Path Vibrationlly Adiabatic
MCTDH	Multiconfiguration Time Dependent Hartree
MEP	Minimum Energy Path
MI	Mapped Interpolation
MT	Multi-Dimensional Tunnelling
PES	Potential Energy Surface

QRS	Quantum Reactive Scattering
RD	Reduced Dimensionality
RPMD	Ring Polymer Molecular Dynamics
SAG	Semi-Classical Adiabatic Ground State
SCSAG	Small-Curvature Semi-Classical Adiabatic Ground State
SCT	Small-Curvature Tunnelling
SCTST	Semi-Classical Transition State Theory
TS	Transition State
TST	Transition State Theory
WKB	Wentzel-Kramers-Brillouin
ZCT	Zero-Curvature Tunnelling
ZPE	Zero Point Energy

Chapter 1

Introduction

In the field of chemical kinetics, transition state theory (TST) had been a popular method used to calculate the reaction rate constants in the gas and condensed phases.[1] It is still widely used nowadays due to its ease of implementation and its usefulness in providing a way to interpret kinetic data.[2,3] The theory was first formulated by Eyring[4] in 1935. In Eyring's early papers,[4,5] the focus was on calculating the reaction rate constants based on information at the so-called activation complex, which was the saddle point of the potential energy surface (PES). It was assumed that the activated complex was in a "quasi-equilibrium" with the reactants and that the activated complex was a normal molecule, with the exception that it was unbounded in one degree of freedom, i.e. the reaction coordinate.[4,5] This unbounded degree of freedom was treated as a translational degree of freedom. The final expression of the rate equation by Eyring[4] put together thermodynamics, kinetics and statistical mechanics.[6] Evans and Polanyi[7] also arrived at equivalent expressions of the rate equation concurrently but separately in 1935. This rate expression was interpreted as calculating the flux of the system through a dividing surface placed at the transition state (the activated complex) in phase space.[8–10]

The theory was first applied to, for example, $H + H_2$,[11] $Cl + H_2$,[12] $H_2 + I_2$,[12] and $H_2 + ICl$,[13] amongst other tested reactions.[7,8,14] However, the resulting reaction rate con-

stants did not show good agreement with experimental data.[12,15–17] Wigner[8] attributed such discrepancies to a few factors. Firstly, it was difficult to obtain accurate PESs used in the calculations.[8,18] At that time, the construction of a PES relied on experimental data which could be erroneous.[8,19] This rendered the PES inaccurate. Secondly, one of the main assumptions of the TST was that the motion of the atoms from the reactants to products could be explained by classical mechanics,[3,8,18] i.e. once the reacting system reached the transition state, if it crossed over to the product side, there was certainty that it would never cross back to the reactant side. A consequence of this assumption was that the calculated reaction rate constants, given that an accurate PES was available, gave the exact classical reaction rate constant if and only if all trajectories crossed the transition state only once from the reactants to the products.[3,8,20] However, for reactions at high temperatures or with complicated PESs that had low energy barriers, it was likely that the trajectories crossed the transition state more than once.[9,21] This led to an overestimation of the TST reaction rate constants as compared to the exact classical reaction rate constants. Thirdly, the lack of quantum effects in Eyring's formulation contributed to the inaccuracies of the TST method.[4,8] Even before the formulation of Eyring's well-known rate equation, Bell[22] showed in 1933 that the behaviour of the reacting system might deviate from classical behaviour especially at low temperatures, and when the atom moving along the potential energy barrier was lighter than a helium atom. As a result, even if the classical reaction rate constants calculated from the PES were in good agreement to exact classical reaction rate constants obtained from classical dynamics, the presence of quantum effects could mean that the reaction rate constants calculated classically was still a poor approximation to the true reaction rate constants.[22–26]

Since then, many improvements had been made over the decades to address the factors described above using advanced computational and theoretical tools.[3,18,23,27–29] Firstly, computational power has improved over the years.[18] Accurate PESs and energy barriers that are independent of experimental data can now be obtained with *ab initio* calcula-

tions.[30,31] Secondly, a variational principle to search for the dividing surface which gave a minimum reaction rate constant was proposed by Horiuti[9] to produce the best estimate of the exact classical reaction rate constant. This variational principle to search for the lowest upper bound was first tested by Horiuti,[9] and became more popular after the works by Keck.[32] Thirdly, the partition functions formulated using classical theory in Eyring's rate equation were replaced with quantised partition functions.[33–37] However, even with quantisation of the partition functions, some of the quantum effects such as quantum tunnelling were still not included in these calculations.[38,39] Several methods[40–54] had been developed to account for such effects, and one approach which has had many applications was the multi-dimensional tunnelling (MT) methods.[55]

In these methods, quantum tunnelling effects were represented by means of a multiplicative transmission coefficient.[56] There were three types of MT, namely zero-, small-, and large-curvature tunnelling (ZCT, SCT and LCT respectively).[38,39] These three methods differed in the extent they considered the curvature of the reaction path. However, they all required an understanding of how a reacting system moved along the PES from reactants to products.[39] According to Dunitz,[57] the trajectories of the reacting system appeared to be concentrated along the valleys on the PES connecting the reactants and products. This was termed as the so-called minimum energy path (MEP). The MEP could be calculated by the steepest descent method.[33,58,59] In order to calculate tunnelling corrections, the potential energy curve along the MEP was required.[38,39] This was calculated by assuming vibrational adiabaticity.[60] The contributions of the orthogonal vibrational modes were included as zero point energies (ZPE) to the potential energy along the MEP to produce an adiabatic ground state potential energy curve.[58] By including the ZPEs of the vibrational modes, the calculation was essentially a multi-dimensional one. However, since only the movement along the reaction coordinate was treated explicitly, subsequent tunnelling calculations were reduced to a one-dimensional problem with respect to the reaction coordinate, and this led to a considerable reduction of computation time.[61]

In the simplest MT method, the ZCT,[3,62] the MEP was taken directly as the tunnelling path in the calculation. However, ZCT had been proven to underestimate tunnelling corrections due to the lack of consideration of the curvature of the reaction path.[63]

Since the reaction path was usually curved, this gave rise to coupling between the motion along the reaction coordinate and the orthogonal vibrational modes of the reacting system along the reaction path.[64,65] Such coupling led to a negative centrifugal effect which caused the reaction path to be shifted to the concave side of the MEP on the PES. This resulted in a shorter reaction path length and hence increased the tunnelling contributions.[64,65] This was similar to the way Marcus and Coltrin calculated the reaction path for the reaction $H + H_2$ using the the Marcus-Coltrin-path vibrationally adiabatic (MCPVA) method.[66,67] When applied to the reaction $H + H_2$, it was found that MCPVA produced better agreement to quantum reactive scattering (QRS) results than ZCT.[67] This substantiated the claim that inclusion of the curvature of the reaction path was important for more accurate reaction rate constants.[68] In order to include such reaction path curvature into the tunnelling calculations, the small-curvature tunnelling (SCT) method was formulated.[68,69]

In the initial stage of formulation of the SCT tunnelling method, its development was specific to collinear atom-diatom reactions.[61,68,69] This small-curvature semi-classical adiabatic ground state (SCSAG) method considered the effects of small reaction path curvature by restricting the curvature to be small such that the unconstrained Schrödinger equation remained in the single-valued region.[61,68,69] This reaction path curvature was treated by defining an effective reduced mass, $\mu_{\text{eff}}(s)$, in the calculations. It accounted for the dependence of the length of the reaction path on the coupling between the reaction coordinate and its orthogonal vibrational modes.[61,63,68–70] When solving for the transmission probability, the Wentzel-Kramers-Brillouin (WKB) method[71] was used to solve for the Schrödinger equation.

However, in general polyatomic reactions, there can be more than one orthogonal vibrational modes that are coupled strongly to the movement along the reaction coordinate.[72]

Lu *et al.* proposed an improvement to SCSAG, termed as centrifugal-dominant SCSAG (CD-SCSAG).[72] In CD-SCSAG, the vibrational axes of the reacting system are rotated in a way such that the curvature vector lies along one of the axes. In this newly defined coordinate system due to the rotation of the vibrational axes, there was no coupling between both the movement along the reaction coordinate, the movement along this vibrational axes and all other motions. The effective mass in CD-SCSAG was then calculated in a similar way as in SCSAG.[68,69,72] Lu *et al.*[72] suggested that CD-SCSAG was a better approximation for more general applications to any polyatomic reactions. However, it should be noted that comparison between SCSAG and CD-SCSAG showed that for collinear atom-diatom reactions, both methods gave identical results.[72]

Over the years, the SCT methods have been tested widely in both collinear and non-collinear atom-diatom reactions.[56,61,62,73–76] Results from these tests showed better agreement to experimental and QRS results than ZCT ones. This suggested that consideration of the curvature of reaction paths was important in tunnelling corrections.[38,39]

It was suggested by Skodje *et al.*[26,69,77] that inclusions of small curvature would fail for reactions that had large reaction path curvatures, especially systems that had the "heavy-light-heavy" configuration. With such a mass configuration, the PES for the reaction has a small skew angle in the mass-weighted coordinates.[26] In such a case, it was suggested that tunnelling would occur on paths that were the most direct.[77] This is taken to be the straight lines that linked the reactant and product valleys on the PES. For any energy, E (smaller than the adiabatic barrier height), there was a straight tunnelling path that linked the points on the reactant side of the MEP which have the energy E to the product side of the MEP with the same energy.[77,78]

The initial model for the large-curvature tunnelling (LCT) method, termed as the large-curvature adiabatic ground state (LCG) method,[77] was formulated for collinear atom-diatom reacting systems. It assumed that such tunnelling occurs when the reactants and products were in the ground state. Since the tunnelling paths were at a particular energy E, it was

proposed that the reacting system had sufficient energy to initiate tunnelling for any straight tunnelling paths that had energies less than E.[77] The tunnelling probability for the LCG method was then an accumulation of the tunnelling probabilities for all the straight line paths with energy up to E. It was shown that the LCG tunnelling paths exhibited the so-called "corner-cutting" phenomena, where the tunnelling paths were deep within the reaction swath and far from the MEP.[77] The transmission coefficient in this LCG model was calculated based on the usual primitive ground state transmission probability.[77,79]

Alternatively, the transmission coefficient was proposed to be calculated using a hyperspherical treatment,[79,80] and such a method was termed LCG2. When LCG and LCG2 were tested against accurate QRS results for collinear heavy-light-heavy reactions, both methods had good agreement over a large range of temperatures.[79] They also produced similar results when compared to each other. However, Bondi et al.[79] suggested that it was more reasonable to use the LCG than the LCG2 model due to convenience of calculations and the accuracy in predicting the oscillations in the reaction probabilities.

With the success of the LCG method, an extension of the LCG method was proposed. This new least-action ground state (LAG) method[81] was constructed so that reaction rate constant calculations for reactions with any number of atoms and with any reaction path curvature could be possible. In the LAG method, the key feature was that a sequence of tunnelling paths linking the points in the reactant and product valleys with the same energy E was constructed based on a linear interpolation of all possible tunnelling paths between the ZCT tunnelling path (the MEP) and the straight-line tunnelling path.[81] The barrier penetration integral was calculated for all the paths. The optimum tunnelling path at E was then determined to be the path with the lowest barrier penetration integral. The calculation of the transmission probability was the same as previous papers.[68,69,76,77,82] When the LAG method was tested again the LCG and SCT methods, it was found that it produced better agreement to accurate QRS results than SCT and was the best method to use for reactions with intermediate reaction path curvatures.[81]

Since all possible tunnelling paths were taken into consideration at any particular energy, the LAG method was computationally more expensive than the SCT or LCG methods.[81] As a result, the so-called LCG3 method[83] was adapted from the LAG method. In LCG3, the tunnelling path used was the shortest tunnelling path linking the reactant and product valleys at any energy in the LAG method. The advantage of LCG3 over LCG was that LCG3 was applicable to any general polyatomic reacting system.[83] It was much more computationally efficient than LAG as it required computation of only one of the many tunnelling paths from LAG. The LCG3 method was tested on a range of symmetric and asymmetric heavy-light-heavy reacting systems and was found to produce good agreement with the LAG and QRS reaction rate constants.[83,84]

However, by employing the LCG3 method instead of the LAG method to account for tunnelling contributions, the variability of the reaction path curvature was lost. Therefore, a combination of the SCT and LCG3 tunnelling methods were used.[85] In this combination method termed the microcanonical optimised multi-dimensional tunnelling (μOMT) approximation,[85] the tunnelling probabilities were chosen from the larger of the tunnelling probabilities calculated from the LCG3 and the SCT methods at every energy. This meant that the barrier penetration action was the one that had the least action as in the LAG method.[81,85] The SCT, LCG3 and μOMT methods were tested on various reactions.[86] It was found that for a large number of reactions, the μOMT method was generally reliable and produced good agreement with accurate QRS results.[86]

In cases where there were discrepancies with QRS calculations, these differences were attributed to the deficiencies of the tunnelling methods.[86] Therefore, the LCG3 method was improved to the most recent LCG4 method.[87] In this method, anharmonic corrections to the adiabatic ground state potential energy were introduced, and the fragments of the tunnelling paths were calculated differently.[39,87] These were improved when comparing to LCG3 to ensure that there was no discontinuity in the potential energy barrier along the tunnelling paths.[39,87] However, LCG4 did not significantly increase the computation costs

when comparing to LCG3.[87] The LCG4 method was first tested on the $CH_3 + H_2$[85,88] and the unimolecular rearrangement of formamidine monohydrate[85,89] reactions and compared against the LCG3 method.[87] It was found that the transmission coefficients for the LCG4 method was more physically meaningful than the LCG3 method when studying the kinetic isotope effects, and the improvement in the anharmonic corrections in the LCG4 method led to improvements in the Boltzmann-weighted transmission probability curve.[87] Due to the similarities between the LCG3 and LCG4 methods, in the more recent version of μOMT method,[87] the transmission probabilities calculated for the LCG3 method was replaced by the LCG4 method due to its improvements to the LCG3 method. Since then, MT had been generally used to describe a group of tunnelling methods consisting of ZCT, SCT (CD-SCSAG), LCT (LCG4) and the μOMT methods.[39] The different MT methods had also been applied to a wide range of reactions and in conjunction with other methods.[90–95]

In the tests of the accuracy of MT methods, results from MT were compared against experimental data and accurate QRS calculations on the same PESs.[96] The conventional way to calculate reaction rate constants quantum mechanically required the formulation of PESs and solving the time-dependent or time-independent Schrödinger equation in QRS calculations.[40] However, it is computationally expensive to construct full-dimensional PESs even for reactions with four atoms.[97] As a result, several approximate methods had been developed to calculate reaction rate constants for general polyatomic reacting systems, of which one of them was the MT methods. Other methods include centroid molecular dynimcs (CMD),[41,42] ring polymer molecular dynamics (RPMD),[43–46] semi-classical transition state theory (SCTST),[47–50] and multiconfiguration time dependent hartree (MCTDH).[51–54]

A full-dimensional QRS calculation, though providing the most accurate dynamical results including the rate constants for a chemical reaction,[86] is often computationally too expensive to perform.[97] To our knowledge, the largest system treated full-dimensionally involved only six atoms.[98–100] Since some of the internal degrees of freedom in the reacting systems had almost negligible impact on the reaction, the reduced dimensionality (RD)

method[96,97,101,102] was developed. In such a method, only a subset of the internal degrees of freedom, termed as the active modes, were treated explicitly while the contributions of remaining internal degrees of freedom, termed as the spectator modes, were only added to the PES as ZPEs.[102–105] This treatment to the spectator modes is very similar to the construction of the adiabatic ground state potential energy barrier used in ZCT calculations, except that the constructed PES in the RD method is still multi-dimensional. As a result, the RD methods were able to have accurate calculations for the active modes but yet be more computationally efficient than full-dimensional calculations.[106] In particular, the 2-dimensional (2D) QRS model[107,108] was used for collinear or near-collinear reactions that involved the breaking and formation of chemical bonds.[106,107,109–113] The *R*-matrix propagation method[114] was used on the 2D PESs to obtain the reaction probabilities which in turn could be used to calculate the reaction rate constants.[40] The results were in good agreement to experimental data and other theoretical works for many reactions.[106,107,109,111–113,115]

In this study, the accuracy of MT is tested against QRS on the 2D PESs of hydrogen abstraction and exchange reactions of polyatomic hydrocarbon molecules.[109,110,112,113] By performing QRS calculations on the constructed PESs, the reaction rate constants obtained are exact results for solutions to the Schrödinger equation for the PESs.[86] Therefore, comparisons between the results from the MT and QRS methods can be made.[86] These directly test the accuracy of the MT methods since any errors arising due to the inaccuracies of the PESs would not contribute to the differences in the results.[33,86] This provides useful insights into the approximations employed in the MT methods.[33]

The remainder of this thesis is organised as follows. Chapter 2 gives the background of the TST and MT methods. The partition functions contributing to the TST reaction rate constant are first briefly introduced, and a description of the calculation of the MEP and its corresponding adiabatic ground state potential energy curve is then given. The various MT methods (ZCT, SCT and LCT) are then presented in its full-dimensional form, before a description of the adaptation of these methods to the RD framework is given.

Chapter 3 gives the description of RDPOLY, the program written to apply the TST/MT methods to the previously constructed RD PESs.[109,110,112,113] Comparison between RDPOLY and POLYRATE,[116] a popular computer program currently available that is used to calculate reaction rate constants, is also given in this chapter to outline the accuracy of RDPOLY. A brief description of the RD PESs used in this thesis is also given in this chapter.

Chapter 4 presents the results and discussion for the hydrogen abstraction reactions studied in this thesis. This includes the reactions,

$$CH_4 + H \longrightarrow CH_3 + H_2 \quad \text{(R1)}$$

$$C_2H_6 + H \longrightarrow C_2H_5 + H_2 \quad \text{(R2)}$$

$$\text{cyc-}C_3H_6 + H \longrightarrow \text{cyc-}C_3H_5 + H_2 \quad \text{(R3)}$$

which involves the abstraction of a hydrogen atom from linear or cyclic alkanes by a second hydrogen atom. The RD PES, TS on the RD PES, MEP and potential energy curves along the MEP are given for each reaction. The reaction rate constants obtained from TST/ZCT and TST/SCT calculations with and without mapped interpolation (MI) are compared against QRS calculations on the same surfaces[109,112,113] and with experimental data to study the effect of including reaction path curvature of the RD PESs in tunnelling calculations and the importance of maximising the use of the available RD PESs.

Chapter 5 presents the results and discussion for the hydrogen exchange reaction and its symmetric deuterated variants,

$$CH_4 + CH_3 \longrightarrow CH_3 + CH_4 \quad \text{(R4)}$$

$$CH_3D + CH_3 \longrightarrow CH_3 + CH_3D \quad \text{(R5)}$$

$$CD_4 + CD_3 \longrightarrow CD_3 + CD_4 \quad \text{(R6)}$$

which involves the exchange of a hydrogen or deuterium atom between two unsubstituted methyl groups or its symmetric deuterated variants. The RD PES, TS on the RD PES, MEP and potential energy curves are given for each reaction. Due to the larger and heavier methyl groups involved in the hydrogen exchange reaction of the reaction $CH_4 + CH_3$, the reaction path curvature for the reaction is larger than the other reactions studied in this thesis. Hence, the effect of implementing the LCT method on the RD PES of the $CH_4 + CH_3$, $CH_3D + CH_3$ and $CD_4 + CD_3$ reactions is studied in this chapter. TST/SCT and TST/LCT reaction rate constants are compared against QRS ones calculated on the same surfaces and experimental data to study the significance of corner-cutting effects in these reactions. Results between the reactions are also compared against each other in the chapter to study the primary and secondary kinetic isotope effects (KIE) of the $CH_4 + CH_3$ and $CH_3D + CH_3$ reactions respectively.

Chapter 2

Theory

2.1 Classical Transition State Theory

The reaction rate constant for the classical Transition State Theory (TST) is a well-established method used in the calculation of many reaction rates. It is given by[4,7,33]

$$k^{\mathrm{TST}}(T) = \frac{1}{\beta h}\frac{Q^{\ddagger}}{Q_{\mathrm{R}}}\exp\left[-\beta V_{\mathrm{a}}^{\mathrm{GTS}}\right] \tag{2.1}$$

where T is the temperature, h is the Planck constant, $V_{\mathrm{a}}^{\mathrm{GTS}}$ is the adiabatic ground state potential energy of the transition state (TS) relative to the adiabatic ground state potential energy of the reactants, Q_{R} and $Q^{\ddagger}$ are the partition functions of the reactants and TS respectively and $\beta = (k_{\mathrm{B}}T)^{-1}$, where k_{B} is the Boltzmann constant.

Each type of partition function Q measures the number of thermally accessible states of that particular type of motion of the molecule at a temperature T.[117] For a system with degenerate energy levels the function is given by[117,118]

$$Q = \sum_{i=0}^{j} g_i \exp\left[-\beta E_i\right], \tag{2.2}$$

where j is the total number of energy levels, and g_i is the degeneracy of the energy level, E_i.

The total partition function for a polyatomic molecule consists of contributions from translational, vibrational, rotational, and electronic motions. In this particular study, these four types of energies are assumed to be uncoupled. The partition function of each individual type is briefly discussed here. The translational partition function for a polyatomic molecule confined in a 3-dimensional space, with a as the length of each dimension, is given by[34,36]

$$Q_{\text{trans}} = a^3 \left[\frac{2\pi m}{\beta h^2}\right]^{3/2}, \tag{2.3}$$

where m is the mass of the molecule. Under the rigid rotor-harmonic oscillator approximation of a polyatomic molecule, the vibrational partition function is given by[34,35,37]

$$Q_{\text{vib}} = \prod_{i=1}^{l} \frac{1}{1-\exp\left[-\beta h \nu_i\right]}, \tag{2.4}$$

where l is the number of vibrational modes present in the polyatomic molecule, and ν_i is the vibrational frequency of the i-th vibrational mode. The rotational partition function of the polyatomic molecule under such approximation is[34,37]

$$Q_{\text{rot}} = \frac{1}{\sigma}\left[\frac{\pi T^3}{\theta_x \theta_y \theta_z}\right]^{1/2}, \tag{2.5}$$

where σ is the symmetry number of the polyatomic molecule, and θ_x, θ_y, and θ_z are the characteristic rotational temperatures corresponding to the rotation of the molecule around the x-, y- and z- axes respectively. θ is given by[34,37]

$$\theta_k = \frac{h^2}{8\pi^2 I_k k_{\text{B}}} \tag{2.6}$$

where I_k is the moment of inertia of the molecule in the k-axis (where $k = x$, y or z). The

electronic partition function of a molecule can be expressed by[34,37]

$$Q_{\text{elec}} = \sum_{i=0}^{p} g_i \exp\left[-\beta E_{\text{elec},i}\right] \tag{2.7}$$

where p is the number of electronic levels in the molecule, and g_i is the degeneracy of the electronic level i. The separation between electronic levels is usually large, suggesting that only the ground state of the electronic partition function is accessible.[34,37] For all the reactions considered in this study, $E_{\text{elec},0} = 0$. Eq 2.7 then becomes

$$Q_{\text{elec}} = g_0. \tag{2.8}$$

Since the four types of energies contributing to the total partition function are assumed to be uncoupled to one another, the total partition functions of the reactants and transition state can be expressed as a product of the individual partition functions,[117]

$$Q = Q_{\text{trans}} Q_{\text{vib}} Q_{\text{rot}} Q_{\text{elec}}. \tag{2.9}$$

2.2 Multi-Dimensional Tunnelling

Although the reaction rate constants can be easily computed using the TST method, a major drawback of this method is the lack of accounting of any quantum effects, such as quantum tunnelling.[8] Such effects have large contributions to rate constants of chemical reactions especially at low temperatures, and when hydrogen atoms are directly involved, e.g. in hydrogen abstraction and hydrogen exchange reactions.[22] In order to improve the TST method, various multi-dimensional tunnelling (MT) methods have been developed to incorporate such quantum effects.[33,61,68,69,77,79,83,87]

2.2.1 Outline of Multi-Dimensional Tunnelling

In the TST/MT methods, a temperature dependent factor, which is the so-called semi-classical adiabatic ground state transmission coefficient, $\kappa^{\mathrm{SAG}}(T)$, is multiplied by the TST rate constant, $k^{\mathrm{TST}}(T)$, to give[38,39]

$$k(T) = k^{\mathrm{TST}}(T)\kappa^{\mathrm{SAG}}(T), \tag{2.10}$$

where $\kappa^{\mathrm{SAG}}(T)$ is given by,[38,39]

$$\kappa^{\mathrm{SAG}}(T) = \frac{\int_0^\infty dE\ \exp[-\beta E]P^{\mathrm{SAG}}(E)}{\beta^{-1}\exp[-\beta V_{\mathrm{a}}^{\mathrm{Gmax}}]}. \tag{2.11}$$

In Eq 2.11, $P^{\mathrm{SAG}}(E)$ is the semi-classical adiabatic ground state transmission probability at energy E that the system has access to, and $V_{\mathrm{a}}^{\mathrm{Gmax}}$ is the maximum energy of the adiabatic ground state potential. There are three types of MT methods, namely the zero-,[33] small-[61,68,69] and large-curvature tunnelling[77,79,83,87] calculations (abbreviated as ZCT, SCT and LCT respectively). When calculating $\kappa^{\mathrm{SAG}}(T)$, information of the minimum energy path (MEP) is required.[58] The construction of the MEP, including geometrically finding the MEP points on a PES and calculating the adiabatic potential energy at each point, will be discussed in the next section.

2.2.2 Minimum Energy Path

When a reacting system moves along a potential energy surface (PES) from reactants to products, it can choose to move along a wide variety of trajectories depending on the amount of energy the system possesses.[57] These trajectories are localised in the valleys on the PES that connected the reactants and products. On a PES expressed in mass-weighted coordinates, the MEP is calculated by tracing out the path from the transition state to the reactants and products using the steepest descent method.[26] This path provides a descrip-

tion of the mechanism of the reaction from reactants to products, by giving the geometries and energies of non-stationary points as the reaction progresses along the MEP. Additional calculations can also be performed along the MEP to obtain the vibrational frequencies, and other relevant dynamical properties required to study the reaction rate constants of the reaction.

2.2.2.1 Steepest Descent Path

In a mass-weighted Cartesian coordinate system, the coordinate can be expressed as[119]

$$a_{i,x} = \sqrt{\frac{m_i}{\mu}} A_{i,x} \tag{2.12}$$

where a is the mass-weighted x-coordinate for atom i, m_i is the mass of atom i, μ is the reduced mass of the system, and A is the non-mass-weighted x-coordinate for atom i. For bimolecular reactions, μ is given by[39]

$$\mu = \frac{m_{\mathrm{A}} m_{\mathrm{B}}}{m_{\mathrm{A}} + m_{\mathrm{B}}} \tag{2.13}$$

where m_{A} and m_{B} are the masses of the reactants A and B of the bimolecular reacting system. Without loss of generality, this can be applied to the y- and z-coordinates as well. In the mass-weighted coordinate system, the kinetic term in the Hamiltonian is reduced to[119]

$$\begin{aligned} T &= \frac{1}{2} \sum_{i=1}^{N} m_i \frac{d}{dt} (A_{i,x}^2 + A_{i,y}^2 + A_{i,z}^2) \\ &= \frac{\mu}{2} \sum_{i=1}^{N} m_i \frac{d}{dt} \left(\left[\frac{a_{i,x}}{\sqrt{m_i}} \right]^2 + \left[\frac{a_{i,y}}{\sqrt{m_i}} \right]^2 + \left[\frac{a_{i,z}}{\sqrt{m_i}} \right]^2 \right) \\ &= \frac{\mu}{2} \sum_{i=1}^{N} \frac{d}{dt} (a_{i,x}^2 + a_{i,y}^2 + a_{i,z}^2) \end{aligned} \tag{2.14}$$

where N is the number of atoms in the system. The kinetic term in the Hamiltonian now becomes independent of the masses of the individual atoms. As a result, PESs are expressed

in mass-weighted coordinates such that movements on the PES by polyatomic molecules are reduced to movements by a point mass μ.

Since the MEP is calculated by the steepest descent method from the TS, the reacting system moving along the MEP from the TS follows the direction of the vector that points towards the direction of steepest descent, i.e. the gradient of the PES. The equation of motion for such movement is given by,[119]

$$\mu \frac{d^2}{dt^2} a_{i,x} = -\frac{\partial V}{\partial a_{i,x}} \tag{2.15}$$

where V is the potential energy function of the PES. Integrating Eq 2.15 with respect to t, we obtain

$$\mu \frac{d}{dt} a_{i,x} + C = -\frac{\partial V}{\partial a_{i,x}} t \tag{2.16}$$

where C is the integration constant. When $t = 0$, the velocity of the system $da_{i,x}/dt = 0$, therefore the integration constant $C = 0$. Eq 2.16 then simplifies to give[39]

$$\mu \frac{d}{dt} a_{i,x} = -\frac{\partial V}{\partial a_{i,x}} t. \tag{2.17}$$

In vector form, Eq 2.17 gives the expression[39]

$$\mu \frac{d\mathbf{a}}{dt} = -\frac{\partial V}{\partial \mathbf{a}} t. \tag{2.18}$$

For an infinitesimal step taken in the direction of the steepest descent, the distance travelled on the PES is[39]

$$ds = \left[\sum_{i=1}^{N} da_{i,x}^2 + da_{i,y}^2 + da_{i,z}^2 \right]^{1/2} = \left| \frac{\partial V}{\partial \mathbf{a}} \right| \frac{t \, dt}{\mu}. \tag{2.19}$$

Substituting Eq 2.19 into Eq 2.18 gives

$$\frac{d\mathbf{a}}{ds} = -\widehat{\mathbf{v}} \tag{2.20}$$

where $\widehat{\mathbf{v}}$ is the unit vector of $\partial V/\partial \mathbf{a}$. By means of following the path of steepest descent from the transition state, the MEP can be traced from the reactants to the products.[38,39,119]

2.2.2.2 Calculation of the Adiabatic Ground State Potential Energy Curve

The calculation of MT to account for quantum effects is carried out along the MEP where only the movement along the reaction coordinate is treated explicitly.[39] All other vibrational modes are included in the calculations as zero point energies (ZPE). The adiabatic ground state potential energy is then calculated as the sum of the potential energy from the PES and ZPEs and used in MT calculations.

The potential energy along the MEP can be easily obtained from either direct *ab initio* calculations or an analytical PES function.[39] Calculation of the ZPEs of the other bounded vibrational modes requires the removal of any contribution from the movement along the unbounded reaction coordinate to the movements along these vibrational modes.[120] This is carried out using projection methods in rectilinear[121] or curvilinear coordinates.[120] Details of the projection methods can be found in the literature[120,121] and only a brief outline is provided for each method here.

For the projection method in rectilinear coordinates, the vector representing the reaction coordinate is the mass-weighted gradient of the PES by the steepest descent method. At any point along the MEP, s, we denote the mass-weighted gradient of the PES corresponding to the motion along the reaction coordinate at s as $\overline{\mathbf{v}}$. Then the rectilinear projection operator that spans this 1-dimensional subspace is[121]

$$\mathbf{P}_{s,R} = \frac{\overline{\mathbf{v}}\,\overline{\mathbf{v}}^{\mathrm{T}}}{|\overline{\mathbf{v}}|^2} \tag{2.21}$$

where $\overline{\mathbf{v}}^{\mathrm{T}}$ is the transpose of the vector $\overline{\mathbf{v}}$. Since we want to project out the motion along the reaction coordinate from the pre-projection Hessian, the $3N$x$3N$ matrix of force constants

where N is the number of atoms in the reacting system, the desired subspace is given by

$$\mathbf{P}_R = \mathbf{I} - \mathbf{P}_{s,R} \tag{2.22}$$

where $\mathbf{I}$ is the identity matrix. As a result, the post-projection mass-weighted Hessian in rectilinear coordinates is

$$\mathbf{H}_{R,\text{proj}} = (\mathbf{I} - \mathbf{P}_{s,R})\mathbf{H}_{R,\text{unproj}}(\mathbf{I} - \mathbf{P}_{s,R}) \tag{2.23}$$

where $\mathbf{H}_{R,\text{unproj}}$ is the pre-projection mass-weighted Hessian in rectilinear coordinates.[121]

In curvilinear projection, the non-mass-weighted gradient and Hessian at a point s along the MEP are first converted into mass-weighted curvilinear coordinates using the Wilson B matrix and C tensor,[120,122]

$$\begin{aligned} \mathbf{g} &= \mathbf{A}^T\mathbf{G}, \\ \mathbf{f} &= \mathbf{A}^T\mathbf{F}\mathbf{A} - \sum_i^N g_i \mathbf{A}^T\mathbf{C}^{[i]}\mathbf{A} \end{aligned} \tag{2.24}$$

where $\mathbf{g}$ and $\mathbf{f}$ are the mass-weighted gradient and Hessian in curvilinear coordinates respectively, $\mathbf{C}^{[i]}$ is the square sub-matrix in the C tensor that corresponds to the i-th internal coordinate, and $\mathbf{A}$ is the generalised inverse of the Wilson B matrix.[120] The curvilinear projection operator is then given by[120]

$$\mathbf{P}_{s,C} = \frac{\overline{\mathbf{g}}\,\overline{\mathbf{g}}^{\mathrm{T}}}{|\overline{\mathbf{g}}|^2}, \tag{2.25}$$

and the desired subspace,

$$\mathbf{P}_C = \mathbf{I} - \mathbf{P}_{s,C}. \tag{2.26}$$

The post-projection mass-weighted Hessian in curvilinear coordinates is then given by

$$\mathbf{H}_{C,\text{proj}} = (\mathbf{I} - \mathbf{P}_{s,C}\mathbf{h}^*)\mathbf{H}_{C,\text{unproj}}(\mathbf{I} - \mathbf{h}^*\mathbf{P}_{s,C}) \tag{2.27}$$

where $\mathbf{h}^*$ is the contravariant metric tensor of the space spanned by the curvilinear coordinates.[120] The post-projection mass-weighted Hessians, $\mathbf{H}_{R,\text{proj}}$ or $\mathbf{H}_{C,\text{proj}}$, can then be used to calculate the post-projection vibrational frequencies and the corresponding ZPEs for the spectator vibrational modes. The adiabatic ground state potential along the MEP is[39]

$$V_\text{a}^\text{G}(s) = V_\text{MEP}(s) + \text{ZPE}(s). \tag{2.28}$$

An example of the potential energy and adiabatic ground state potential energy curves along the MEP of a chemical reaction is illustrated in Fig 2.1.

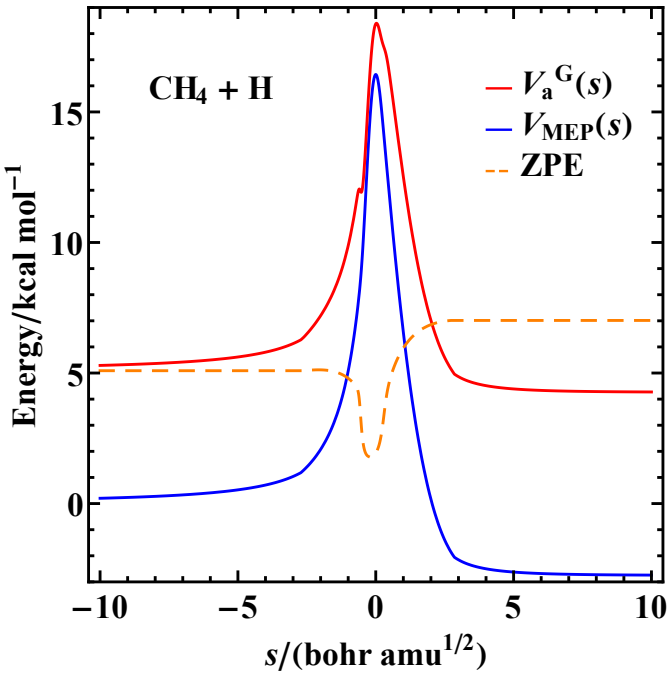


Figure 2.1: The potential energy curve, $V_\text{MEP}(s)$ (blue), and adiabatic ground state potential energy curve, $V_\text{a}^\text{G}(s)$ (red), for the $CH_4 + H \longrightarrow CH_3 + H_2$ reaction on a 2-dimensional analytical PES.[112] The difference between $V_\text{MEP}(s)$ and $V_\text{a}^\text{G}(s)$ at every point along the reaction coordinate, s, is the summation of all the ZPEs (orange) of the vibrational modes that are orthogonal to the motion along the reaction coordinate at s calculated using projection methods.[120,121]

We note that such projection methods are required on all points on the MEP except the stationary points. The adiabatic ground state potential energy in Eq 2.28 is subsequently used in the evaluation of the transmission coefficients by MT methods as described next.[39,121]

2.2.3 Zero- and Small-curvature Tunnelling

The simplest MT methods (ZCT and SCT) focus on calculating the tunnelling corrections along the reaction coordinate. For such evaluation, Skodje *et al.*[68] suggested that the equation for the wavefunction of the reaction coordinate when the bounded vibrational modes are treated as being vibrationally adiabatic is

$$\left[\frac{\langle A\rangle(s)}{2\mu}p_s^2 - V_{\mathrm{a}}^{\mathrm{G}}(s) + E\right]\Psi(s) = 0, \tag{2.29}$$

where $\langle A\rangle(s)$ is a measure of change in the kinetic term of the Hamiltonian due to the coupling between the movement along the reaction coordinate, s (given previously in Eq 2.19), and the orthogonal vibrational modes, and p_s is the momentum of the wavefunction at s.[63,68]

As the name suggests, ZCT assumes zero reaction path curvature, i.e. there is no coupling between the motion along the reaction coordinate and the other vibrational modes.[33] In this case, the tunnelling path is the MEP, and $\langle A\rangle(s) = 1$ for all s. By the Wentzel-Kramers-Brillouin (WKB) theory,[71] the barrier penetration integral for such wavefunction is evaluated by[63]

$$\theta(E) = \int \mathrm{Im}p_s(s,E)\, ds. \tag{2.30}$$

Substituting the expression of p_s from Eq 2.29 into Eq 2.30, we get the expression of the barrier penetration integral for the ZCT method,

$$\theta_{\mathrm{ZCT}}(E) = \int_{s_{\mathrm{R}}}^{s_{\mathrm{P}}} \sqrt{2\mu(V_{\mathrm{a}}^{\mathrm{G}}(s) - E)}\, ds. \tag{2.31}$$

In Eq 2.31, s_R and s_P are the outermost points of the adiabatic ground state potential energy curve ($V_a^G(s)$) on the reactant and product valleys respectively, and $V_a^G(s_R) = V_a^G(s_P) = E$.

With the barrier penetration integrals evaluated at all energies, the semi-classical adiabatic ground state transmission probability is then given by

$$P^{SAG}(E) = \begin{cases} 0 & \text{if } E < E_0 \\ \dfrac{1}{1+\exp[2\theta(E)]} & \text{if } E_0 \leq E \leq V_a^{Gmax} \\ 1 - P^{SAG}(2V_a^{Gmax} - E) & \text{if } V_a^{Gmax} \leq E \leq 2V_a^{Gmax} - E_0 \\ 1 & \text{if } E > 2V_a^{Gmax} - E_0 \end{cases} \tag{2.32}$$

where E_0 is the maximum of the reactant and product adiabatic ground state potential energies, and $\theta(E)$ is the barrier penetration integral evaluated at energy E. The energy levels in Eq 2.32 are illustrated in Fig 2.2.

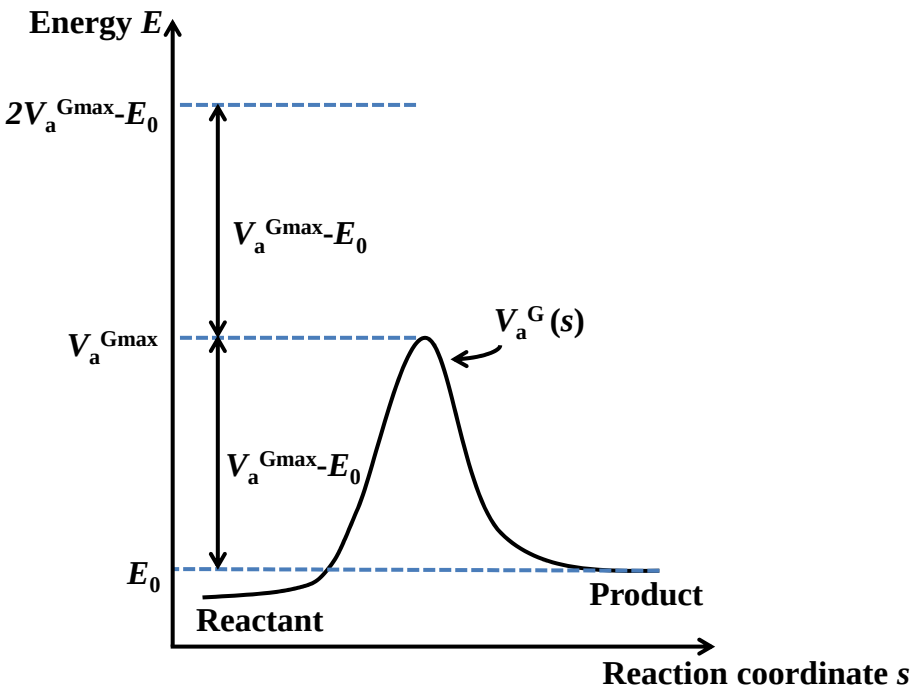


Figure 2.2: Energy levels used as the boundaries in the calculation of $P^{SAG}(E)$. The black curve is the adiabatic ground state potential energy curve along the MEP, $V_a^G(s)$, as the reaction proceeds from the reactants to products along the reaction coordinate s.

The transmission coefficient for the ZCT method is then obtained by Eq 2.11.

SCT takes into account the curvature of the reaction path due to coupling between the motion along the reaction coordinate and its orthogonal vibrational modes.[61,68,69] With such coupling, the reacting system exhibits the so-called corner-cutting phenomena where the tunnelling path is moved to the concave side of the MEP due to negative centrifugal effect and "cuts the corner" of the MEP. As a result, the SCT tunnelling path is shorter than the MEP.[39,68] This is similar to the tunnelling path proposed by Marcus and Coltrin[66] for the collinear $H + H_2 \longrightarrow H_2 + H$ reaction, which yielded much better agreement with quantum scattering results. Skodje *et al.*[68] further suggested that the shortening of the tunnelling path could be expressed in terms of an effective mass, $\mu_{\text{eff}}(s)$, so that the barrier penetration integral could still be evaluated along the MEP, which saved the computational effort of calculating a new tunnelling path. The relationship between $\mu_{\text{eff}}(s)$ and μ is given by[39]

$$\left[\frac{\mu_{\text{eff}}(s)}{\mu}\right]^{1/2} = \frac{d\gamma}{ds} \tag{2.33}$$

where ds is the instantaneous change in length of the MEP at s, and $d\gamma$ is the corresponding instantaneous change in length of the SCT tunnelling path due to the coupling. An illustration showing the relationship between $d\gamma$ and ds is given in Fig 2.3.

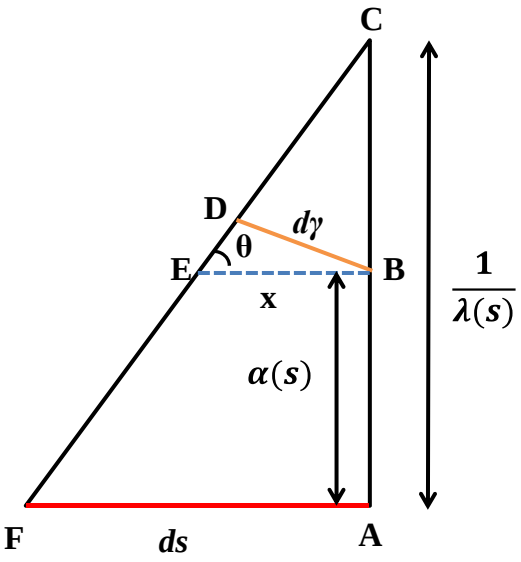


Figure 2.3: Illustration for the calculation of $d\gamma/ds$ (or $\sqrt{\mu_{\text{eff}}(s)/\mu}$). $1/\lambda(s)$ is the radius of the instantaneous circle at s (denoted by A) with curvature $\lambda(s)$ and effective vibrational turning point $\alpha(s)$, and θ and x are properties used in the computation of $d\gamma/ds$. AC is the direction of the displacement along the effective vibrational mode and is orthogonal to the direction of the movement along the reaction coordinate AF.

In Fig 2.3, the length x can be calculated by similar triangles,

$$\frac{x}{ds} = 1 - \alpha(s)\lambda(s), \tag{2.34}$$

where $\lambda(s)$ and $\alpha(s)$ are as described in Fig 2.3. The curvature of the reaction path, $\lambda(s)$, arises due to the coupling between the motion along the reaction coordinate and the orthogonal vibrational modes, and is given by[72]

$$\lambda(s) = \left[\sum_{k=1}^{F-1} B_{k,F}(s)^2\right]^{1/2}, \tag{2.35}$$

where $(F-1)$ is the number of vibrational modes in the reacting system orthogonal to the reaction coordinate, and $B_{k,F}(s)$ is the coupling between the motion along the reaction coordinate (the F-th mode) and the k-th vibrational mode at s. $B_{k,F}(s)$ is given by[39]

$$B_{k,F}(s) = -[\text{sign}(s)] \sum_{i=1}^{3N} \frac{d(-\overline{\mathbf{v}}_i(s))}{ds} L_{i,k}(s), \tag{2.36}$$

where $\overline{\mathbf{v}}(s)$ is the unit gradient vector at s, N is the number of atoms in the system, and $L_{i,k}(s)$ is the i-th component of the eigenvector corresponding to the k-th vibrational mode at s. For the calculation of $\alpha(s)$ in Fig 2.3 where there are more than one vibrational modes orthogonal to the reaction coordinate, it was proposed that the axes of the vibrational modes be rotated in a way such that the curvature vector lay along one of these axes.[72] The effective vibrational mode along this vector and the motion along the reaction coordinate would then be uncoupled from the other displacements in the other rotated axes, hence reducing a multi-dimensional problem to a 2-dimensional problem.[72] The harmonic frequency of this effective vibrational mode is given by[39]

$$\omega_{\text{eff}}(s) = \left[\sum_{k=1}^{F-1}\left[\frac{B_{k,F}(s)}{\lambda(s)}\omega_k(s)\right]^2\right]^{1/2} \tag{2.37}$$

where $\omega_k(s)$ is the vibrational frequency of the k-th mode at s. Within the harmonic approximation, the vibrational turning point for the k-th vibrational mode is given by[39]

$$t_k(s) = \left[\frac{\hbar}{\mu\omega_k(s)}\right]^{1/2}. \tag{2.38}$$

Similarly, for the effective vibrational mode, its vibrational turning point $\alpha(s)$ is given by[39,72]

$$\begin{aligned}\alpha(s) &= \left[\frac{\hbar}{\mu\omega_{\text{eff}}(s)}\right]^{1/2} \\ &= \left[\frac{\hbar}{\mu}\left[\sum_{k=1}^{F-1}\left[\left(\frac{B_{k,F}(s)}{\lambda(s)}\right)\left(\frac{\hbar}{t_k(s)^2\mu}\right)\right]^2\right]^{-1/2}\right]^{1/2} \\ &= \left[\sum_{k=1}^{F-1}\frac{B_{k,F}(s)^2 t_k(s)^{-4}}{\lambda(s)^2}\right]^{-1/4}.\end{aligned} \tag{2.39}$$

With the values of $\lambda(s)$ and $\alpha(s)$, x/ds can be obtained by Eq 2.34. In the calculation of $d\gamma$ in Eq 2.33, the angle θ in Fig 2.3 is assumed to tend towards 90^{o} in the limit that ds is

infinitesimal. Therefore, the desired $d\gamma$ can be found by,

$$x^2 + \mathrm{DE}^2 = d\gamma^2. \tag{2.40}$$

The length DE is the change in the vibrational turning point between s at A and s at F. This can be denoted by dt. By such approximation, we obtain

$$\begin{aligned} d\gamma &= \left([[1-\alpha(s)\lambda(s)]ds]^2 + dt^2 \right)^{1/2} \\ \frac{d\gamma}{ds} &= \left([1-\alpha(s)\lambda(s)]^2 + \left[\frac{dt}{ds}\right]^2 \right)^{1/2}. \end{aligned} \tag{2.41}$$

Combining Eqs 2.33 and 2.41, $\mu_{\mathrm{eff}}(s)$ can be calculated as

$$\mu_{\mathrm{eff}}(s) = \mu \left[(1-\alpha(s)\lambda(s))^2 + \left(\frac{dt}{ds}\right)^2 \right]. \tag{2.42}$$

In cases where the vibrational mode at s enters the multi-valued region where $\alpha(s)\lambda(s) > 1$, the expression for $(1-\alpha(s)\lambda(s))$ becomes physically not meaningful. In order to overcome this issue, an exponential form is used, and $\mu_{\mathrm{eff}}(s)$ can be expressed as[72]

$$\mu_{\mathrm{eff}}(s) = \mu \ \min \begin{cases} 1 \\ \exp\left[-2\alpha(s)\lambda(s) - (\alpha(s)\lambda(s))^2 + \left(\frac{dt}{ds}\right)^2 \right]. \end{cases} \tag{2.43}$$

The SCT barrier penetration integral is then given by a similar form as Eq 2.31,

$$\theta_{\mathrm{SCT}}(E) = \int_{s_{\mathrm{R}}}^{s_{\mathrm{P}}} \sqrt{2\mu_{\mathrm{eff}}(s)(V_{\mathrm{a}}^{\mathrm{G}}(s) - E)}\, ds. \tag{2.44}$$

The semi-classical adiabatic ground state transmission probability and the transmission coefficient are then calculated by Eqs 2.32 and 2.11 respectively.

2.2.4 Large Curvature Tunnelling

The ZCT and SCT methods described in the previous section are useful in calculating reaction rate constants for reactions that have small reaction path curvatures.[39] However, for reactions where the reaction path curvatures are large, especially in reactions with the so-called heavy-light-heavy mass combination, such methods are inappropriate.[39,77–79] In this case, the corner-cutting phenomena as presented in the previous section would be extreme. Garrett *et al.*[77] suggested that for reactions with small skew angles and large reaction path curvatures, tunnelling would occur on the shortest paths which were the most direct. These corresponded to the straight lines connecting the reactant and product valleys in the PES expressed in mass-weighted Cartesian coordinates.

For any straight-line tunnelling path, it was suggested that there should be no linear or angular momentum produced as the system moves along this path from the reactant valley to the product valley.[123] A convenient choice for the set of points to form the tunnelling path would be the points in the reactant and product valleys that have the same energy, E_i, following the resonant tunnelling model.[77] The barrier penetration integral can be expressed as[77]

$$\theta_{\mathrm{LCT}}(E_i) = \int_0^{\zeta_p} \sqrt{2\mu[V(\zeta) - E_i]}\, d\zeta \tag{2.45}$$

where ζ is the coordinate along the straight-line tunnelling path and ζ_p is the length of the tunnelling path. ζ_p is given by[39,87]

$$\zeta_p = \left[\sum_{i=1}^{N} [a_{r,i,x} - a_{p,i,x}]^2 + \sum_{i=1}^{N} [a_{r,i,y} - a_{p,i,y}]^2 + \sum_{i=1}^{N} [a_{r,i,z} - a_{p,i,z}]^2 \right]^{1/2} \tag{2.46}$$

where N is the number of atoms in the system, $a_{r,i,x}$ is the mass-weighted Cartesian x-coordinate for the point in the reactant valley (r) of the i-th atom, $a_{p,i,x}$ is the mass-weighted Cartesian x-coordinate for the point in the product valley (p) of the i-th atom, and similarly for $a_{r,i,y}$, $a_{p,i,y}$, $a_{r,i,z}$ and $a_{p,i,z}$.

When travelling along the LCT tunnelling path from the reactant valley to the product valley, the reacting system first travels through the region that is within the turning points of the vibrational modes orthogonal to the MEP in the reactant valley (adiabatic region). It may then travel through a region that is beyond the turning points of the orthogonal vibrational modes if it exists (non-adiabatic region), before entering the region that is within the turning points of the vibrational modes orthogonal to the MEP in the product valley (adiabatic region).[87] The boundaries of the adiabatic regions in the reactant and product valleys are termed as ζI and ζII respectively. The method to calculate these boundaries is described next.

When determining the boundaries ζI and ζII, the corresponding point on the MEP, s_ζ, for any reaction coordinate along the LCT tunnelling path, ζ, such that the vector formed between these two points is normal to the MEP is first found. This relationship is given by,[38,39]

$$[\mathbf{a}(\zeta) - \mathbf{a}(s_\zeta)] \cdot \frac{d\mathbf{a}(s_\zeta)}{ds} = 0 \tag{2.47}$$

where **a** refers to the mass-weighted Cartesian coordinates at its respective point along the LCT tunnelling path or MEP. We denote the reaction coordinate along the MEP that satisfies such condition s_ζ, i.e. s_ζ is the point along the MEP that is mapped onto the point ζ. The search of s_ζ for ζ when determining ζI starts from s_R (as defined in Eq 2.31) and ends at s_P and is subsequently defined as $s_{\mathrm{I},\zeta}$. Similarly, the search of $s_{\mathrm{II},\zeta}$ when determining ζII starts from s_P and ends at s_R.

The properties at ζ and its corresponding $s_{\mathrm{I},\zeta}$ or $s_{\mathrm{II},\zeta}$ were then tested with three conditions to determine if the boundaries have been reached.[38] Once any of the conditions is not met by the reacting system, the final value of ζ is set to be ζI and ζII in the reactant and product valleys respectively.[38,39] Without loss of generality, we define them for ζI. The first condition is that for any $\zeta \leq \zeta$I, $\mathbf{a}(\zeta)$ has to be within the vibrational turning points of all the vibrational modes at $s_{\mathrm{I},\zeta}$.[38] This condition can be tested by comparing the nor-

mal coordinates of the vector $(\mathbf{a}(\zeta) - \mathbf{a}(s_{\mathrm{I},\zeta}))$ for each mode with its respective vibrational turning points,[38]

$$Q_k(s_{\mathrm{I},\zeta}) \leq t_k(s_{\mathrm{I},\zeta}) \quad \text{for all } 1 \leq k \leq (F-1) \text{ vibrational modes,} \tag{2.48}$$

where $Q_k(s_{\mathrm{I},\zeta})$ and $t_k(s_{\mathrm{I},\zeta})$ are the normal coordinates of the vector and the vibrational turning point for the k-th vibrational mode at $s_{\mathrm{I},\zeta}$, and $(F-1)$ is the number of vibrational modes orthogonal to the motion along the reaction coordinate. $Q_k(s_{\mathrm{I},\zeta})$ can be calculated by projecting the vector onto the k-th vibrational mode,[38,39]

$$Q_k(s_{\mathrm{I},\zeta}) = \left| [\mathbf{a}(\zeta) - \mathbf{a}(s_{\mathrm{I},\zeta})] \cdot \mathbf{L}_k(s_{\mathrm{I},\zeta}) \right|, \tag{2.49}$$

where $\mathbf{L}_k(s_{\mathrm{I},\zeta})$ is the eigenvector corresponding to the k-th vibrational mode at $s_{\mathrm{I},\zeta}$.

Secondly, for any $\zeta \leq \zeta\mathrm{I}$ along the LCT tunnelling path, the point $s_{\mathrm{I},\zeta}$ along the MEP that maps onto ζ has to be between the start and end points of the LCT tunnelling path that lie along the MEP,[38]

$$s_{\mathrm{I},\zeta=0} \leq s_{\mathrm{I},\zeta} \leq s_{\mathrm{I},\zeta=\zeta_p}. \tag{2.50}$$

Thirdly, the point ζ on the LCT tunnelling path has to be in the single-valued region at $s_{\mathrm{I},\zeta}$,[38]

$$\left| \sum_{k=1}^{F-1} B_{k,F}(s_{\mathrm{I},\zeta}) Q_k(s_{\mathrm{I},\zeta}) \right| < 1. \tag{2.51}$$

Similarly, the conditions used to define $\zeta\mathrm{II}$ are given as[38,39]

$$\begin{aligned} & Q_k(s_{\mathrm{II},\zeta}) \leq t_k(s_{\mathrm{II},\zeta}) \\ & s_{\mathrm{II},\zeta=0} < s_{\mathrm{II},\zeta} < s_{\mathrm{II},\zeta=\zeta_p} \\ & \left| \sum_{k=1}^{F-1} B_{k,F}(s_{\mathrm{II},\zeta}) Q_k(s_{\mathrm{II},\zeta}) \right| < 1 \end{aligned}$$

for any $\zeta \geq \zeta\mathrm{II}$. $\zeta\mathrm{II}$ is set to be the value of ζ once any of the conditions is not met.

When $\zeta\mathrm{I} < \zeta\mathrm{II}$, the non-adiabatic region exists and the boundaries between the non-adiabatic region and adiabatic regions are defined as $\zeta\mathrm{I}$ and $\zeta\mathrm{II}$. In order to evaluate the barrier penetration integral, the effective tunnelling potentials in these regions are required. The large-curvature ground state version 3 (LCG3) approximation for the effective tunnelling potential energy in the non-adiabatic region, $V_{\mathrm{LCG3}}(\zeta)$, is given by[39]

$$V_{\mathrm{LCG3}}(\zeta) = V_{\mathrm{PES}}(\zeta) + V\mathrm{I}_{\mathrm{corr}}(\zeta\mathrm{I}) + \frac{\zeta - \zeta\mathrm{I}}{\zeta\mathrm{II} - \zeta\mathrm{I}}[V\mathrm{II}_{\mathrm{corr}}(\zeta\mathrm{II}) - V\mathrm{I}_{\mathrm{corr}}(\zeta\mathrm{I})] \tag{2.52}$$

where $V_{\mathrm{PES}}(\zeta)$ is the potential energy obtained from the PES at ζ and $V\mathrm{I}_{\mathrm{corr}}(\zeta\mathrm{I})$ and $V\mathrm{II}_{\mathrm{corr}}(\zeta\mathrm{II})$ are correction terms for ZPEs at $\zeta\mathrm{I}$ and $\zeta\mathrm{II}$ respectively.

The terms $V\mathrm{I}_{\mathrm{corr}}(\zeta\mathrm{I})$ and $V\mathrm{II}_{\mathrm{corr}}(\zeta\mathrm{II})$ in Eq 2.52 are non-zero if the reacting system is within the turning points of the vibrational modes orthogonal to the motion along the reaction coordinate at $\zeta\mathrm{I}$ and $\zeta\mathrm{II}$. $V\mathrm{I}_{\mathrm{corr}}(\zeta\mathrm{I})$ is calculated by[39]

$$V\mathrm{I}_{\mathrm{corr}}(\zeta\mathrm{I}) = \frac{1}{2}\left[\sum_{k=1}^{F-1} \hbar\omega_k(s_{\mathrm{I},\zeta\mathrm{I}}) - \mu\,\omega_k(s_{\mathrm{I},\zeta\mathrm{I}})^2 Q_k(s_{\mathrm{I},\zeta\mathrm{I}})^2\right] \tag{2.53}$$

where $\omega_k(s_{\mathrm{I},\zeta\mathrm{I}})$ is the vibrational frequency of the k-th vibrational mode orthogonal to the reaction coordinate $s_{\mathrm{I},\zeta\mathrm{I}}$. $V\mathrm{II}_{\mathrm{corr}}(\zeta\mathrm{II})$ is calculated in a similar fashion.

In the adiabatic regions, the effective tunnelling potential at ζ along the LCT tunnelling path would be the same as the adiabatic ground state potential energy at $s_{a,\zeta}$ (where $a =$ I or II). Therefore, Eq 2.45 can be expanded to give,[39,87]

$$\begin{aligned}\theta_{\mathrm{LCT}}(E_i) = &\int_0^{\zeta\mathrm{I}} \sqrt{2\mu(V_{\mathrm{a}}^{\mathrm{G}}(s_{\mathrm{I},\zeta}) - E_i)}\cos\varepsilon_{\mathrm{I},\zeta}\,d\zeta + \\ &\int_{\zeta\mathrm{I}}^{\zeta\mathrm{II}} \sqrt{2\mu(V(\zeta) - E_i)}\,d\zeta + \\ &\int_{\zeta\mathrm{II}}^{\zeta_p} \sqrt{2\mu(V_{\mathrm{a}}^{\mathrm{G}}(s_{\mathrm{II},\zeta}) - E_i)}\cos\varepsilon_{\mathrm{II},\zeta}\,d\zeta\end{aligned} \tag{2.54}$$

where $\varepsilon_{\mathrm{I/II}}$ is the acute angle formed between the tangent vector of the MEP at $s_{\mathrm{I/II}}$ and the

direction vector of the LCT tunnelling path. In the adiabatic regions, the tunnelling occurs along the MEP through the adiabatic ground state potential energy. Therefore, the integrals in these regions are weighted by the projection of the LCT tunnelling path onto the MEP by using the cosine factors in Eq 2.54.[39,87]

With $V_{\mathrm{LCG3}}(\zeta)$ in Eq 2.52, it was found that there was a lack of continuity between the effective tunnelling potentials in the adiabatic regions and non-adiabatic region at the boundaries ζI and ζII.[87] The effective tunnelling potentials of the adiabatic regions in $V_{\mathrm{LCG3}}(\zeta)$ can be (i) larger, or (ii) smaller than that of the non-adiabatic region at the boundaries.[39] This is illustrated in Fig 2.4.

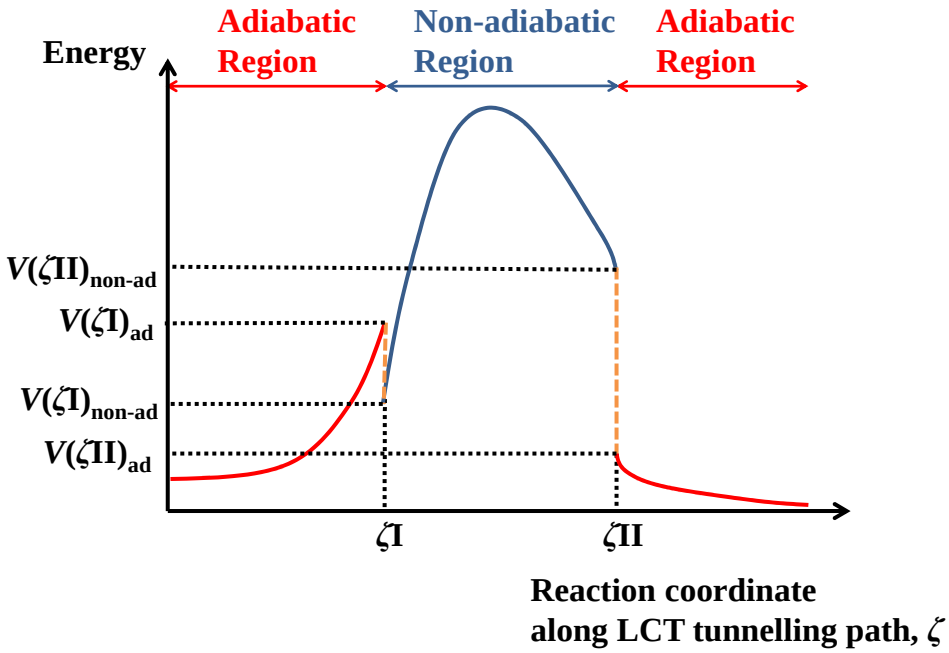


Figure 2.4: Illustration of an example of the energy profile along a LCT tunnelling path. Red and blue curves (with respective labelling) refer to the potential energies in the adiabatic and non-adiabatic regions along the tunnelling path respectively. ζI and ζII are the boundaries for the adiabatic regions in the reactant and product valleys respectively. The effective tunnelling potential of the adiabatic region is larger than that of the non-adiabatic region in the reactant valley, $V_{\mathrm{LCG3}}(\zeta\mathrm{I})_{\mathrm{ad}} > V_{\mathrm{LCG3}}(\zeta\mathrm{I})_{\mathrm{non\text{-}ad}}$, and the effective tunnelling potential of the adiabatic region is smaller than that of the non-adiabatic region in the product valley, $V_{\mathrm{LCG3}}(\zeta\mathrm{II})_{\mathrm{ad}} < V_{\mathrm{LCG3}}(\zeta\mathrm{II})_{\mathrm{non\text{-}ad}}$.

In the LCG4 method,[87] a new condition was added to define new boundaries for the adiabatic regions, $\zeta \mathrm{I}_{\mathrm{new}}$ and $\zeta \mathrm{II}_{\mathrm{new}}$: the effective tunnelling potential energy in the adiabatic regions should be the same as that in the non-adiabatic region at the boundaries,

$$V_{\mathrm{LCG4}}(\zeta \mathrm{I}_{\mathrm{new}})_{\mathrm{ad}} = V_{\mathrm{LCG4}}(\zeta \mathrm{I}_{\mathrm{new}})_{\text{non-ad}}. \tag{2.55}$$

When the effective tunnelling potential at the boundary of the adiabatic region is larger than that of the non-adiabatic region, for example, in the reactant valley in Fig 2.4, the difference in energies is attributed to anharmonicity.[39,87] The anharmonic contribution is given by[39,87]

$$V\mathrm{I}_{\mathrm{anh}} = V_{\mathrm{LCG3}}(\zeta \mathrm{I})_{\mathrm{ad}} - V_{\mathrm{LCG3}}(\zeta \mathrm{I})_{\text{non-ad}}, \tag{2.56}$$

and the new boundary for the adiabatic region is the same as the old,

$$\zeta \mathrm{I}_{\mathrm{new}} = \zeta \mathrm{I}.$$

Similarly, if this situation occurs in the adiabatic region in the product valley, then

$$V\mathrm{II}_{\mathrm{anh}} = V_{\mathrm{LCG3}}(\zeta \mathrm{II})_{\mathrm{ad}} - V_{\mathrm{LCG3}}(\zeta \mathrm{II})_{\text{non-ad}}, \tag{2.57}$$

$$\zeta \mathrm{II}_{\mathrm{new}} = \zeta \mathrm{II}.$$

When the effective tunnelling potential at the boundary of the adiabatic region is smaller than that of the non-adiabatic region, for example, in the product valley in Fig 2.4, the non-adiabatic region is extended out till the point $\zeta \mathrm{II}_{\mathrm{new}}$ where Eq 2.55 is met.[39,87] The same treatment is given to the reactant valley if $V_{\mathrm{LCG3}}(\zeta \mathrm{I})_{\mathrm{ad}} < V_{\mathrm{LCG3}}(\zeta \mathrm{I})_{\text{non-ad}}$.

The expression for the final LCG4 effective tunnelling potential in the non-adiabatic

region is then given by[39,87]

$$V_{\mathrm{LCG4}}(\zeta) = V_{\mathrm{PES}}(\zeta) + V\mathrm{I}_{\mathrm{corr}}(\zeta[\mathrm{I}]) + V\mathrm{I}_{\mathrm{anh}} + \frac{\zeta - \zeta[\mathrm{I}]}{\zeta[\mathrm{II}] - \zeta[\mathrm{I}]}[V\mathrm{II}_{\mathrm{corr}}(\zeta[\mathrm{II}]) - V\mathrm{I}_{\mathrm{corr}}(\zeta[\mathrm{I}]) + V\mathrm{II}_{\mathrm{anh}} - V\mathrm{I}_{\mathrm{anh}}] \tag{2.58}$$

where $\zeta[\mathrm{I}]$ and $\zeta[\mathrm{II}]$ refer to the new boundaries for the adiabatic regions. The LCG4 potential energy barrier is shown together with the LCG3 barrier in Fig 2.5.

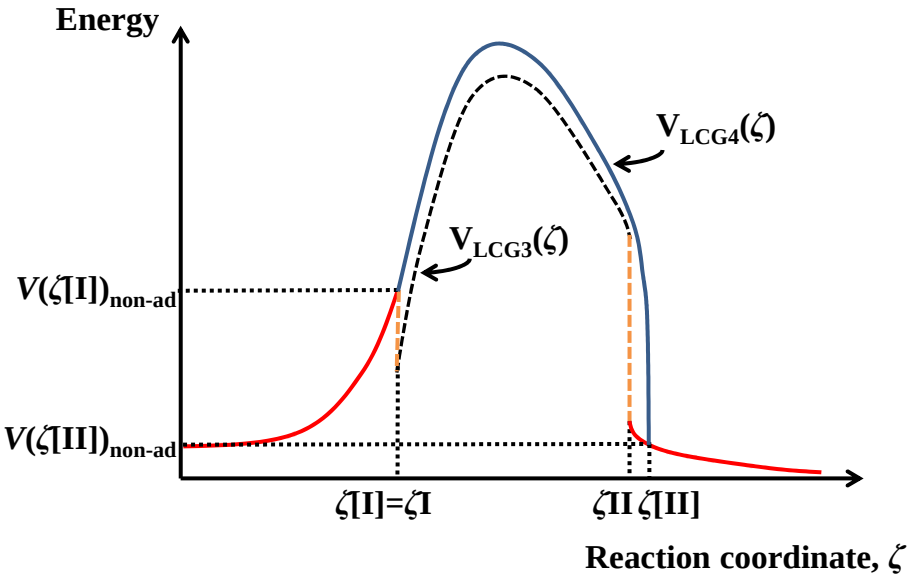


Figure 2.5: Illustration of the energy profile along the LCT tunnelling path in Fig 2.4 with the LCG4 potential energy. Red, blue and dashed black curves refer to the adiabatic, LCG4 and LCG3 potential energy curves respectively. $\zeta\mathrm{I}$ and $\zeta\mathrm{II}$ are the boundaries for the $V_{\mathrm{LCG3}}(\zeta)$ potential, and $\zeta[\mathrm{I}]$ and $\zeta[\mathrm{II}]$ are the boundaries for the $V_{\mathrm{LCG4}}(\zeta)$ potential. $V_{\mathrm{LCG4}}(\zeta[\mathrm{I}])_{\mathrm{ad}} = V_{\mathrm{LCG4}}(\zeta[\mathrm{I}])_{\mathrm{non\text{-}ad}}$ and $V_{\mathrm{LCG4}}(\zeta[\mathrm{II}])_{\mathrm{ad}} = V_{\mathrm{LCG4}}(\zeta[\mathrm{II}])_{\mathrm{non\text{-}ad}}$ using the LCG4 method to approximate the potential energy in the non-adiabatic region.

With the new boundaries, $\zeta[\mathrm{I}]$ and $\zeta[\mathrm{II}]$, and $V_{\mathrm{LCG4}}(\zeta)$, the barrier penetration integral along any LCT tunnelling path can then be calculated by Eq 2.54.

When $\zeta\mathrm{I} \geq \zeta\mathrm{II}$, there is no non-adiabatic region in the LCT tunnelling path. Therefore, the boundaries $\zeta\mathrm{I}$ and $\zeta\mathrm{II}$ do not have to be redefined. The barrier penetration integral is

then given by[39]

$$\theta_{\mathrm{LCT}}(E_i) = \int_0^{\zeta_{\mathrm{II}}} \sqrt{2\mu(V_{\mathrm{a}}^{\mathrm{G}}(s_{\mathrm{I},\zeta}) - E_i)}\,\cos\varepsilon_{\mathrm{I},\zeta}\,d\zeta + \int_{\zeta_{\mathrm{II}}}^{\zeta_{\mathrm{I}}} \sqrt{2\mu(\min\,[V_{\mathrm{a}}^{\mathrm{G}}(s_{\mathrm{I},\zeta}), V_{\mathrm{a}}^{\mathrm{G}}(s_{\mathrm{II},\zeta})] - E_i)}\,\cos\varepsilon_{\zeta_{\mathrm{min}}}\,d\zeta + \int_{\zeta_{\mathrm{I}}}^{\zeta_p} \sqrt{2\mu(V_{\mathrm{a}}^{\mathrm{G}}(s_{\mathrm{II},\zeta}) - E_i)}\,\cos\varepsilon_{\mathrm{II},\zeta}\,d\zeta. \tag{2.59}$$

where $\varepsilon_{\zeta_{\mathrm{min}}}$ is the corresponding angle for the chosen adiabatic ground state potential in the integral.

Tunnelling along the LCT tunnelling path can be initiated both by motion along the MEP and along the orthogonal vibrational modes. For the former, the tunnelling amplitude is simply weighted by the angle the tunnelling path makes with the tangent of the MEP at reaction coordinate s_E corresponding to energy E,[39]

$$T_{\mathrm{MEP}}(E) = \exp[-\theta(E)]\,\cos\varepsilon(s_E) \tag{2.60}$$

where $\exp[-\theta(E)]$ is the primitive tunnelling amplitude for the LCT tunnelling path. For the initiation of tunnelling by the motion along the vibrational modes that are orthogonal to the MEP, the tunnelling amplitude is also weighted by the same angle,[39]

$$T_{\mathrm{vib}}(E) = \exp[-\theta(E)]\,\sin\varepsilon(s_E). \tag{2.61}$$

When the reacting system has a particular energy, E_i, tunnelling can also be initiated by motion along the vibrational modes orthogonal to the MEP for all $E \leq E_i$.[38,39] Therefore, the total tunnelling amplitude due to vibrational motions at E_i is an accumulation of all the tunnelling amplitudes where $E \leq E_i$. Since any energy E_i corresponds to a point on the MEP with reaction coordinate s_{E_i}, the tunnelling amplitude at energy E_i can be expressed

as,[39]

$$T_{\text{vib}}(E_i) = \int_{-\infty}^{s_{E_i}} \left[\frac{\exp[-\theta(s_E)] \sin \varepsilon(s_E)}{\nu(s_E)\tau(s_E)} \right] ds_E \tag{2.62}$$

where $\nu(s_E)$ is the speed at which the reacting system travels past a point s_E along the MEP, and $\tau(s_E)$ is the vibrational period of the effective vibrational frequency at s_E. In Eq 2.62, $ds_E/\nu(s_E)$ gives the amount of time spent by the reacting system between s_E and $(s_E + ds_E)$, and $1/\tau(s_E)$ gives the number of times that the reacting system collides with the turning point of effective the vibrational mode per unit time.[39] Therefore, the combination of both terms gives the total number of times the reacting system collides with the turning point of the effective vibrational mode within the time where it travels from s_E to $(s_E + ds_E)$.

The speed of travel past s_E, $\nu(s_E)$, and the vibrational period at s_E, $\tau(s_E)$, are given by[39]

$$\nu(s_E) = \left[\frac{2}{\mu} (E - V_{\text{a}}^{\text{G}}(s_E)) \right]^{1/2} \tag{2.63}$$

$$\tau(s_E) = \frac{2\pi}{\omega_{\text{eff}}(s_E)} \tag{2.64}$$

where $\omega_{\text{eff}}(s_E)$ is the effective vibrational frequency of the vibrational modes at s_E evaluated along the LCT tunnelling path. $\omega_{\text{eff}}(s_E)$ has contributions from the vibrational frequencies from the vibrational modes at s_E and is given by[39]

$$\omega_{\text{eff}}(s_E) = \left[\sum_{k=1}^{F-1} [\omega_k(s_E) q_k(s_E)]^2 \right]^{1/2} \tag{2.65}$$

where $\omega_k(s_E)$ is the vibrational frequency of the k-th vibrational mode at s_E and $q_k(s_E)$ is the k-th component of the unit vector along the projected path. It can be expressed by[39]

$$q_k(s_E) = \frac{\mathbf{n}(s_E) \cdot \mathbf{L}_k(s_E)}{\left[\sum_{k=1}^{F-1} [\mathbf{n}(s_E) \cdot \mathbf{L}_k(s_E)]^2 \right]^{1/2}} \tag{2.66}$$

where **n** is the unit vector along the tunnelling path,[38]

$$\mathbf{n} = \frac{\mathbf{a}(\zeta_p) - \mathbf{a}(\zeta_0)}{|\mathbf{a}(\zeta_p) - \mathbf{a}(\zeta_0)|}. \tag{2.67}$$

The total transmission probability at energy E with both contributions from the motion along the MEP and the vibrational mode orthogonal to the MEP is then given by[81]

$$P_{\text{prim}}(E) = [T_{\text{vib}}(E)]^2 + [T_{\text{MEP}}(E)]^2 \tag{2.68}$$

where $P_{\text{prim}}(E)$ is the primitive transmission probability at energy E.[39] This transmission probability is then uniformised in order to take into account non-classical reflection,[81]

$$P(E) = \begin{cases} 0 & \text{if } E < E_0 \\ \left[1 + \dfrac{P_{\text{prim}}(E)(P_{\text{prim}}(V_{\text{a}}^{\text{Gmax}})^{-1} - 1)}{P_{\text{prim}}(V_{\text{a}}^{\text{Gmax}})^{-1}}\right]\left[\dfrac{P_{\text{prim}}(E)}{P_{\text{prim}}(E)+1}\right] & \text{if } E_0 \leq E \leq V_{\text{a}}^{\text{Gmax}} \\ 1 - P(2V_{\text{a}}^{\text{Gmax}} - E) & \text{if } V_{\text{a}}^{\text{Gmax}} \leq E \leq 2V_{\text{a}}^{\text{Gmax}} - E_0 \\ 1 & \text{if } E > 2V_{\text{a}}^{\text{Gmax}} - E_0 \end{cases} \tag{2.69}$$

The assumption in the above sections is that the PES provides sufficient information allowing calculations within the whole range of the MEP from reactants to products, and in the reaction swath. However, there might be insufficient information at times, or it might be computationally too expensive to calculate all quantities required.[39] In such cases, the missing information can be estimated from available information by the mapped interpolation (MI) method.

2.2.5 Mapped Interpolation

In order to achieve computational efficiency, the MI method interpolates the properties along the MEP by mapping the reaction coordinate s with an infinite range $-\infty < s < \infty$

from reactants to products to a variable z with a finite range $-1 < z < 1$.[39,124] Such mapping is necessary such that interpolation is possible for the range where there is no available data.

The mapping is done using the expression,[124]

$$z = \frac{2}{\pi}\tan^{-1}\left[\frac{s - s_0}{L}\right], \tag{2.70}$$

where s_0 is the s value where changes in the potential is important along the reaction coordinate, and L is the width of the reaction path. The values of s_0 and L are given by[124]

$$s_0 = \frac{s_R + s_P}{2}$$
$$L = \frac{s_P - s_R}{2}$$

where s_R and s_P are defined as[124]

$$s_R = -\min(-s_{R,0}, 2s_{P,0}), \quad s_P = \min(-s_{R,0}, s_{P,0}).$$

$s_{R,0}$ is the reaction coordinate in the reactant valley where its potential is halfway between that of the reactants and transition state, and $s_{P,0}$ is the corresponding point in the product valley.

If the reaction coordinate values $s_{R,0}$ and $s_{P,0}$ are not available, they can be obtained by the following method. The potential energy at $s_{R,0}$ can be calculated using the quadratic expansion using the imaginary frequency at the transition state,[124]

$$V_{\mathrm{MEP}}(s_{R,0}) = V_{\mathrm{MEP}}(0) - \frac{1}{2}\mu|\omega(0)|^2 s_{R,0}^2 \tag{2.71}$$

where $s = 0$ corresponds to the reaction coordinate for the transition state, and $\omega(0)$ is the imaginary frequency of the transition state. Since the potential energy at $s_{R,0}$ is halfway between that of the reactants and the transition state, its potential energy can also be expressed

as

$$V_{\mathrm{MEP}}(s_{R,0}) = V_{\mathrm{MEP}}(0) - \frac{V_{\mathrm{MEP}}(0) - V_{\mathrm{MEP}}(s_{-\infty})}{2}. \tag{2.72}$$

By equating Eq 2.72 to Eq 2.71 we obtain[39,124]

$$s_{R,0} = -\left[\frac{V_{\mathrm{MEP}}(0) - V_{\mathrm{MEP}}(s_{-\infty})}{\mu|\omega(0)|^2}\right]^{1/2}. \tag{2.73}$$

Similarly, for the calculation of $s_{P,0}$, we get[39,124]

$$s_{P,0} = \left[\frac{V_{\mathrm{MEP}}(0) - V_{\mathrm{MEP}}(s_{\infty})}{\mu|\omega(0)|^2}\right]^{1/2}. \tag{2.74}$$

The MI algorithm will now be described briefly for the calculation of $V_{\mathrm{MEP}}(s)$.[124] Within the range of the MEP where information is available, W number of points were chosen at equal intervals. With additional information from the transition state, reactants and products, the total number of data points available is $(W+3)$. Without loss of generality, when $s_{R,f}$ and $s_{P,f}$ are the final (f) points of calculation in the reactant (R) and product (P) valleys respectively, information on the PES is not available between $s_{-\infty} < s < s_{R,f}$ and $s_{P,f} < s < s_{\infty}$. In these ranges where there is no data, the potential energies at 10 additional points in each of the ranges were interpolated using Eckart potentials. The Eckart potential can be expressed as[124,125]

$$V_{\mathrm{MEP}}(s) = \frac{AY}{1+Y} + \frac{BY}{(1+Y)^2}. \tag{2.75}$$

The parameters A, B, and Y are given by[124]

$$\begin{aligned}
A &= V_{\mathrm{MEP}}(s_{\infty}),\\
B &= 2V_{\mathrm{MEP}}(0) - A + 2\left[V_{\mathrm{MEP}}(0)(V_{\mathrm{MEP}}(0) - A)\right]^{1/2},\\
Y &= \exp\left[\frac{s}{L^{\mathrm{eck}}(s)} + \ln(A+B) - \ln(B-A)\right],
\end{aligned}$$

where $L^{\text{eck}}(s)$ is the characteristic length of the Eckart potential at the reaction coordinate s along the MEP. All energies given are with respect to the energy of the reactants, i.e. $V_{\text{MEP}}(s_{-\infty}) = 0$. The Eckart potential at any particular non-stationary point along the MEP amongst the chosen W non-stationary points, also passes through the transition state, reactants and products by construction.[124] Therefore, $L^{\text{eck}}(s)$ can be found at these non-stationary points. At the transition state, $L^{\text{eck}}(0)$ is given by,[124]

$$L^{\text{eck}}(0) = \left[\frac{2V_{\text{MEP}}(0)(V_{\text{MEP}}(0) - A)}{B\mu|\omega(0)|^2}\right]^{1/2}. \tag{2.76}$$

With $L^{\text{eck}}(s)$ in the range $s_{R,f} < s < s_{P,f}$, $L^{\text{eck}}(z)$ for the corresponding range can then calculated by using the mapping function in Eq 2.70.[39,124] The values of $L^{\text{eck}}(-1)$ and $L^{\text{eck}}(1)$ for the reactants and products respectively are then extrapolated from the function $L^{\text{eck}}(z)$. The $L^{\text{eck}}(z)$ values for the additional 10 points on the reactant and product valleys are then interpolated to obtain $L^{\text{eck}}(z)$ for the range $-1 \leq z \leq 1$. Finally, the potential energies of the $(W + 23)$ can then be calculated using Eq 2.70 and Eq 2.75. A spline function was then fitted to the $(W + 23)$ points so that the potential energy at any s along the MEP can be calculated.[39,124] Similarly, other quantities required in the computation of the transmission probabilities can also calculated using the MI method if they are not available.[39,124] With such interpolation method, it would be possible to have the MEP and its respective adiabatic ground state potential energy curve from the reactants to products which is required for MT calculations.

The different TST/MT methods (ZCT, SCT and LCT) that approximate accurate quantum reactive scattering calculations had been tested against accurate quantum reactive scattering results calculated on the same surfaces for diatom-atom reactions,[86] but have not been thoroughly evaluated in comparison with more accurate calculations on polyatomic reactions that are more complex. Therefore, in order to further test the accuracy of the TST/MT methods on these reactions, the TST/MT methods were adapted and applied to

the PESs constructed using the so-called reduced dimensionality (RD) method for hydrogen abstraction and hydrogen exchange reactions. Therefore, a brief outline of the RD method, in particular, the 2D RD PES formulation for collinear reactions will be given in the next section.

2.3 Reduced Dimensionality

2.3.1 Reduced Dimensionality Potential Energy Surfaces

In the construction of a PES for the calculation of reaction rate constants, it is often computationally expensive to construct a full-dimensional PES.[97] One of the methods used to overcome such issue is to use the so-called Reduced Dimensionality (RD) method.[96,97,101,102] In this method, only a subset of internal degrees of freedom is explicitly considered. All other internal degrees of freedom are treated as spectator modes where their contributions are included in the potential energy functions as ZPEs.[102–105] In the reactions studied in this project, there is only the breaking and forming of one bond each as the reaction proceeds from the reactants to products, and the geometry along the MEP is collinear.[109,110,112,113] This suggests that the internal degrees of freedom that are the most important and should be treated explicitly are the ones that correspond to the chemical bonds that were formed and broken in a collinear fashion. This simplifies the evaluation for a polyatomic reacting system mapped onto a diatom-atom (AB-C) reacting system illustrated in Fig 2.6.

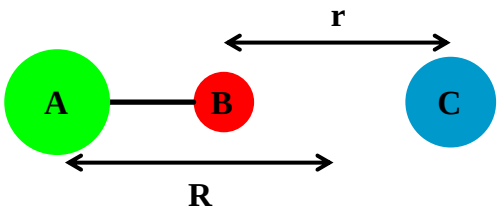


Figure 2.6: Diatom-atom (AB-C) reacting system with Jacobi coordinates R and r defined as the distance between the centre of mass of the reacting atom in A to the centre of mass of BC, and the distance between B and C respectively.

Figure 2.6 illustrates the simplification of the polyatomic reacting system to a diatom-atom reacting system where the internal degrees of freedom that are treated explicitly are the breaking of bond A-B and the forming of bond B-C, and the ABC complex is collinear throughout the MEP. As a result, we only consider the movement of the pseudo-atoms[115] along the x-direction and align them such that the axis of collinearity is parallel to the x-axis. Since the pseudo-atom A in Figure 2.6 is in reality a polyatomic molecule, we consider the Jacobi coordinate R only from the centre of mass of the atom that is directly bonded to atom B. The Jacobi coordinates are given by[112]

$$\mathrm{R} = \left| \left(\frac{m_\mathrm{B} x_\mathrm{B} + m_\mathrm{C} x_\mathrm{C}}{m_\mathrm{B} + m_\mathrm{C}} - x_\mathrm{A} \right) \right|, \quad \mathrm{r} = |(x_\mathrm{C} - x_\mathrm{B})| \tag{2.77}$$

where $m_\mathrm{A}, m_\mathrm{B}$ and m_C are the masses of pseudo-atom A, atom B and pseudo-atom C, and $x_\mathrm{A}, x_\mathrm{B}$ and x_C are their corresponding Cartesian coordinates in the x-direction. The Jacobi coordinates are then used to convert to hyperspherical coordinates, ρ and δ,[112]

$$\frac{m_1}{\mu}\mathrm{R}^2 = (\rho \cos[\delta])^2, \quad \frac{m_2}{\mu}\mathrm{r}^2 = (\rho \sin[\delta])^2. \tag{2.78}$$

where the definition of m_1, m_2, and μ can be found in the literature.[107,110,112,113]

In the formulation of the 2D PESs, the motion along the two vibrational modes that were explicitly treated were first projected out from the mass-weighted Hessian.[107,110,112,113] Vibrational analysis was then carried out on the post-projection mass-weighted Hessian to obtain the ZPEs from the other vibrational modes. The ZPEs were subsequently added to the *ab initio* single-point energies to get the energies of the grid points used in the fitting of the 2D PESs in hyperspherical coordinates.[107,110,112,113] These 2D PESs were used in quantum reactive scattering (QRS) calculations[109,110,112,113] to give benchmark results to test the various TST/MT methods for a variety of reactions of polyatomic molecules in this thesis.

2.3.2 Reduced Dimensionality-Adapted Calculations

Using the 2D PESs described in the previous section, the MEP was then obtained for subsequent calculations of the tunnelling corrections. Since the 2D PESs were defined in hyperspherical coordinates[107,110,112,113] and the derivatives required to calculate the MEP by the steepest descent method were expressed in mass-weighted Cartesian coordinates,[39] the steepest descent algorithm had to be adapted to the RD nature of the PES.

In the RD PES, only the breaking of AB bond and the forming of BC bond (in Fig 2.6) along the axis of collinearity are explicitly considered.[107,110,112,113] Therefore, in the definition of the Cartesian coordinates of the diatom-atom reaction, only 1 of the coordinates has a non-zero value. Without loss of generality, we set this coordinate to be the x-coordinate. Therefore, the mass-weighted Cartesian coordinate vector has the form of

$$\mathbf{a} = \begin{bmatrix} \sqrt{m_{\mathrm{A}}} A_{\mathrm{A},x} & 0 & 0 \\ \sqrt{m_{\mathrm{B}}} A_{\mathrm{B},x} & 0 & 0 \\ \sqrt{m_{\mathrm{C}}} A_{\mathrm{C},x} & 0 & 0 \end{bmatrix}$$

where columns 2 and 3 are the y- and z coordinates of pseudo-atoms A, B and C.

In the calculation of the derivative $dV/d\mathbf{a}$, we first calculate the derivative of the RD PES with respect to the non-mass-weighted Cartesian coordinate by using the chain rule. The relationship of the terms in the derivation of the derivative is summarised in Figure 2.7.

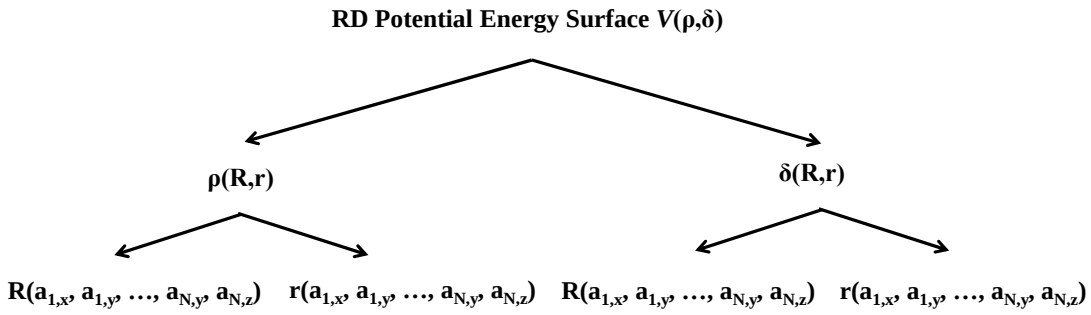


Figure 2.7: Flowchart of the dependencies of the RD PES from hyperspherical coordinates to non-mass-weighted Cartesian coordinates.

By the chain rule, the derivative of the RD PES with respect to the non-mass-weighted Cartesian x-coordinate, $a_{i,x}$, is

$$\frac{dV}{dA_{i,x}} = \frac{dV}{d\rho}\left[\frac{d\rho}{dR}\frac{dR}{dA_{i,x}} + \frac{d\rho}{dr}\frac{dr}{dA_{i,x}}\right] + \frac{dV}{d\delta}\left[\frac{d\delta}{dR}\frac{dR}{dA_{i,x}} + \frac{d\delta}{dr}\frac{dr}{dA_{i,x}}\right]. \tag{2.79}$$

Since the RD PES considers only the movement parallel to the x-axis, the derivatives of the RD PES with respect to all y and z coordinates is equal to 0, i.e.

$$\frac{dV}{dA_{i,y}} = \frac{dV}{dA_{i,z}} = 0. \tag{2.80}$$

The non-mass-weighted gradient is then mass-weighted to give the mass-weighted gradient,

$$\frac{dV}{da_{i,x}} = \frac{1}{\sqrt{m_i}}\frac{dV}{dA_{i,x}}. \tag{2.81}$$

This RD-adapted mass-weighted gradient is then used to calculate the MEP.

In the calculation of the adiabatic ground state potential energy along the MEP, the vibrational frequencies of the modes orthogonal to the MEP are required.[39] In the 2D PES, there are two vibrational modes.[102–105] Since one of these vibrational modes corresponds to the motion along the reaction coordinate, there is only one vibrational mode orthogonal to the reaction coordinate at any s along the MEP. Its vibrational frequency is the sole con-

tributor to the ZPE at that s. This vibrational frequency can be calculated by diagonalising the post-projection mass-weighted Hessian at s.[120,121]

Since we employ the use of a RD PES where we only consider motion parallel to the x-axis, in the pre-projection mass-weighted Hessian, all second derivatives containing any y or z terms are equal to 0. By means of illustration, we remove all the zero terms from the pre-projection mass-weighted Hessian, and it has the form of

$$\frac{d^2V}{d\mathbf{a}^2} = \begin{bmatrix} \frac{d^2V}{dA_{\mathrm{A},x}^2}\frac{1}{\sqrt{m_\mathrm{A}m_\mathrm{A}}} & \frac{d^2V}{dA_{\mathrm{A},x}dA_{\mathrm{B},x}}\frac{1}{\sqrt{m_\mathrm{A}m_\mathrm{B}}} & \frac{d^2V}{dA_{\mathrm{A},x}dA_{\mathrm{C},x}}\frac{1}{\sqrt{m_\mathrm{A}m_\mathrm{C}}} \\ \frac{d^2V}{dA_{\mathrm{A},x}dA_{\mathrm{B},x}}\frac{1}{\sqrt{m_\mathrm{A}m_\mathrm{B}}} & \frac{d^2V}{dA_{\mathrm{B},x}^2}\frac{1}{\sqrt{m_\mathrm{B}m_\mathrm{B}}} & \frac{d^2V}{dA_{\mathrm{B},x}dA_{\mathrm{C},x}}\frac{1}{\sqrt{m_\mathrm{A}m_\mathrm{C}}} \\ \frac{d^2V}{dA_{\mathrm{A},x}dA_{\mathrm{C},x}}\frac{1}{\sqrt{m_\mathrm{A}m_\mathrm{C}}} & \frac{d^2V}{dA_{\mathrm{B},x}dA_{\mathrm{C},x}}\frac{1}{\sqrt{m_\mathrm{B}m_\mathrm{C}}} & \frac{d^2V}{dA_{\mathrm{C},x}^2}\frac{1}{\sqrt{m_\mathrm{C}m_\mathrm{C}}} \end{bmatrix}. \quad (2.82)$$

The procedure for projection then follows from Sec. 2.2.2.[120,121] The post-projection vibrational frequency of the mode orthogonal to the motion along the reaction coordinate can then be calculated and its ZPE added to $V_{\mathrm{MEP}}(s)$ to obtain $V_\mathrm{a}^\mathrm{G}(s)$.[39] This RD-adapted adiabatic ground state potential energy curve is then used to calculate the tunnelling corrections by using the RD-adapted MT methods.

We note here that the resulting RD MEP and RD adiabatic ground state potential energy curve will be different from the MEP and adiabatic ground state potential energy curve directly calculated from full-dimensional calculations. Such differences arise due to the initial projection carried out to formulate the RD PES before any further MEP or ZPE calculations were done.

After obtaining the relevant properties required to calculate the MT transmission coefficients using the RD PESs, the transmission coefficients can then be calculated using the methods previously described in Sec. 2.2.3 and Sec. 2.2.4.

Chapter 3

Computational Details

3.1 Reduced Dimensionality-Adapted Program

The computer program, POLYRATE,[116] is often used[84,126,127] to compute reaction rate constants using the methods described in the previous chapter: zero-, small- and large-curvature tunnelling (ZCT, SCT and LCT respectively). However, in order to better facilitate the use of the reduced dimensionality potential energy surfaces (RD PES)[109,110,112,113] considered in this thesis, a program, RDPOLY, was developed and written using Mathematica 9.0.[128] This also enabled more control over the intermediate steps in the calculations, which helped in the analysis of results.

In RDPOLY, results can be presented graphically without needing to export data to other computer programs for analysis. This provides the convenience of performing calculations and analysing the results in the same program. Also, the gradients and Hessians required can be calculated analytically at all points on the RD PESs, in particular, along the minimum energy path (MEP). This reduces numerical error when the vibrational frequencies at points along the MEP are evaluated. Another consequence is that stationary points can be found analytically on the RD PES. This enables the search for the reactants and products on the RD PESs for subsequent calculation of the transmission coefficients.

The reactants and products had to be found on the RD PESs analytically as the MEP calculated from the transition state (TS) by the steepest descent method led to vibrational frequencies that were physically not meaningful beyond a range of the reaction coordinate, $s_{R,f} \leq s \leq s_{P,f}$ (as defined in Sec. 2.2.5). The RD PESs were also not fully sampled within its range of validity as described in the literature.[109,110,112,113] With the reactants and products of the RD PESs calculated at the maximum ρ validity (where ρ is the hyperspherical coordinate on the RD PESs defined in Eq 2.78), the vibrational frequencies between the stationary points and $s_{R/P,f}$ could be interpolated by the mapped interpolation (MI) method (as described in Sec. 2.2.5) in RDPOLY. Another consequence of employing MI in RDPOLY was the ability to sample the full RD PESs which allowed direct comparison between multi-dimensional tunnelling (MT) with the RD quantum reactive scattering (QRS) within the same validity on the RD PESs.[109,110,112,113]

In order to calculate the final reaction rate constants, the TST rate constant was multiplied to the transmission coefficient calculated from the RD PESs in RDPOLY. Another method that could be used with multi-dimensional tunnelling (MT) is the canonical variational transition state theory (CVTST).[39] In CVTST, a generalised transition state is calculated as the point along the MEP that minimises Eq 2.1 with its corresponding barrier height and partition functions.[39] However, the MEP of the RD PESs only considered explicitly the active modes described in Sec. 2.3. Therefore, the vibrational frequencies of the spectator modes and geometry of the generalised transition state could not be calculated on the RD PESs. As a result, the partition functions and CVTST reaction rate constants could not be evaluated as well. Even though CVTST may improve TST calculations by accounting for most of the recrossing effects,[39] it was not used in this study.

To ensure the accuracy in coding, results from RDPOLY were compared against those from POLYRATE for reaction R1, $CH_4 + H$.

3.1.1 Transition State Properties

In the diatom-atom assumption described in Sec. 2.3, the structure of the transition state (TS) is illustrated in Fig 3.1.

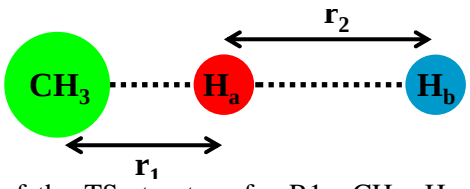


Figure 3.1: Illustration of the TS structure for R1. CH_3, H_a and H_b are the pseudo-atom (as described in Sec. 2.3), abstracted hydrogen and abstracting hydrogen respectively. r_1 is the distance between the centre of mass of the carbon atom in CH_3 to the centre of mass of H_a and r_2 is the distance from the centre of mass of H_a to the centre of mass of H_b.

The properties of the TS calculated by both RDPOLY and POLYRATE for the same RD PES[112] are given in Table 3.1.

Table 3.1: Properties of the TS calculated by RDPOLY and POLYRATE using the RD PES for R1.[112] $V^{\ddagger}$ is the energy of the TS with respect to the energy of the reactants on the RD PES.

	RDPOLY	POLYRATE
r_1/bohr	2.70	2.70
r_2/bohr	1.77	1.77
$V^{\ddagger}$/kcal mol^{-1}	16.4	16.4
Frequency/cm^{-1}	1361	1358
	1793i	1789i

From Table 3.1, r_1 and r_2 calculated by RDPOLY and POLYRATE are identical to each other. This shows that the TS obtained by both programs have the same collinear structure. With the same energies with respect to the energy of the reactants, they produced the same barrier heights for the reaction. The real and imaginary frequencies are also in excellent agreement with each other. These suggest that the adiabatic ground state potential energies and the width of the adiabatic ground state potential energy curves at the TS are the same in both programs. With such comparison of the properties, it is proposed that the TS calculated by RDPOLY for R1 is sufficiently accurate.

3.1.2 Minimum Energy Path

Starting from the TS, the MEP was calculated using the steepest descent method as previously described in Sec. 2.2.2 towards the reactants and products. Since the TS is a stationary point where the gradient is zero, the first step taken from the TS was in the direction of the eigenvector which corresponded to its imaginary frequency.[39] In both RDPOLY and POLYRATE, this normalised eigenvector was calculated to be {-0.194, 0.958, -0.210}, where the three values corresponded to the movements of the CH_3 pseudo-atom, H_a and H_b in the x-direction respectively within the RD framework (as described in Sec. 2.3). The MEP and adiabatic ground state potential energy curve were then subsequently calculated using the methods previously described in Sec. 2.2.2 and Sec. 2.3. The potential energy and adiabatic ground state potential curves along the MEP are given in Fig 3.2.

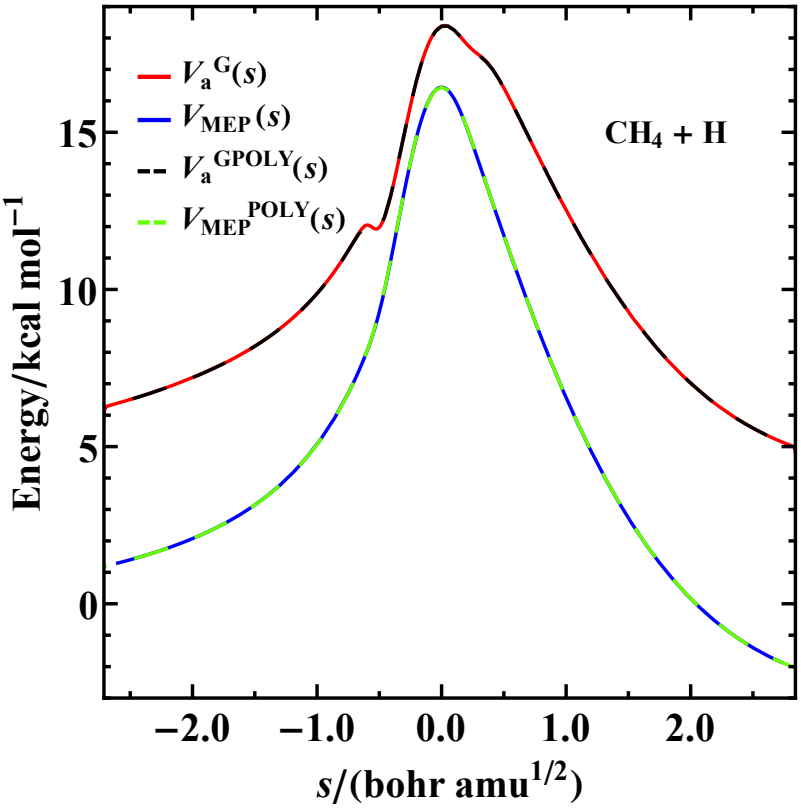


Figure 3.2: An illustration of the adiabatic ground state potential energy and potential energy curves along the MEP calculated by RDPOLY (red and blue respectively) and POLYRATE (black and green respectively) in the range -2.60 bohr amu$^{1/2} \leq s \leq$ 2.73 bohr amu$^{1/2}$.

From Fig 3.2, the potential energy and adiabatic ground state potential energy curves for both programs are in excellent agreement with each other. This suggests that RDPOLY is accurate when calculating the MEP and vibrational frequencies using the RD PES.[112] It is noted that beyond the range of reaction coordinate in Fig 3.2, the vibrational frequencies were physically not meaningful and the MI method was required for further calculations. To our best knowledge, such correction is not possible in POLYRATE. Hence, no such comparison was done between RDPOLY and POLYRATE.

3.1.3 Reaction Rate Constants

Within the range of the reaction coordinate shown in Fig 3.2 where the vibrational frequencies are physically meaningful, the reaction rate constants were calculated using RDPOLY and POLYRATE for ZCT, SCT and LCT. The results are shown in Fig 3.3. From Fig 3.3, the reaction rate constants for R1 calculated using ZCT, SCT and LCT in RDPOLY are in excellent agreement to those calculated by POLYRATE. These results suggest that RDPOLY is accurate within the range of validity of the steepest descent method. Therefore, this approach was subsequently used to extend the range of the MEP for calculations of R1 and was also used to compute the reaction rate constants for reactions R2–R6 (previously given in Chapter 1). The results for reactions R1–R6 will be compared with QRS reaction rate constants and available experimental data in the following chapters.

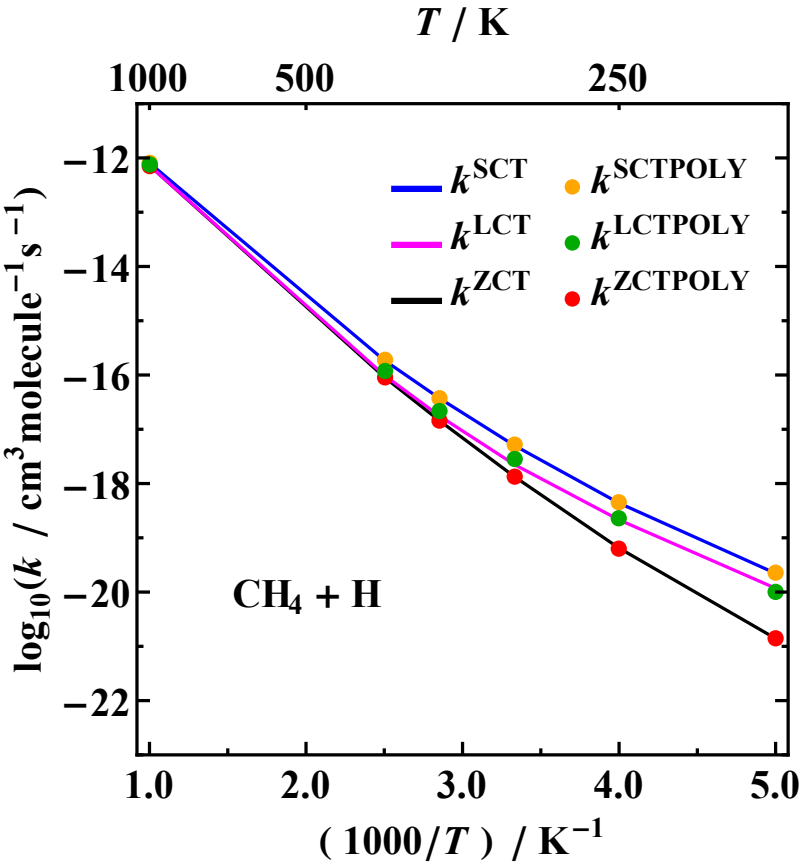


Figure 3.3: Plots of the reaction rate constants in logarithmic scale against 1000/T for R1 calculated within the range of -2.60 bohr amu$^{1/2} \leq s \leq$ 2.73 bohr amu$^{1/2}$. SCT, LCT and ZCT results calculated by RDPOLY are represented by blue, pink and black lines respectively, and the same results calculated by POLYRATE are represented by yellow, green and red dots respectively.

3.2 Potential Energy Surfaces

The RD PESs[109,110,112,113] used in the RDPOLY calculations which were previously constructed for QRS calculations are briefly described next. Geometry optimisations and single point energies of grid points used in the construction of the RD PESs were calculated using Gaussian[129] and MOLPRO.[130] For R1–R6, geometry optimisations were calculated using second order Møller-Plesset perturbation theory (MP2)[129,130] with a correlation consistent polarised valence triple-ζ Dunning basis set[131] (cc-pVTZ). The coupled cluster with single, double and perturbative triple excitations [CCSD(T)] level of theory with the cc-pVTZ basis set[129,130] was then used to calculate the single point energy at each optimised ge-

ometry for R1, R2 and R4–R6; for R3, the explicitly correlated coupled cluster level of theory, CCSD(T)-F12a,[132] was used with the cc-pVTZ-F12 basis set.[133] Details of these calculations, the resulting potential energy functions and their corresponding coefficients for R1–R6 can be found in the literature.[109–113]

Chapter 4

Hydrogen Abstraction Reactions

Reaction rate constants of selected hydrogen abstraction and hydrogen exchange reactions were calculated in RDPOLY (as described in the previous chapter) using Transition State Theory with multi-dimensional tunnelling (TST/MT) applied to the so-called reduced dimensionality potential energy surfaces (RD PES). They are then compared with TST rate constants to study the importance of quantum effects such as quantum tunnelling, then with reaction rate constants obtained from quantum reactive scattering (QRS) calculations to study the extent in which TST/MT accounted for such quantum effects, and finally with available experimental data.

In this chapter, we focus the discussion on hydrogen abstraction reactions, where a hydrogen atom is removed from a stable molecule using an atom or radical.[134] The three reactions studied from this group were,[109,111–113]

$$CH_4 + H \longrightarrow CH_3 + H_2 \tag{R1}$$

$$C_2H_6 + H \longrightarrow C_2H_5 + H_2 \tag{R2}$$

$$\text{cyc-}C_3H_6 + H \longrightarrow \text{cyc-}C_3H_5 + H_2. \tag{R3}$$

The TST/MT methods tested on these systems were TST with zero- and small-curvature

tunnelling (TST/ZCT and TST/SCT respectively) due to the small reaction path curvature of the PESs of these reactions. In the discussion, two types of results will be presented: calculations without mapped interpolation (MI) implemented and calculations with MI. We show the limitations of the calculations without MI and subsequently the improvements made to the results with MI due to the corrections made by using information at the reactants and products on the RD PESs.

4.1 $CH_4 + H \longrightarrow CH_3 + H_2$

The reaction of hydrogen with methane has been widely studied experimentally[135–137] and theoretically[138–143] over the years. It has also become a benchmark reaction used to test approximate theoretical methods for polyatomic reactions against available experimental data or accurate quantum mechanical rate constants.[112,138] This is attributed to its importance in the process of combustion and its small size of the reacting system.[107,144] It is also one of the simplest reaction that involves a hydrocarbon.[107] As a result, its kinetic and dynamical properties are well-known in the literature,[112,135–143] and it is a good reaction that can be used to test the TST/MT method applied to the previously constructed RD PES.[112] The RD PES used in this test treated the spectator modes in curvilinear coordinates and was previously reported by Banks *et al.*[112] (Table I in paper). The calculations were first performed without using MI, then with MI to study the differences between the two methods.

4.1.1 Without Mapped Interpolation

4.1.1.1 Minimum Energy Path

The minimum energy path (MEP) was calculated using the RD PES reported by Banks *et al.*[112] from the transition state (TS) to the reactants and products using Euler's steepest descent method.[39] Due to the formulation of the RD PES,[112] only two internal degrees of

freedom corresponding to the breaking and forming of one bond each along the MEP were explicitly considered as described previously in Sec. 2.3. Since one of the internal degrees of freedom was the vibrational motion along the reaction coordinate, there was only one vibrational mode orthogonal to the reaction coordinate that contributed to the zero point energy (ZPE) at the TS. The coordinates of the TS on the RD PES and this vibrational frequency are given in Table 4.1.

Table 4.1: Properties of the TS on the RD PES[112] for $CH_4 + H$.

$\{\rho$/bohr, δ/rad$\}$	Frequency/cm^{-1}
{4.35, 0.258}	1361

For the calculation of the MEP from the TS, the number of steps taken in each direction was 1000 with stepsize 0.01 bohr amu$^{1/2}$. The resulting MEP is shown on the RD PES in Fig 4.1. The contour plot in Fig 4.1 was plotted based on the validity of the range of ρ used in the R-matrix propagation, i.e. 3.6 bohr $\leq \rho \leq$ 30 bohr.[112] In Fig 4.1, the reactant valley of the RD PES corresponds to points along the MEP where their δ values are larger than that of the TS, i.e. $\delta > 0.258$ rad; points along the MEP where $\delta < 0.258$ rad correspond to the product valley. From Fig 4.1, it is seen that the maximum validity of the RD PES was not attained in the MEP calculations, i.e. the MEP calculated did not reach a value of $\rho = 30$ bohr in both the reactant and product asymptotic regions. When the number of steps taken in the calculation of the MEP doubled, there was no significant change in the MEP calculated as well.

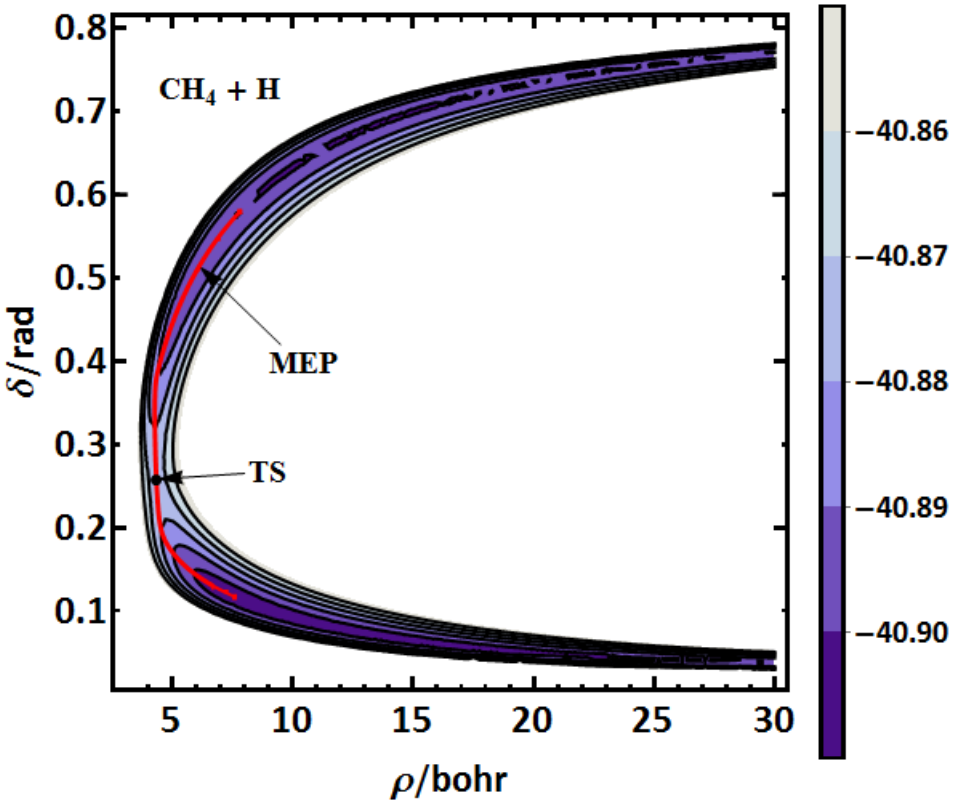


Figure 4.1: The contour plot of the RD PES of R1 by Banks *et al.*[112] with the spectator modes treated in curvilinear coordinates. Black dot is the TS on the RD PES and red curve is the MEP calculated from the TS using Euler's steepest descent method. Bar legend on the right gives the energy of the contour plot in E_h.

As described previously, there were two internal degrees of freedom that were treated explicitly in the RD PES[112] where one of them corresponded to the motion along the reaction coordinate, i.e. the MEP. Since the points along the MEP were non-stationary except at the TS, reactants and products, projection methods[120,121] as described previously in Sec. 2.2.2 were required to obtain the post-projection mass-weighted Hessian matrix for the calculation of the vibrational frequency of the mode that was orthogonal to the motion along the reaction coordinate at these points. In the calculations, it was found that at $s < -2.60$ bohr amu$^{1/2}$ and $s > 2.73$ bohr amu$^{1/2}$ the vibrational frequency became physically not meaningful where there were dips in the ZPEs in both the reactant and product valleys which reflected the changes in the vibrational frequencies. The properties of the reacting system at these points are presented in Table 4.2.

Table 4.2: Properties of reacting system at $s = -2.60$ bohr amu$^{1/2}$ and $s = 2.73$ bohr amu$^{1/2}$ for $CH_4 + H$.

s/bohr amu$^{1/2}$	$\{\rho$/bohr, δ/rad$\}$	Frequency/cm^{-1}
-2.60	{5.95, 0.506}	3568
2.73	{6.57, 0.132}	4918

Beyond the range where the vibrational frequencies were physically meaningful, i.e. $s < -2.60$ bohr amu$^{1/2}$ and $s > 2.73$ bohr amu$^{1/2}$, the vibrational frequencies were assumed to remain constant. The resulting potential energy, adiabatic ground state potential energy and ZPE curves along the MEP are illustrated in Fig 2.1.

4.1.1.2 Reaction Rate Constants

With the ZPE and adiabatic ground state potential energy curves shown in Fig 2.1, the TST/ZCT and TST/SCT reaction rate constants were calculated using the RD-adapted method described in Sec. 2.2.3 and Sec. 2.3. The reaction rate constants were compared with TST and QRS reaction rate constants as shown in Table 4.3 and Fig 4.2.

Table 4.3: Reaction rate constants for $CH_4 + H$ in cm^3 $molecule^{-1}$ s^{-1}. Number in parentheses denote the powers of 10. Results for TST/ZCT and TST/SCT were calculated without MI.

Temperature/K	TST	TST/ZCT	TST/SCT	QRS[112]
200	8.43(-26)	8.87(-23)	1.41(-21)	5.67(-22)
250	8.12(-23)	7.15(-21)	4.83(-20)	1.53(-20)
300	8.05(-21)	2.12(-19)	7.97(-19)	2.33(-19)
350	2.19(-19)	2.93(-18)	7.59(-18)	2.25(-18)
400	2.66(-18)	2.31(-17)	4.73(-17)	1.50(-17)
450	1.89(-17)	1.22(-16)	2.14(-16)	7.34(-17)
500	9.24(-17)	4.82(-16)	7.53(-16)	2.80(-16)
600	1.04(-15)	4.05(-15)	5.50(-15)	2.34(-15)
700	6.11(-15)	1.98(-14)	2.48(-14)	1.16(-14)
800	2.39(-14)	6.82(-14)	8.07(-14)	4.07(-14)
1000	1.73(-13)	4.19(-13)	4.67(-13)	2.57(-13)
1300	1.20(-13)	2.53(-12)	2.70(-12)	1.57(-12)
1600	4.39(-12)	8.47(-12)	8.84(-12)	5.24(-12)
2000	1.46(-11)	2.59(-11)	2.66(-11)	1.57(-11)

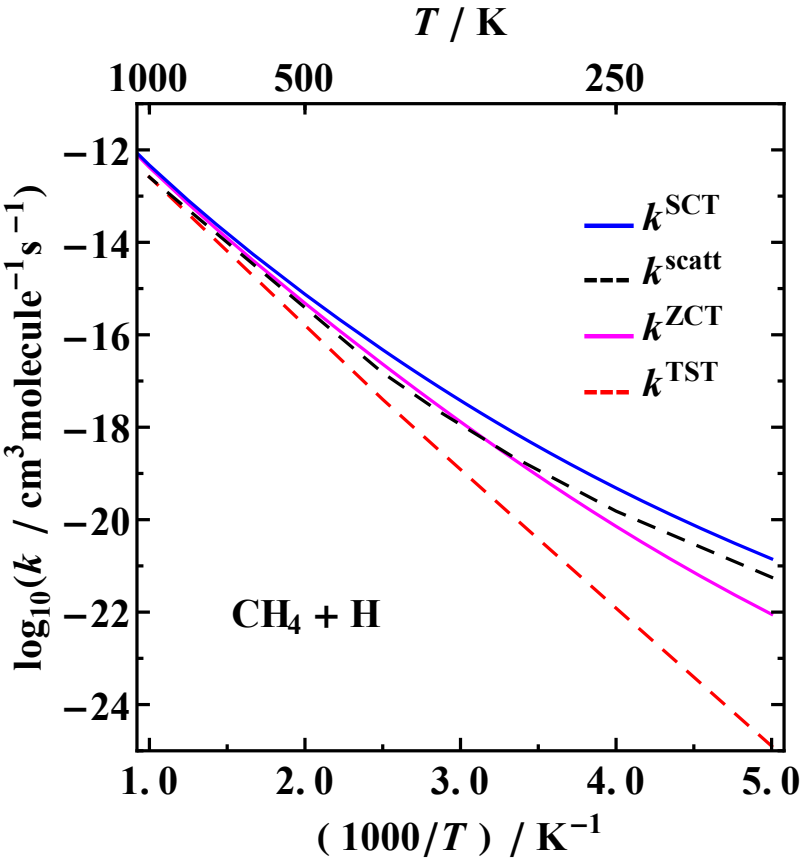


Figure 4.2: Plots of the reaction rate constants in logarithmic scale against 1000/T (where T is the temperature) for R1. TST/SCT, QRS,[112] TST/ZCT and TST reaction rate constants are represented by blue, black, pink and red curves respectively.

From Fig 4.2, the curves for TST and QRS converge at high temperatures which is expected since quantum effects become less important in reaction rate constant calculations at high temperatures. However, both TST/ZCT and TST/SCT are larger than TST results at higher temperatures. In particular, both TST/ZCT and TST/SCT reaction rate constants are about 2 times larger than the TST reaction rate constant at 2000K. The adiabatic barrier heights calculated without using MI and from *ab initio*[112] calculations were 13.102 kcal mol^{-1} and 13.785 kcal mol^{-1} respectively. Since quantum effects are not significant at such high temperatures, the overestimation of the reaction rate constants at 2000K may be due to the difference between the adiabatic barrier heights calculated without MI and *ab initio* calculations, therefore resulting in different TST reaction rate constants between TST and TST/SCT. When the temperature decreases, the curves start to diverge. This

is also expected since quantum effects become more significant at lower temperatures. Comparing TST/ZCT, TST/SCT and QRS results with TST ones, these methods produced reaction rate constants that were much larger than TST at low temperatures. This suggests that quantum effects such as quantum tunnelling are extremely important in R1, and TST itself is insufficient to produce accurate reaction rate constants. This is expected since a hydrogen is transferred in the reaction and quantum effects are known to be significant when a hydrogen is directly involved in the reaction.[22] When the TST/ZCT results were compared with QRS results, TST/ZCT reaction rate constants are smaller than QRS ones. This is expected since TST/ZCT is known to underestimate reaction rate constants due to the lack of accounting for reaction path curvature.[68,86] In particular, the QRS reaction rate constant was about 2 times that of TST/ZCT at 250K. When comparing TST/SCT with QRS, TST/SCT reaction rate constants overestimated with respect to those obtained from QRS calculations at low temperatures. In particular, at 250K, TST/SCT reaction rate constant was about 3 times larger than that of QRS. Due to the unexpected overestimation of TST/SCT results with respect to QRS ones at low temperatures, the cumulative reaction probability for TST/SCT was studied to gain insight into such behaviour.

4.1.1.3 Cumulative Reaction Probability

In order to study the factors contributing to the overestimation of the reaction rate constants by TST/SCT with respect to QRS calculations, the cumulative reaction probability (CRP) curves for TST/SCT and QRS calculations are given in Fig 4.3. In the CRPs for both QRS and TST/SCT in Fig 4.3, the threshold energies (E_0 in Eqn 2.32) for both calculations were 0 eV, i.e. the threshold energies for quantum tunnelling were both the energies of the reactants.

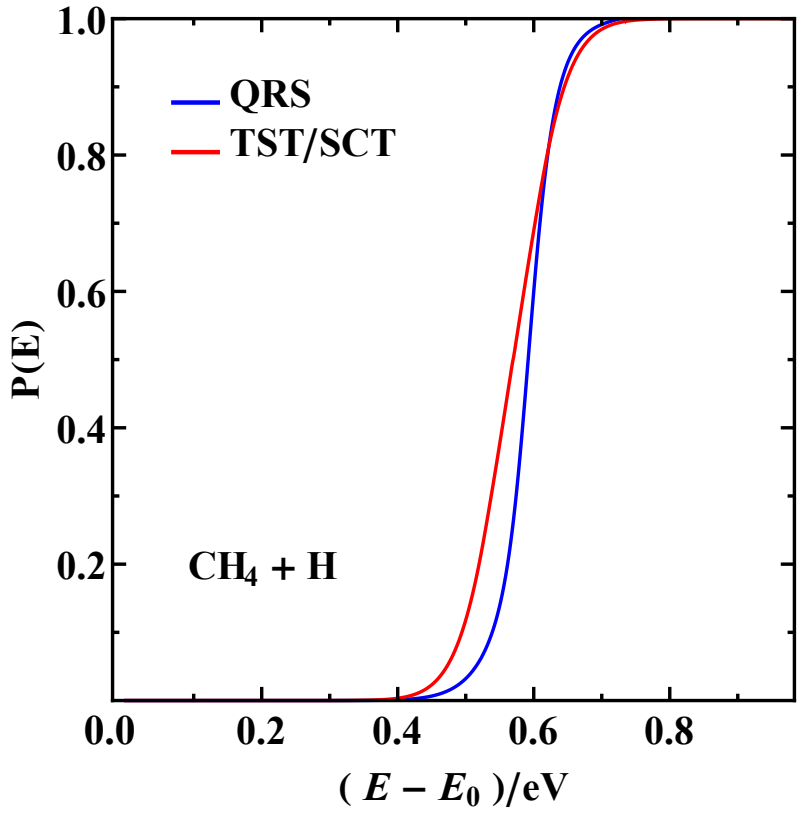


Figure 4.3: CRP curve for R1. Blue curve is the CRP from QRS calculations and red curve is from the TST/SCT calculations.

From Fig 4.3, the CRP for TST/SCT is larger than the CRP for QRS between 0.4 eV–0.6 eV. It was suggested that at 250K, the integral for the transmission coefficient was dominated by the CRP at $(E - E_0) < 0.6$ eV.[145] From Fig 4.3, at energies less than 0.6 eV, the CRP of TST/SCT is much larger than of QRS. This is further accentuated in the Boltzmann-weighted CRP at 250K which is shown in Fig 4.4.

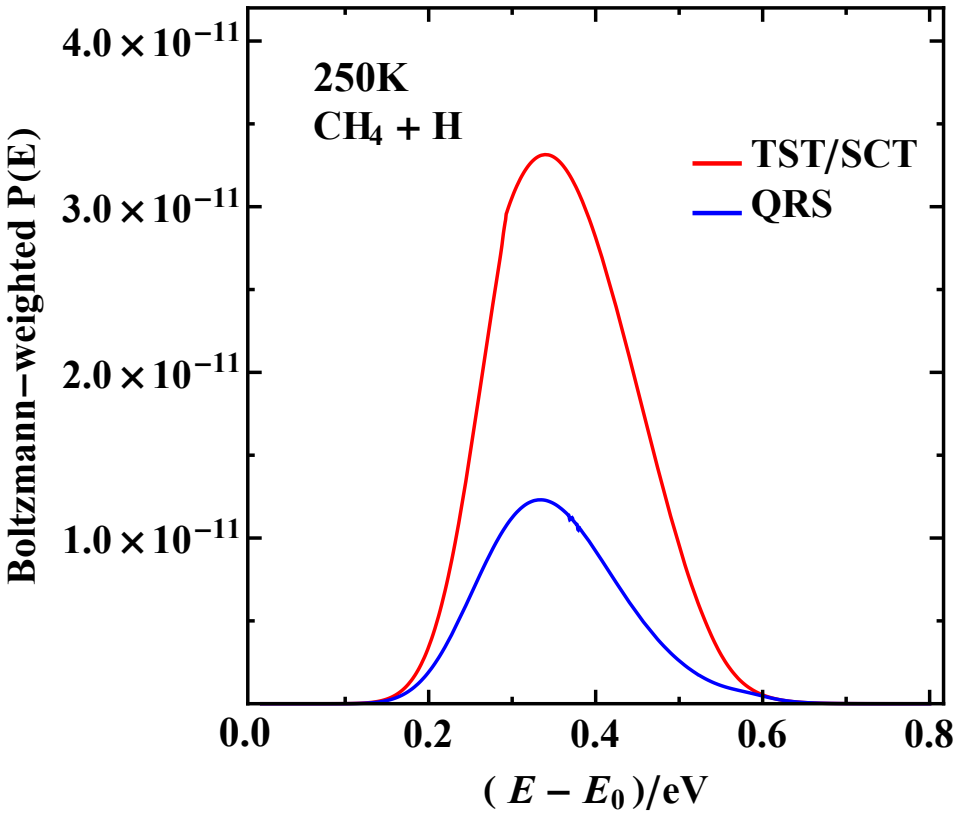


Figure 4.4: Boltzmann-weighted CRP curve for R1 at 250K. Blue curve is the CRP from QRS calculations and red curve is from the TST/SCT calculations.

From Fig 4.4, the area under the Boltzmann-weighted CRP curve for TST/SCT is much larger than that for QRS at 250K. This suggests that the TST/SCT transmission coefficient calculated by Eq 2.11 will be much larger than the QRS transmission coefficient at 250K. This led to an overestimation of TST/SCT reaction rate constants compared to QRS at low temperatures as shown in Table 4.3 and Fig 4.2. In the hope to improve the results presented in this section, MI was implemented in calculations.

4.1.2 With Mapped Interpolation

4.1.2.1 Minimum Energy Path

In the MI method, the reactants and products were used to interpolate data for points along the MEP where information was unavailable. This enabled the RD PES to be sampled from the TS to its maximum validity, i.e. $\rho = 30$ bohr.[112] They were defined to be the minimum points at $\rho = 30$ bohr, and their properties are given in Table 4.4.

Table 4.4: Properties of reactants and products at $\rho = 30$ bohr for $CH_4 + H$.

Direction	$\{\rho$/bohr, δ/rad$\}$	Frequency/cm^{-1}
Reactant	{30, 0.772}	3278
Product	{30, 0.037}	4573

From Table 4.4, the vibrational frequency of the reactants and products are lower than those in Table 4.2. Since both the vibrational frequencies and potential energies are interpolated using the reactants and products in MI, the resulting potential energy and adiabatic ground state potential energy curves along the MEP were altered when MI was implemented in the calculations. The curves are shown in Fig 4.5.

From Fig 4.5, the threshold energy for the evaluation of the transmission probability remains the same as the energy of the reactants when MI is used. However, the adiabatic ground state potential energy of the reactants when MI was used was lower than that without MI. This is due to the lower vibrational frequency calculated for the reactant using MI as shown in Table 4.4. Therefore, in the evaluation of the barrier penetration integral using Eq 2.31, the barrier penetration integral at an energy E with respect to the energy of the reactants on V_a^G (MI) in Fig 4.5 would be larger than the corresponding E with respect to the energy of the reactants on V_a^G in the same figure due to the wider adiabatic ground state potential energy curve at E. Therefore, the transmission probabilities at corresponding energies with respect to the energies of the reactants would be smaller when MI was used. In particular, this is true at low energies. This can be shown by comparing the CRP and

Boltzmann-weighted CRP at 250K between TST/SCT and QRS.

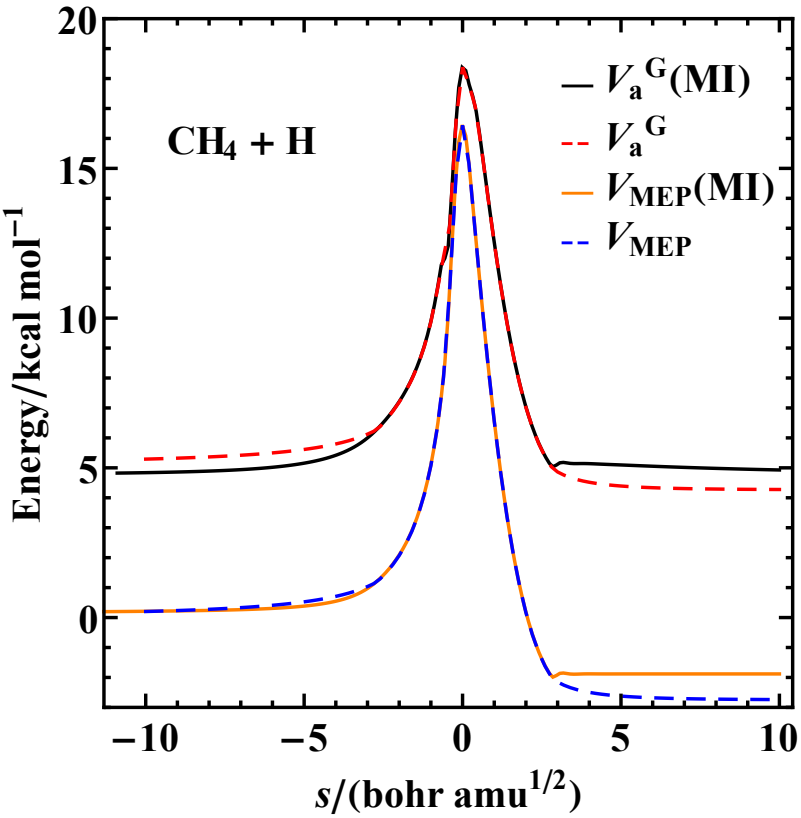


Figure 4.5: Adiabatic ground state potential energy and potential energy curves along the MEP with MI (black and orange curves respectively) and without MI (red and blue curves respectively) for R1.

4.1.2.2 Cumulative Reaction Probability

The new CRP curve for TST/SCT (MI) is shown in Fig 4.6 with the same QRS CRP curve from Fig 4.3. In Fig 4.6, the CRP for the TST/SCT (MI) is much lower than that in Fig 4.3 at energies less than 0.6 eV.[145] The CRP for TST/SCT (MI) is also closer to that obtained from QRS calculations than the CRP for TST/SCT (non-MI).

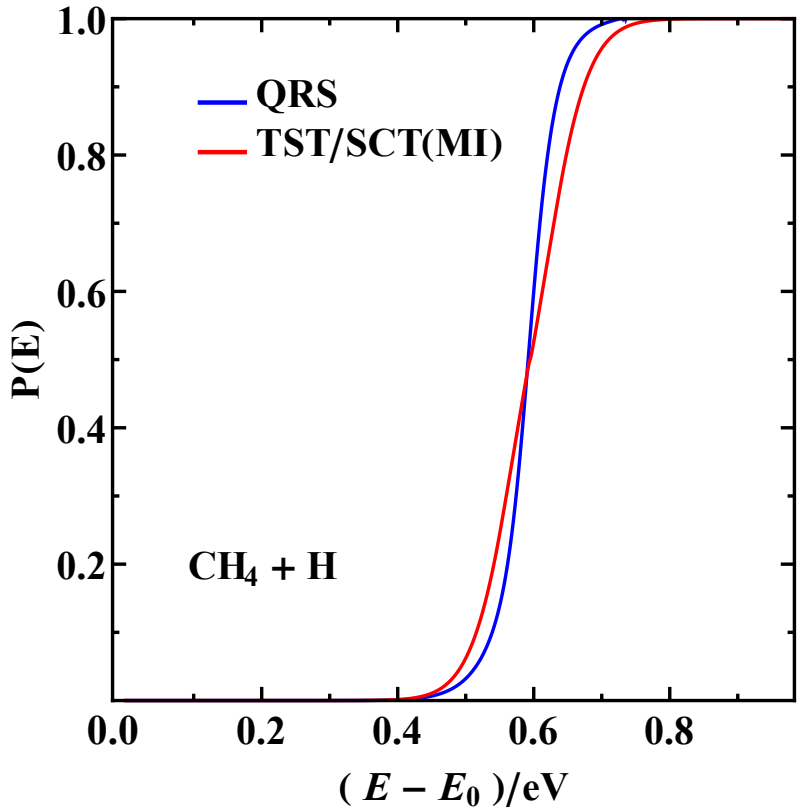


Figure 4.6: CRP curve for R1 using the MI method. Blue curve is the CRP from QRS calculations and red curve is from the TST/SCT (MI) calculations.

Since the transmission probability at lower energies have a larger contribution to the integral in Eq 2.11, a smaller CRP at low energies due to the new adiabatic ground state potential energy curve obtained would reduce the transmission coefficient at lower temperatures. This is shown in Fig 4.7 where the Boltzmann-weighted CRP curves for TST/SCT (MI) and QRS at 250K are given. From Fig 4.7, the Boltzmann-weighted CRP curve for TST/SCT (MI) is slightly shifted to higher energies as compared to the curve for QRS. However, the area under the Boltzmann-weighted CRP for TST/SCT (MI) is comparable to that to QRS calculations. Since the transmission coefficient calculated is dependent on the area under the Boltzmann-weighted CRP curve, the shifting of the curve to higher energies would not have an effect on the transmission coefficient. Comparison between Fig 4.7 and Fig 4.4 shows that the area under the Boltzmann-weighted CRP is greatly reduced by using the MI method. This implied that the TST/SCT (MI) transmission coefficient at

low temperatures, in particular, at 250K would be smaller than that when MI was not used.

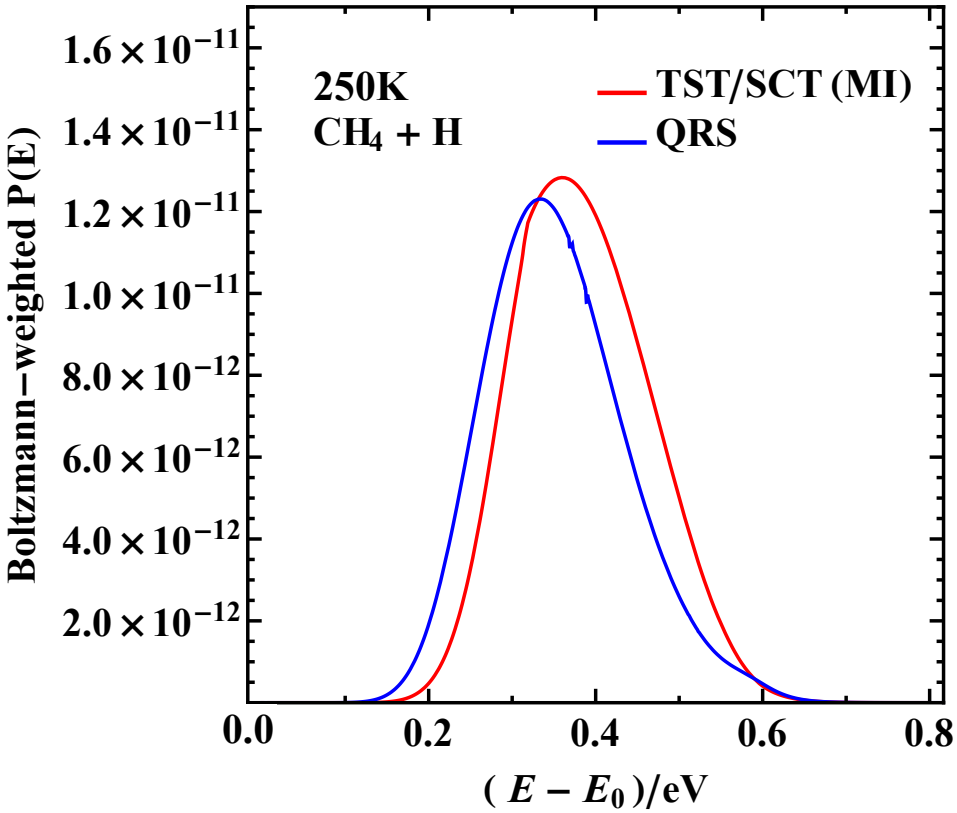


Figure 4.7: Boltzmann-weighted CRP curve for R1 at 250K using the MI method. Blue curve is the CRP from QRS calculations and red curve is from the TST/SCT (MI) calculations.

4.1.2.3 Reaction Rate Constants

The reaction rate constants calculated for TST, TST/ZCT (MI), TST/SCT (MI), QRS[112] and experimental data[136] are given in Table 4.5 and Fig 4.8.

Table 4.5: Reaction rate constants for $CH_4 + H$ in cm^3 $molecule^{-1}$ s^{-1}. Number in parentheses denote the powers of 10. Results for TST/ZCT and TST/SCT were calculated using the MI method.

Temperature/K	TST	TST/ZCT	TST/SCT	QRS[112]	Experiment[136]
200	8.43(-26)	2.08(-23)	4.18(-22)	5.67(-22)	
250	8.12(-23)	2.24(-21)	1.84(-20)	1.53(-20)	
300	8.05(-21)	8.08(-20)	3.57(-19)	2.33(-19)	
350	2.19(-19)	1.28(-18)	3.79(-18)	2.25(-18)	2.47(-18)
400	2.66(-18)	1.12(-17)	2.56(-17)	1.50(-17)	1.82(-17)
450	1.89(-17)	6.42(-17)	1.23(-16)	7.34(-17)	8.96(-17)
500	9.24(-17)	2.70(-16)	4.55(-16)	2.80(-16)	3.33(-16)
600	1.04(-15)	2.50(-15)	3.59(-15)	2.34(-15)	2.57(-15)
700	6.11(-15)	1.31(-14)	1.71(-14)	1.16(-14)	1.19(-14)
800	2.39(-14)	4.75(-14)	5.82(-14)	4.07(-14)	3.99(-14)
1000	1.73(-13)	3.14(-13)	3.57(-13)	2.57(-13)	2.43(-13)
1300	1.20(-13)	2.03(-12)	2.19(-12)	1.57(-12)	1.54(-12)
1600	4.39(-12)	7.09(-12)	7.46(-12)	5.24(-12)	5.59(-12)
2000	1.46(-11)	2.25(-11)	2.33(-11)	1.57(-11)	

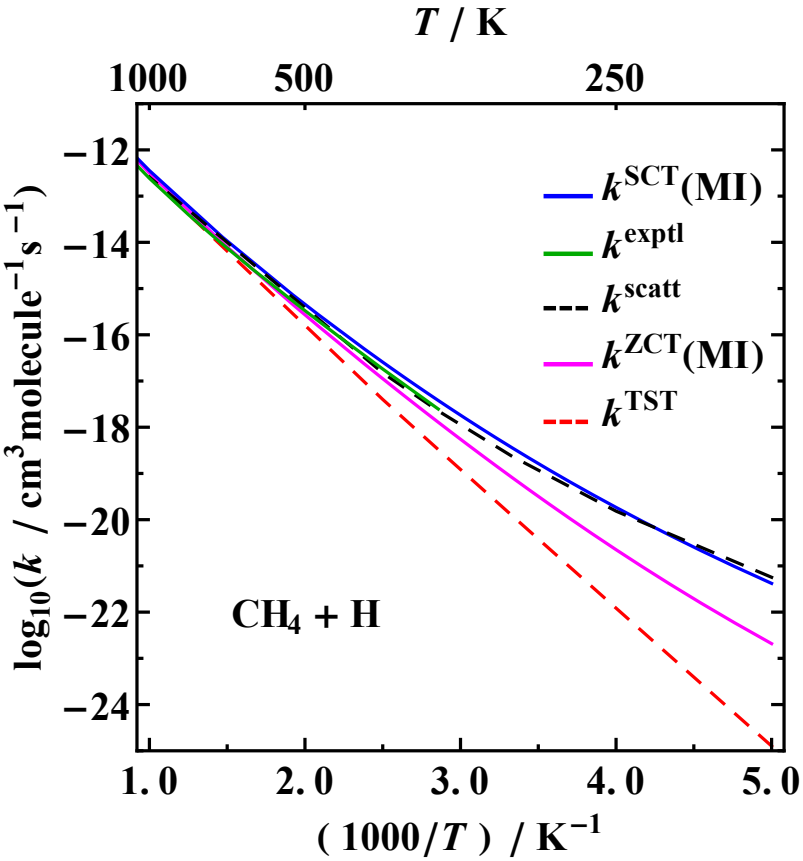


Figure 4.8: Plots of the reaction rate constants in logarithmic scale against 1000/T (where T is the temperature) for R1 using the MI method. Results obtained from TST/SCT (MI), experimental data,[136] QRS,[112] TST/ZCT (MI) and TST results are in blue, green, black, pink and red respectively.

From Fig 4.8, the reaction rate constants obtained experimentally and calculated by the theoretical methods converge at high temperatures, i.e. > 1000K, as expected. Comparing Table 4.3 and Table 4.5, the reaction rate constants of TST/ZCT and TST/SCT without MI at 2000K are reduced using MI. However, the TST/ZCT (MI) and TST/SCT (MI) reaction rate constants with MI are still slightly larger than TST ones at higher temperatures and this could be due to the difference in the adiabatic barrier height of the RD PES and *ab initio*[112] calculations which were calculated to be 13.676 kcal mol^{-1} and 13.785 kcal mol^{-1} respectively. Similar to Fig 4.2, the curves in Fig 4.8 diverge at low temperatures. This is especially so between the TST and the other theoretical methods. In particular, TST/ZCT (MI), TST/SCT (MI) and QRS calculations gave reaction rate constants that were 26, 227 and 188 larger than TST ones at 250K. This shows the inadequacy of TST when predicting

the reaction rate constants at low temperatures. When comparing with experimental data within the valid temperature range (348K–1950K),[136] both TST/ZCT (MI) and TST/SCT (MI) had good agreement within the temperature range 350K–1600K. At 350K, TST/ZCT (MI) underestimated the experimental reaction rate constant by 48% and TST/SCT (MI) overestimated the reaction rate constant by 53%. When comparing with QRS results, the reaction rate constants for TST/SCT (MI) were also in good agreement with QRS ones within the temperature range of 200K–2000K. In particular, at 250K, the TST/SCT (MI) results was 20% larger than QRS results which was considered good at such low temperatures.[86] On the other hand, the TST/ZCT (MI) reaction rate constant was 85% smaller than QRS ones at the same temperature. This was attributed to the lack of accounting for the reaction path curvature. Across the entire temperature range of 200K–2000K, TST/ZCT (MI) reaction rate constants were consistently lower than TST/SCT (MI) ones. This showed that it was important to consider reaction path curvature in the calculation of transmission coefficients.

Comparing Fig 4.8 with Fig 4.2 and Table 4.5 with Table 4.3, using MI in the calculations lowered the reaction rate constants for both TST/ZCT and TST/SCT which led to a better agreement between TST/SCT (MI) and QRS especially at lower temperatures. This was due to the smaller vibrational frequencies evaluated for the reactants when MI was used. This resulted in larger barrier penetration integrals at lower energies. As a result, the areas under the Boltzmann-weighted CRP curves were smaller when MI was used especially at low temperatures which led to the smaller transmission coefficients calculated for TST/SCT (MI).

4.1.3 Summary for $CH_4 + H \longrightarrow CH_3 + H_2$

In the test of the TST/ZCT and TST/SCT methods on the RD PES for reaction R1, the use of MI improved the results by using more information from the RD PES, in particular,

the reactants and products were defined to be the minimum points on the RD PES at its maximum validity, i.e. $\rho = 30$ bohr. Using the information at $\rho = 30$ bohr did not change the threshold energy in which the transmission coefficient was evaluated for the reaction; it altered the shape of the adiabatic ground state potential energy due to the lower frequency of the reactants. This led to excellent agreement between TST/SCT (MI) and QRS results. TST/ZCT (MI) results underestimated TST/SCT (MI) results across all temperatures due to the lack of reaction path curvature considered in the calculations, hence also underestimating the QRS reaction rate constants. This showed the importance of reaction path curvature in transmission coefficient calculations. Comparison between TST and other theoretical methods presented showed the importance of quantum effects in the reaction where a light hydrogen atom was transferred especially at low temperatures. The results for this simplest reaction involving a hydrocarbon served as a good platform to test the TST/MT methods on more complicated systems such as R2 and R3. Therefore, similar approaches were used in the calculation of the reaction rate constants for reactions R2 and R3. The results for these reactions will be presented in subsequent sections.

4.2 $C_2H_6 + H \longrightarrow C_2H_5 + H_2$

In the previous section, TST/ZCT and TST/SCT were applied to the RD PES[112] for R1. With the excellent agreement that TST/SCT (MI) had with QRS calculations on the same RD PES for R1, an extension of the test of TST/ZCT and TST/SCT was applied to reactions that were more complicated. One of such reactions was to extend the carbon chain by 1, which gave reaction R2. Similar to R1, R2 is also important in combustion processes.[109,146] In the calculations for R2, the RD PES reported by Kerkeni *et al.*[109] was used where the spectator modes were treated in rectilinear coordinates. Calculations were both carried out without and with MI to study the improvements to the results when MI was applied. The results for calculations without applying the MI method will first be presented.

4.2.1 Without Mapped Interpolation

4.2.1.1 Minimum Energy Path

The MEP for R2 was calculated on the RD PES reported by Kerkeni *et al.*[109] from the TS towards the reactants and products. The properties of the TS on the RD PES are given in Table 4.6.

Table 4.6: Properties of the TS on the RD PES[109] for $C_2H_6 + H$.

$\{\rho$/bohr, δ/rad$\}$	$V(\rho,\delta)$/E_h	Frequency/cm^{-1}
{3.55, 0.253}	-0.0381	1394

Comparing Table 4.1 and Table 4.6, the real vibrational frequency of the TS for R2 is similar to that for R1. This was expected since the hydrocarbons in both reactions were similar, hence resulting in similar TS structures for both reactions. In each direction of the MEP calculation, 1000 steps were taken with stepsize 0.01 bohr $amu^{1/2}$. The resulting MEP is shown in Fig 4.9 on the contour plot of the RD PES in the range of validity, 3 bohr $< \rho <$ 26 bohr.[109] On the contour plot in Fig 4.9, the reactant valley of the RD PES corresponds to points along the MEP where the $\delta > 0.253$ rad, and the opposite applies to the product valley. Similar to Fig 4.1 for R1 presented in the previous section, the MEP for R2 did not fully sample the maximum validity of the RD PES in both the reactant and product asymptotic regions.

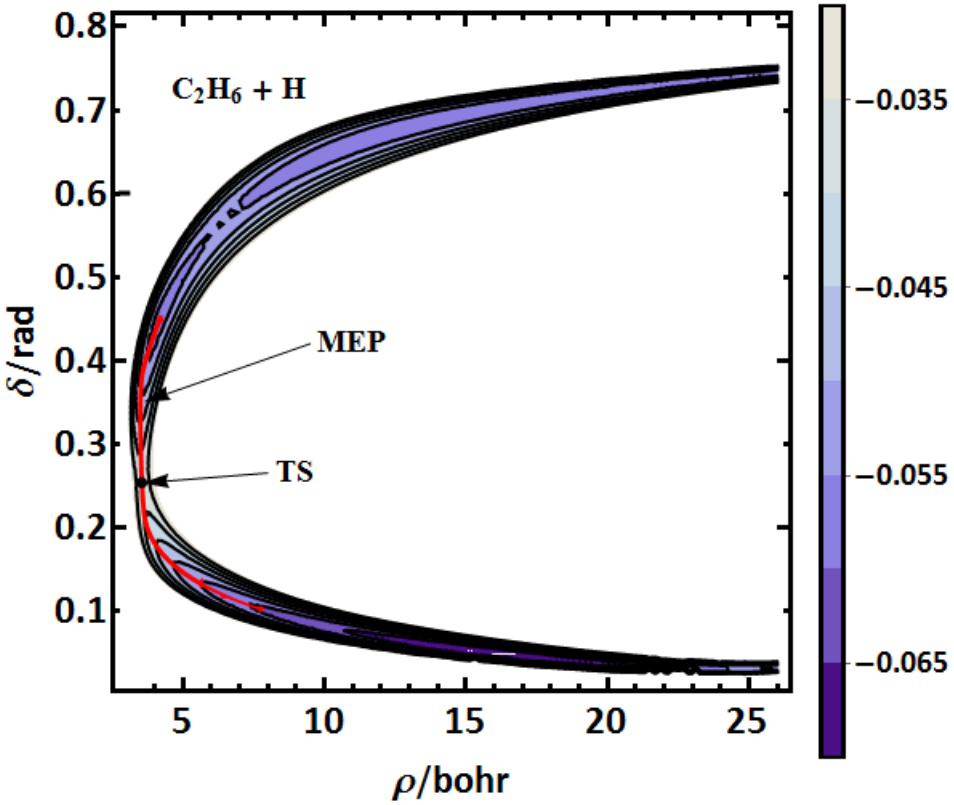


Figure 4.9: The contour plot of the RD PES of R2 by Kerkeni *et al.*[109] with the spectator modes treated in rectilinear coordinates. Black dot is the TS on the RD PES and red curve is the MEP calculated from the TS using Euler's steepest descent method. Bar legend on the right gives the energy of the contour plot in E_h.

For R2, the range of reaction coordinates where the vibrational frequencies calculated were physically meaningful was -1.40 bohr amu$^{1/2} \leq s \leq$ 2.80 bohr amu$^{1/2}$. The properties of the reacting system at these reaction coordinates are given in Table 4.7.

Table 4.7: Properties of reacting system at $s = -1.40$ bohr amu$^{1/2}$ and $s = 2.80$ bohr amu$^{1/2}$ for $C_2H_6 + H$.

s/bohr amu$^{1/2}$	$\{\rho$/bohr, δ/rad$\}$	Frequency/cm^{-1}
-1.40	{4.05, 0.437}	3240
2.80	{5.46, 0.136}	4720

Beyond the range where the vibrational frequencies were physically meaningful, i.e. $s < -1.40$ bohr amu$^{1/2}$ and $s > 2.80$ bohr amu$^{1/2}$, the vibrational frequencies were kept constant at 3240 cm^{-1} and 4720 cm^{-1} respectively. The resulting potential energy, adi-

abatic ground state potential energy and ZPE curves along the MEP are illustrated in Fig 4.10.

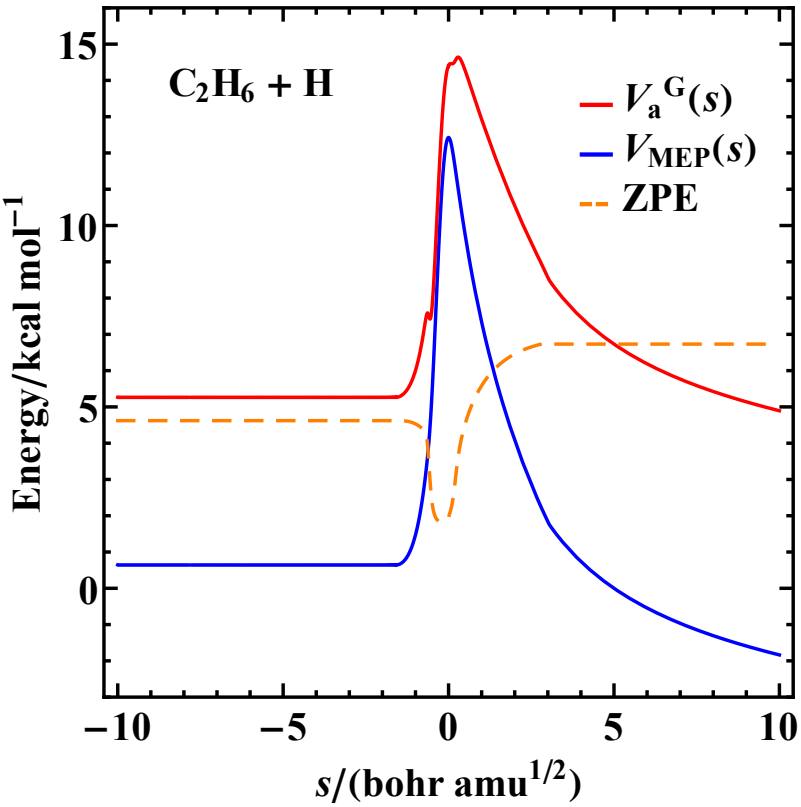


Figure 4.10: Illustration of the adiabatic ground state potential energy (red), MEP potential energy (blue) and ZPE (orange) along the MEP for R2.

From Fig 4.10, the adiabatic ground state potential energy of the reactants is larger than that of the products. Therefore, in the evaluation of the transmission coefficient, the threshold energy is 0 eV, i.e. the energy of the reactants. Comparison of the ZPE curves in Fig 2.1 and Fig 4.10 shows similar trends where the ZPE drops when approaching from both asymptotic regions, and the ZPE at the products is larger than that of the reactants. This is expected due to the similarities of both reactions.

4.2.2 Reaction Rate Constants

Using the adiabatic ground state potential energy curve in Fig 4.10, TST/ZCT and TST/SCT were calculated in a similar way as R1 and the resulting reaction rate constants are shown in Table 4.8.

Table 4.8: Reaction rate constants for $C_2H_6 + H$ in cm^3 $molecule^{-1}$ s^{-1}. Number in parentheses denote the powers of 10. Results for TST/ZCT and TST/SCT were calculated without using the MI method.

Temperature/K	TST	TST/ZCT	TST/SCT	QRS[109]
200	7.76(-24)	1.77(-20)	3.98(-20)	4.08(-21)
260	8.56(-21)	2.57(-18)	4.21(-18)	7.74(-19)
320	7.12(-19)	6.58(-17)	9.18(-17)	2.36(-17)
360	6.12(-18)	3.28(-16)	4.27(-16)	1.27(-16)
420	7.36(-17)	2.14(-15)	2.60(-15)	9.08(-16)
480	4.88(-16)	9.08(-15)	1.06(-14)	4.11(-15)
520	1.37(-15)	2.01(-14)	2.29(-14)	9.43(-15)
680	2.74(-14)	2.08(-13)	2.24(-13)	1.06(-13)
880	2.80(-13)	1.32(-12)	1.38(-12)	7.12(-13)
1000	7.58(-13)	2.92(-12)	3.03(-12)	1.61(-12)
1300	4.45(-12)	1.23(-11)	1.25(-11)	6.92(-12)
2000	4.44(-11)	7.85(-11)	7.93(-11)	4.50(-11)

From Table 4.8, it is shown that both TST/ZCT and TST/SCT overestimate the reaction rate constants with respect to QRS calculations on the same RD PES[109] in the temperature range 200K–2000K. In particular, at 260K, the TST/ZCT reaction rate constant was 3 times larger than those obtained from QRS calculations. Since TST/ZCT is known to underestimate reaction rate constants due to the lack of consideration of the reaction path curvature in calculations,[68,86] such results is unexpected. Therefore, TST/SCT, which corrected for the reaction path curvature from TST/ZCT results,[68] led to an even larger overestimation of reaction rate constants with respect to QRS results. At 260K, the TST/SCT reaction rate constant was 5 times larger than that obtained from QRS calculations. This can be further

illustrated by Fig 4.11.

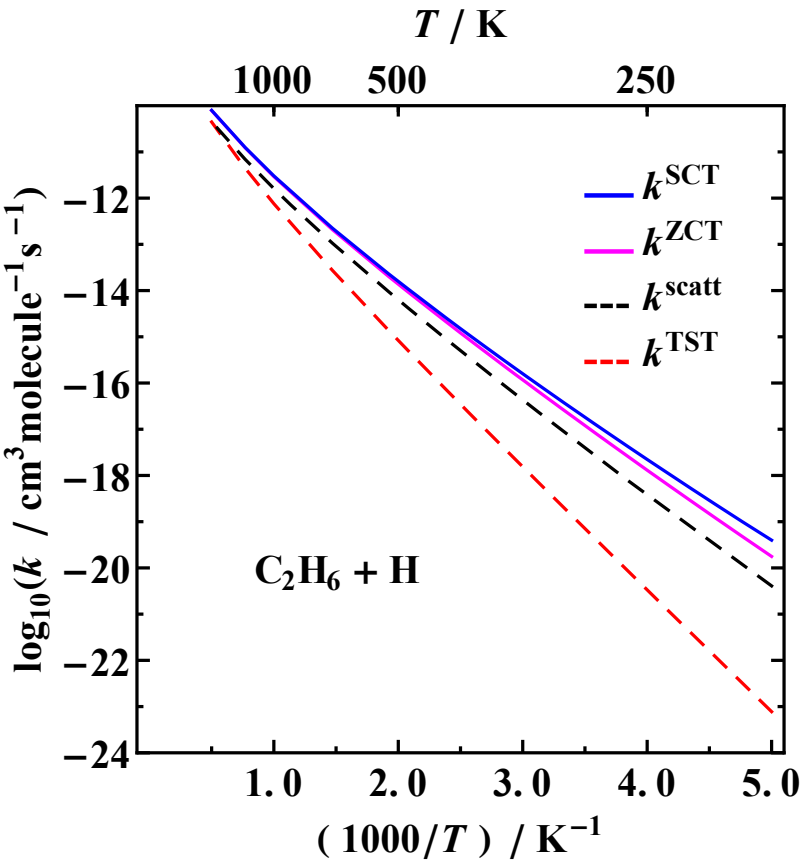


Figure 4.11: Plots of the reaction rate constants in logarithmic scale against 1000/T (where T is the temperature) for R2. TST/SCT, TST/ZCT, QRS,[109] and TST reaction rate constants are represented by blue, pink, black and red curves respectively.

From Fig 4.11, TST/SCT, TST/ZCT and QRS reaction rate constants are significantly larger than TST ones. In particular, at 260K, they are 492, 300 and 90 times larger respectively. This once again shows that quantum effects are important in hydrogen abstraction reaction such as R2. This is expected since a hydrogen atom is transferred between an ethane molecule and a hydrogen atom. This also agreed with results for R1 where quantum effects are important since both reactions are similar. Since the overestimation of reaction rate constants were also encountered in the calculations for R1, the CRP and Boltzmann-weighted CRP were plotted for R2 to gain insight into the overestimation of reaction rate constants for the reaction.

4.2.3 Cumulative Reaction Probability

In the CRP for reaction R2, the threshold energy for the CRP in the QRS calculations was not the energy of the reactants but the energy of the products in R2, i.e. $E_0 > 0$ eV. Therefore, in the TST/SCT calculations without MI, the transmission probability was higher than QRS especially at low energies. Since the transmission coefficients at low temperatures are extremely sensitive to the transmission probabilities at low energies, slight inaccuracies in the transmission probabilities could result in a large difference in the transmission coefficients. This is shown by the difference in areas under the Boltzmann-weighted CRP for both TST/SCT and QRS at 260K in Fig 4.12.

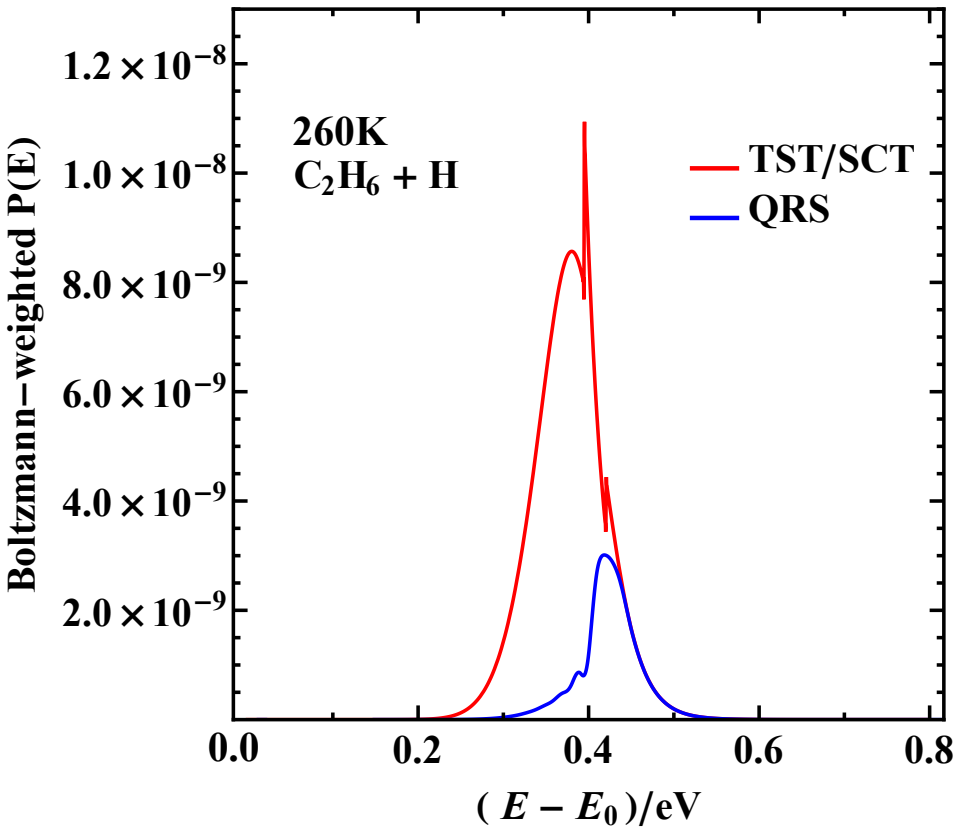


Figure 4.12: Boltzmann-weighted CRP curve for R2 at 260K. Blue curve is the CRP from QRS calculations and red curve is from the TST/SCT calculations.

From Fig 4.12, the area under the Boltzmann-weighted CRP curve of TST/SCT is much larger than that of QRS at 260K. Therefore, when evaluating the transmission coefficient

at 260K, this resulted in the overestimation of the reaction rate constants of TST/SCT as compared to QRS which is shown both in Table 4.8 and Fig 4.11. In order to correct for the threshold energy for CRP calculations, MI was used in the calculations for R2.

4.2.4 With Mapped Interpolation

4.2.4.1 Minimum Energy Path

Using the RD PES proposed by Kerkeni *et al.*,[109] the reactants and products on the RD PES were calculated at the maximum ρ validity, i.e. $\rho = 26$ bohr. Their properties are given in Table 4.9.

Table 4.9: Properties of reactants and products at $\rho = 26$ bohr for $C_2H_6 + H$.

Direction	$\{\rho$/bohr, δ/rad$\}$	Frequency/cm^{-1}
Reactant	{26, 0.745}	3109
Product	{26, 0.0315}	4416

Similar to R1, comparison between Table 4.7 and Table 4.9 shows that the vibrational frequencies calculated at $\rho = 26$ bohr are smaller. The resulting potential energy and adiabatic potential energy curves obtained due to the use of MI are plotted with those calculated without MI and are shown in Fig 4.13.

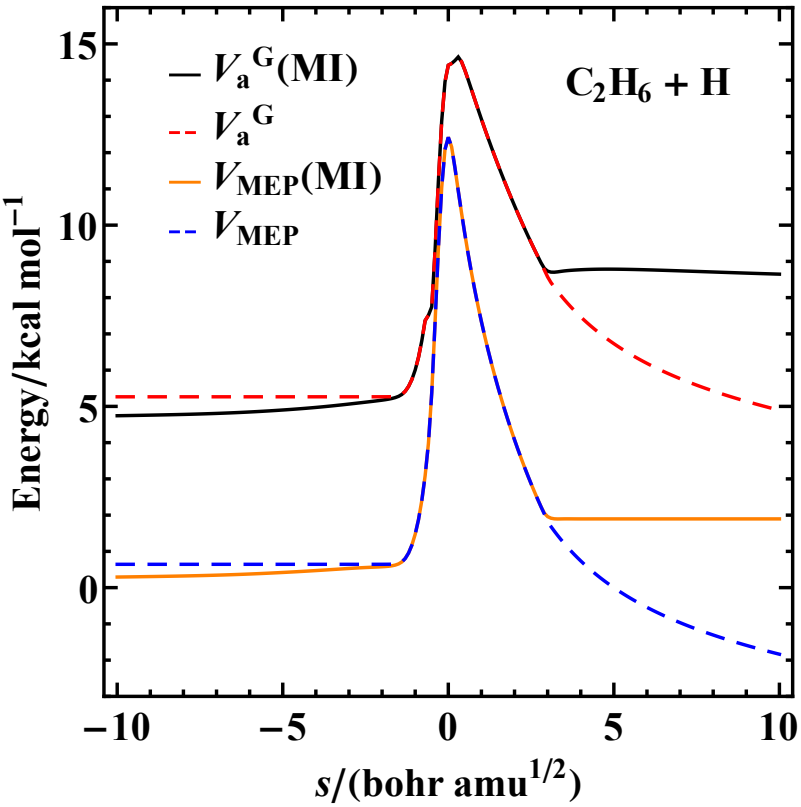


Figure 4.13: Adiabatic ground state potential energy and potential energy curves along the MEP with MI (black and orange curves respectively) and without MI (red and blue curves respectively) for R2.

From Fig 4.13, it is seen that the potential energy and the adiabatic ground state potential energy at the reactants ($s < 0$ bohr amu$^{1/2}$) when MI was used are in good agreement to the energies when MI was not used. However, this is not the case in the product asymptotic region ($s > 0$ bohr amu$^{1/2}$). The large difference in the adiabatic ground state potential energy was mostly due to the difference in the potential energy curve along the MEP rather than the vibrational frequencies calculated at the products.

In order to study the differences between the potential energies along the MEP calculated on the RD PES by Euler's steepest descent method and MI, the potential energy curves in Fig 4.13 were extended in the range 10 bohr amu$^{1/2}$ $< s < \infty$ to reach the products. However, the steepest descent method was unable to calculate the vibrational frequencies accurately beyond $s > 2.80$ bohr amu$^{1/2}$. Therefore, the potential energies on the RD PES

in the product asymptotic region were calculated by finding the potential energies of the stationary points in the product asymptotic region. These points were calculated along ρ = 5.46 bohr (from Table 4.7), 6 bohr, and subsequently in intervals of $\delta\rho$ = 1 bohr until the products at ρ = 26 bohr. The potential energy curves calculated on the RD PES at stationary points in intervals of $\delta\rho = 1$ bohr and by the MI method given in Fig 4.14 serve as an extension to Fig 4.13 for the range 2.80 bohr amu$^{1/2} < s < \infty$.

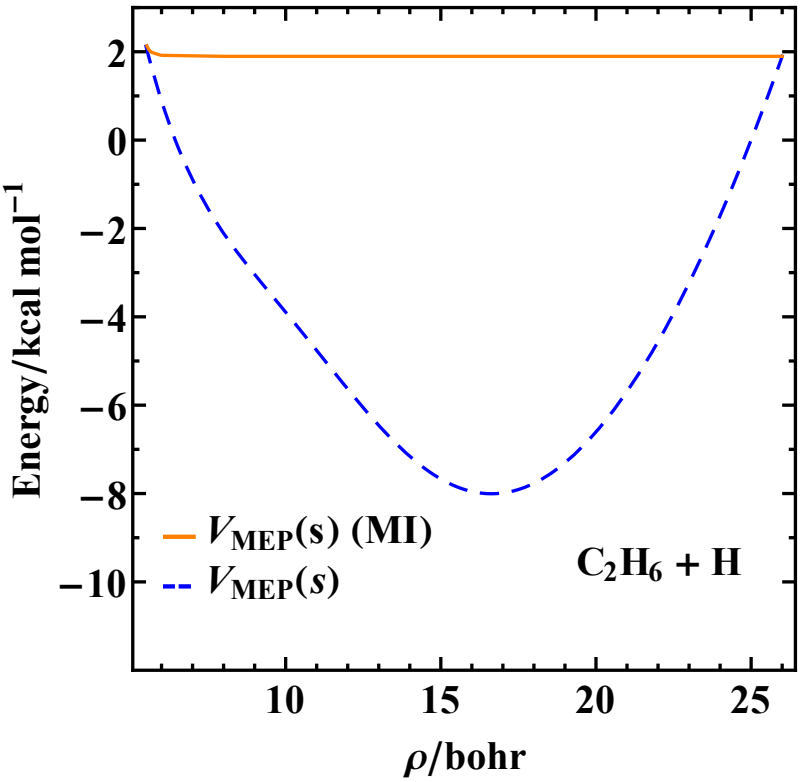


Figure 4.14: Potential energy curves calculated with and without MI (in orange and blue respectively) in the product asymptotic region for R2 in the range 5.46 bohr < ρ < 26 bohr.

From Fig 4.14, it is shown that between $\rho = 5.46$ bohr and $\rho = 26$ bohr, the potential energy on the RD PES is lower than that of $\rho = 26$ bohr. When MI was used, the mapping function in Eq 2.70 placed less emphasis on points that were closer to the asymptotic regions. In the case of the product region in R2, interpolation was carried out in the range 2.80 bohr amu$^{1/2} \leq s \leq \infty$ bohr amu$^{1/2}$. Using Eq 2.70, this corresponded to a range of 0.903 bohr amu$^{1/2} \leq z \leq 1$ bohr amu$^{1/2}$. Therefore, information about the potential energy

was lost in the range 5.46 bohr $\leq \rho \leq$ 26 bohr (from Table 4.7) when MI was used. However, this did not affect the evaluation of the transmission coefficients since the energies in the range 5.46 bohr $\leq \rho \leq$ 26 bohr were lower than the threshold energy (energy of the products at $\rho = 26$ bohr) and would not contribute to the evaluation of the transmission coefficients. Therefore, the resultant adiabatic ground state potential energy evaluated with MI was used to calculate the TST/ZCT (MI) and TST/SCT (MI) reaction rate constants.

4.2.5 Cumulative Reaction Probability

With the implementation of MI, the difference in the potential energy curve along the MEP resulted in a change in the threshold energy (previously given as E_0 in Eq 2.32) used in the evaluation of the transmission coefficients. The threshold energies for QRS,[109] TST/SCT (non-MI) and TST/SCT (MI) are given in Table 4.10 to show the effect of using MI for the reaction.

Table 4.10: Threshold energies, E_0 calculated by QRS,[109] TST/SCT (non-MI) and TST/SCT (MI).

	QRS[109]	TST/SCT (non-MI)	TST/SCT (MI)
E_0/eV	0.14	0	0.16

With the correction in the threshold energy, this altered the Boltzmann-weighted CRP at 260K which is given in Fig 4.15. The area under the Boltzmann-weighted CRP curve at 260K in Fig 4.15 is greatly reduced, and is much closer to that from QRS calculations. This also suggests that the TST/SCT (MI) transmission probability will be reduced from previous calculations without MI and the reaction rate constants will have better agreement with those obtained from QRS. The reaction rate constants calculated with MI is presented in the next section.

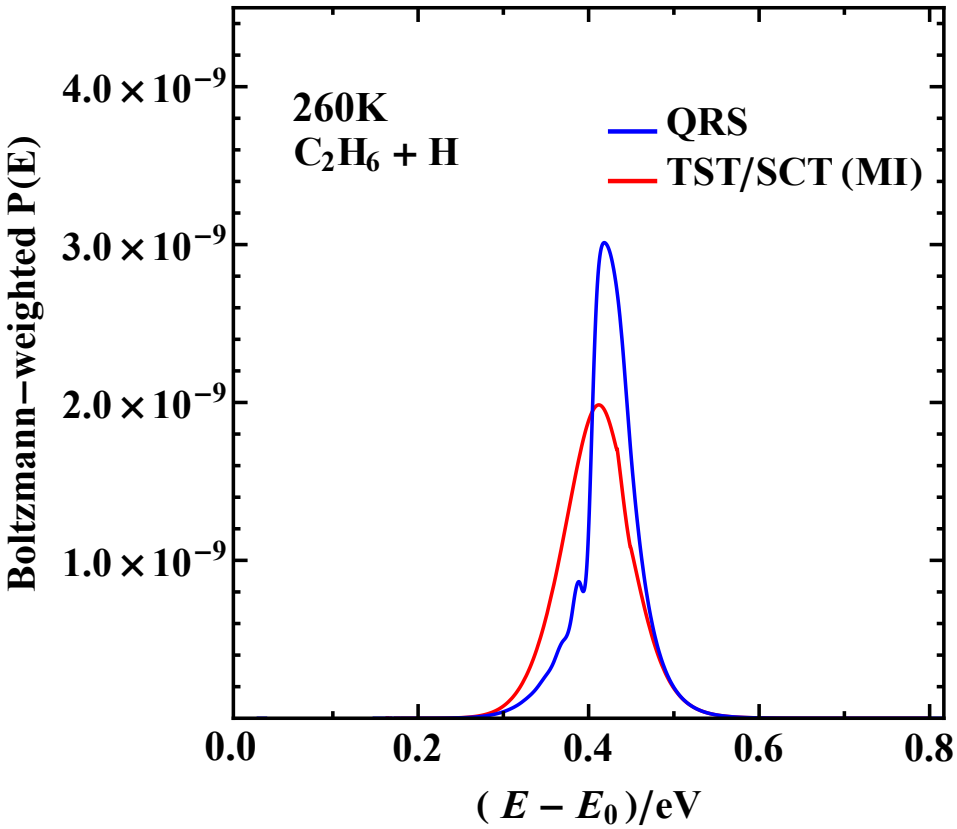


Figure 4.15: Boltzmann-weighted CRP curve for R2 at 260K using the MI method. Blue curve is the CRP from QRS calculations and red curve is from the TST/SCT (MI) calculations.

4.2.6 Reaction Rate Constants

The reaction rate constants calculated for TST, TST/ZCT (MI), TST/SCT (MI), QRS[109] and experimental data[146,147] are given in Table 4.11 and Fig 4.16.

Table 4.11: Reaction rate constants for $C_2H_6 + H$ in cm^3 $molecule^{-1}$ s^{-1}. Number in parentheses denote the powers of 10. Results for TST/ZCT and TST/SCT were calculated using the MI method.

Temperature/K	TST	TST/ZCT	TST/SCT	QRS[109]	Experiment[146,147]
200	7.76(-24)	1.38(-21)	3.28(-21)	4.08(-21)	
260	8.56(-21)	3.61(-19)	6.13(-19)	7.74(-19)	
320	7.12(-19)	1.34(-17)	1.91(-17)	2.36(-17)	
360	6.12(-18)	7.94(-17)	1.06(-16)	1.27(-16)	4.46(-16)[147]
420	7.36(-17)	6.35(-16)	7.84(-16)	9.08(-16)	2.81(-15)[147]
480	4.88(-16)	3.13(-15)	3.69(-15)	4.11(-15)	1.18(-14)[146]
520	1.37(-15)	7.53(-15)	8.66(-15)	9.43(-15)	2.36(-14)[146]
680	2.74(-14)	9.74(-14)	1.06(-13)	1.06(-13)	1.66(-13)[146]
880	2.80(-13)	7.22(-13)	7.60(-13)	7.12(-13)	
1000	7.58(-13)	1.72(-12)	1.77(-12)	1.61(-12)	
1300	4.45(-12)	7.79(-12)	7.99(-12)	6.92(-12)	
2000	4.44(-11)	5.38(-11)	5.44(-11)	4.50(-11)	

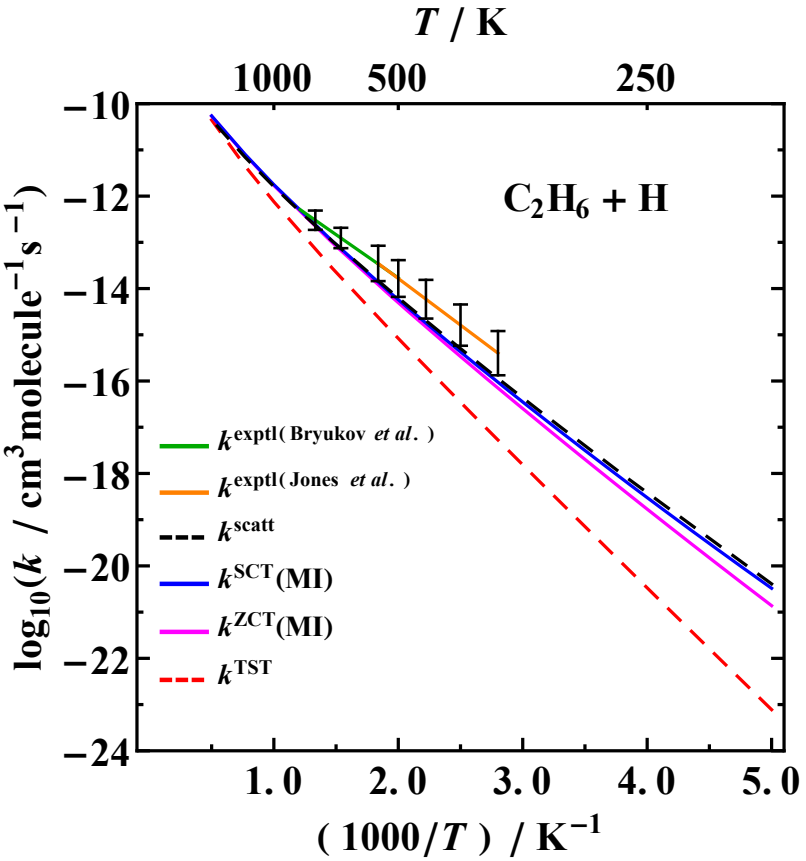


Figure 4.16: Plots of the reaction rate constants in logarithmic scale against 1000/T (where T is the temperature) for R2 using the MI method. Results obtained from experimental data by Bryukov *et al.*[146] and Jones *et al.*,[147] QRS,[109] TST/SCT (MI), TST/ZCT (MI) and TST are in green, orange, black, blue, pink and red respectively.

From Fig 4.16, QRS, TST/SCT (MI) and TST/ZCT (MI) reaction rate constants are much larger than TST at low temperatures. In particular, their reaction rate constants are 90, 77 and 42 times larger than TST ones at 260K. This shows the importance of quantum effects in R2 when a light hydrogen atom is transferred. This is similar to the results of R1. TST/ZCT (MI) and TST/SCT (MI) reaction rate constants are also in good agreement with QRS results over the entire temperature range. However, TST/SCT (MI) reaction rate constants are larger than TST/ZCT (MI) ones and have better agreement to QRS results, which is expected due to the importance of reaction path curvature in transmission coefficient calculations.[68] In particular, at 260K, TST/SCT (MI) accounts for almost double the amount of quantum tunnelling than in TST/ZCT (MI). Comparing with experimental results, TST/SCT (MI) results are slightly lower than the range of the experimental results.

However, the TST/SCT (MI) results were calculated using the same RD PES[109] as QRS calculations. Therefore, such agreement to experimental results are expected due to the agreement between QRS results and experimental results.[109] Comparison between Table 4.8 and Table 4.11, and between Fig 4.11 and Fig 4.16 shows the improvement in the results when MI was implemented. This is due to the correction for the threshold energy.

4.2.7 Summary for $C_2H_6 + H \longrightarrow C_2H_5 + H_2$

In the test of TST/ZCT and TST/SCT on the RD PES,[109] the reaction rate constants obtained from both methods have good agreement to both QRS calculations[109] and to experimental data when MI was used.[146,147] In particular, TST/SCT (MI) agrees excellently to QRS results even at low temperatures such as 260K. For both R1 and R2, MI improved the reaction rate constants with respect to QRS. Even though MI corrected for the vibrational frequencies in both reactions, such correction was not as significant in R2 as compared to R1. The significant correction that MI made in R2 was the threshold energy in the CRP calculations. By applying TST/ZCT and TST/SCT on the RD PES[109] for R2, an extension of the method used for R1 was tested on a similar system that is more complicated due to the increased length of the carbon chain. With the good agreement obtained for R1 and R2 involving a linear alkane and a hydrogen, the same method was further applied to R3 which involved a reaction between cyclic alkane with a hydrogen atom.

4.3 cyc-$C_3H_6 + H \longrightarrow$ cyc-$C_3H_5 + H_2$

R3 is the simplest hydrogen abstraction reaction involving a cyclic alkane. The cyclopropyl radical which is produced in the reaction is important in combustion processes,[148] and it undergoes subsequent ring opening to produce the more stable allyl radical[148] which is studied in experiments.[149,150] However, to our best knowledge, TST/MT methods have not been applied to this reaction before. In addition, in a previous study of R3 by Shan *et al.*,[113] the RD PES had been constructed. Therefore, TST/ZCT and TST/SCT were applied to the RD PES constructed by Shan *et al.*[113] to further extend the study of hydrogen abstraction reactions involving alkanes. Given the excellent agreement of the reaction rate constants obtained by TST/SCT (MI) to those calculated by QRS and experimental data, MI was directly applied in calculations for this reaction and will be presented next.

4.3.1 With Mapped Interpolation

4.3.1.1 Minimum Energy Path

Using the RD PES constructed by Shan *et al.*,[113] the MEP was calculated in the range -2.25 bohr amu$^{1/2} \leq s \leq$ 2.10 bohr amu$^{1/2}$ from the TS. The properties of the TS are given in Table 4.12.

Table 4.12: Properties of the TS on the RD PES[113] for cyc-$C_3H_6 + H$.

$\{\rho$/bohr, δ/rad$\}$	$V(\rho,\delta)$/E_h	Frequency/cm^{-1}
{3.49, 0.243}	-118.13	1548

Comparing Table 4.12 with Tables 4.1 and 4.6, the vibrational frequency of the TS for R3 is significantly larger than that of the TS for R1 and R2. This is due to the unusually strong C–H bond of a cyclopropane,[113,151,152] unlike in R1 and R2 which involved linear alkanes. When calculating the MEP from the TS with stepsize 0.01 bohr amu$^{1/2}$, the vibrational frequencies became physically not meaningful at the points $s = -2.25$ bohr amu$^{1/2}$

and $s = 2.10$ bohr amu$^{1/2}$ in the reactant and product asymptotic regions respectively. The properties of the reacting system at these points are given in Table 4.13.

Table 4.13: Properties of reacting system at boundaries for MI for cyc-$C_3H_6 + H$.

s/bohr amu$^{1/2}$	$\{\rho$/bohr, δ/rad$\}$	Frequency/cm^{-1}
-2.25	{4.47, 0.476}	3209
2.10	{4.88, 0.139}	5344

Therefore, MI was applied for calculations between these points and the reactants and products at the maximum validity of the RD PES, i.e. $\rho = 12$ bohr.[113] The properties of the reactants and products are given in Table 4.14.

Table 4.14: Properties of reactants and products at $\rho = 12$ bohr for cyc-$C_3H_6 + H$.

Direction	$\{\rho$/bohr, δ/rad$\}$	Frequency/cm^{-1}
Reactant	{12, 0.679}	3775
Product	{12, 0.0588}	3913

From Table 4.14, the vibrational frequency of the reactant is much higher than that of the reactants in R1 and R2 (Tables 4.4 and 4.9 respectively). This is once again attributed to the unusually strong C–H bond in cyclopropane[113,151,152] as compared to CH_4 and C_2H_6. The points in Tables 4.13 and 4.14 are shown together with the RD PES[113] in Fig 4.17.

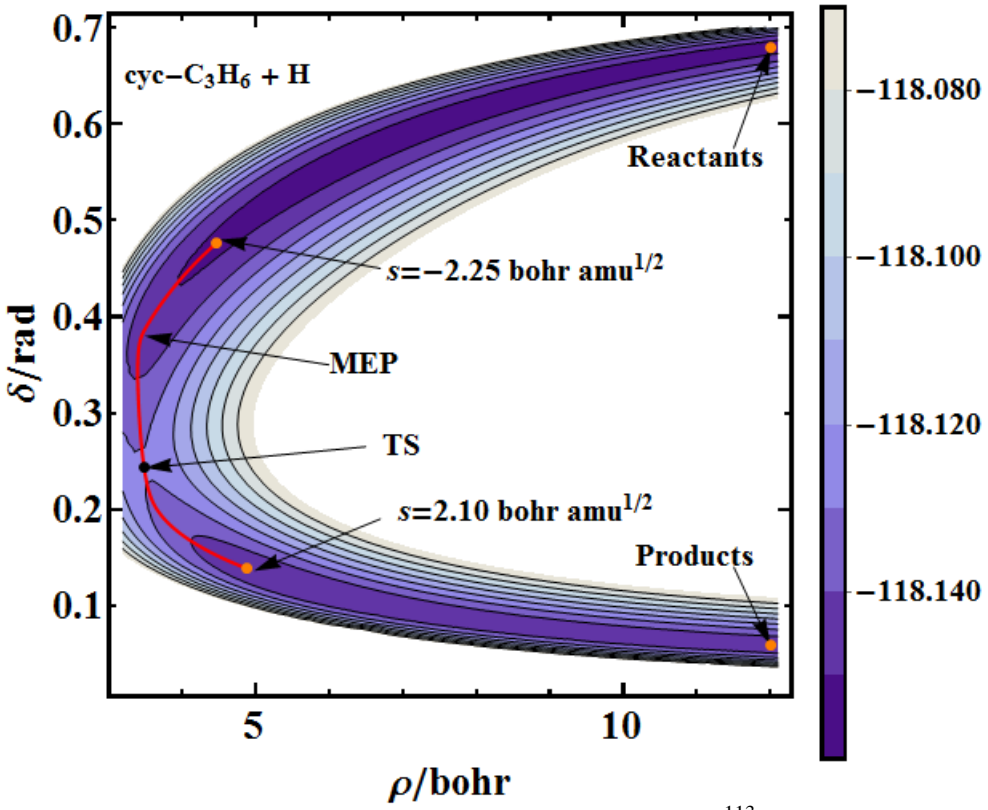


Figure 4.17: The contour plot of the RD PES of R3 by Shan *et al.*[113] with the spectator modes treated in rectilinear coordinates. Black dot is the TS on the RD PES, brown dots are points listed in Tables 4.13 and 4.14 (as labelled) and red curve is the MEP calculated from the TS using Euler's steepest descent method. Bar legend on the right gives the energy of the contour plot in E_h.

Using MI for interpolation, the resulting potential energy, adiabatic potential energy and ZPE curves are given in Fig 4.18. From Fig 4.18, it is seen that the threshold energy for the evaluation of the transmission probability is the energy of the products, and it was calculated to be 0.20 eV. Using the adiabatic ground state potential energy curve in Fig 4.18, the reaction rate constants were calculated using TST/ZCT (MI) and TST/SCT (MI).

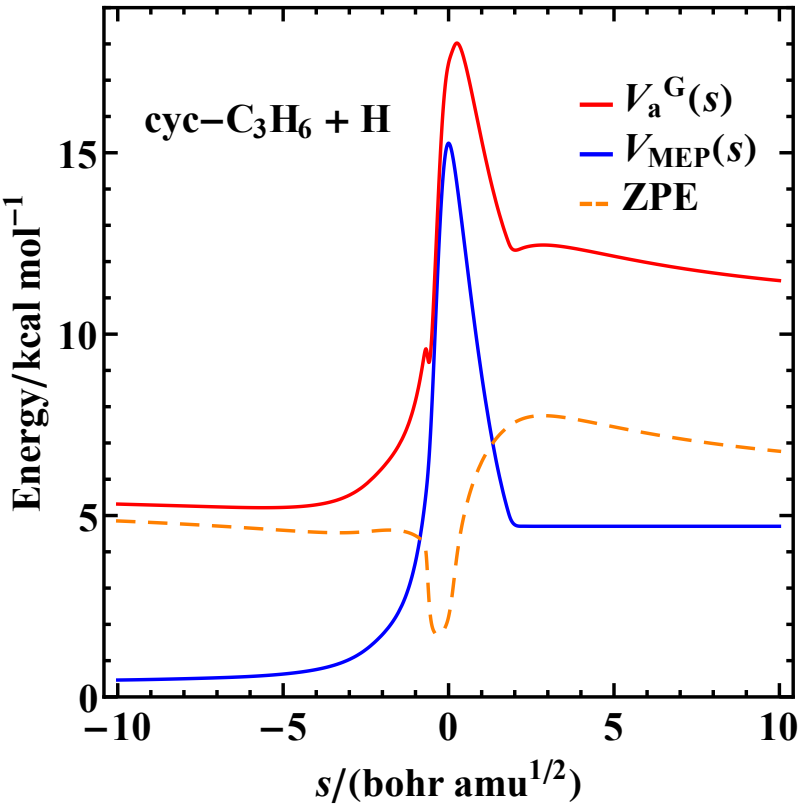


Figure 4.18: Illustration of the adiabatic ground state potential energy (red), MEP potential energy (blue) and ZPE (orange) along the MEP for R3 calculated using MI.

4.3.2 Reaction Rate Constants

The reaction rate constants calculated using TST, TST/ZCT (MI), TST/SCT (MI), QRS[113] and experimental data[151,152] are given in Table 4.15.

Table 4.15: Reaction rate constants for cyc-$C_3H_6 + H$ in cm^3 $molecule^{-1}$ s^{-1}. Number in parentheses denote the powers of 10. Results for TST/ZCT and TST/SCT were calculated using the MI method.

Temperature/K	TST	TST/ZCT	TST/SCT	QRS[109]	Experiment[151,152]
360	6.52(-19)	4.28(-18)	6.32(-18)	8.08(-18)	2.05(-17)[152]
390	2.91(-18)	1.59(-17)	2.21(-17)	2.83(-17)	7.25(-17)[152]
420	3.06(-17)	4.96(-17)	6.60(-17)	8.38(-17)	2.14(-16)[152]
450	3.27(-17)	1.34(-16)	1.73(-16)	2.17(-16)	5.45(-16)[152]
480	8.81(-17)	3.25(-16)	4.05(-16)	5.02(-16)	1.24(-15)[152]
510	2.13(-16)	7.15(-16)	8.69(-16)	1.06(-15)	2.55(-15)[152]
540	4.68(-16)	1.45(-15)	1.73(-15)	2.08(-15)	4.84(-15)[152]
630	3.27(-15)	8.36(-15)	9.50(-15)	1.09(-14)	6.23(-15)[151]
660	5.59(-15)	1.36(-14)	1.53(-14)	1.73(-14)	9.50(-15)[151]
690	9.17(-15)	2.13(-14)	2.37(-14)	2.64(-14)	1.40(-14)[151]
720	1.45(-14)	3.23(-14)	3.56(-14)	3.91(-14)	1.99(-14)[151]
750	2.21(-14)	4.74(-14)	5.19(-14)	5.63(-14)	2.75(-14)[151]

The reaction rate constants are also given in Fig 4.19. From both Table 4.15 and Fig 4.19, TST/ZCT (MI) and TST/SCT (MI) converge with TST results at high temperatures, i.e. >1000K. This is expected as quantum effects are not significant at high temperatures. At low temperatures, similar to R1 and R2, the curves for QRS, TST/ZCT (MI) and TST/SCT (MI) diverge from TST. This further shows the inadequacy of TST to produce accurate reaction rate constants at low temperatures. In particular, QRS, TST/SCT (MI) and TST/ZCT (MI) produced reaction rate constants that were 12, 10 and 7 times larger than those obtained from TST calculations at 360K. When comparing with QRS results, TST/SCT (MI) had excellent agreement with QRS, with a maximum discrepancy of 22% at 360K. When comparing with experimental results, TST/SCT (MI) and TST/ZCT (MI)

also had good agreement with experimental results across the entire temperature range, with a maximum difference at 360K where the experimental reaction rate constant was 3 times larger than TST/SCT (MI) ones.[113]

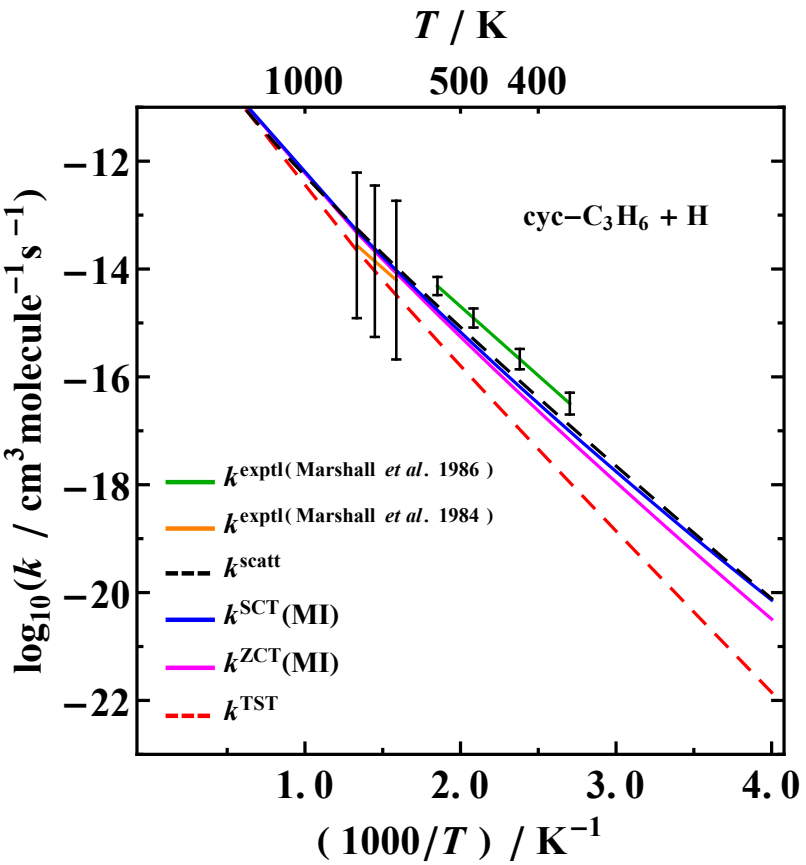


Figure 4.19: Plots of the reaction rate constants in logarithmic scale against 1000/T (where T is the temperature) for R3 using the MI method. Results obtained from experimental data by Marshall *et al.*,[151,152] QRS,[113] TST/SCT (MI), TST/ZCT (MI) and TST are in green, orange, black, blue, pink and red respectively.

4.3.3 Summary for cyc-$C_3H_6 + H \longrightarrow$ cyc-$C_3H_5 + H_2$

When TST/ZCT (MI) and TST/SCT (MI) were tested on the RD PES for R3,[113] it was found that the inclusion of MI in the methods obtained reaction rate constants that had good agreement to both QRS[113] and experimental ones.[151,152] Due to the structural difference between cyclopropane and the linear alkanes studied in R1 and R2, this led to difference in the vibrational frequencies obtained in the TS and the reactants. However, quantum

effects are still important in R3 due to the transfer of the hydrogen atom in the reaction which is absent in TST calculations and insufficiently accounted for in TST/ZCT (MI) due to the lack of consideration of reaction path curvature when evaluating the transmission coefficients.

4.4 Conclusion for Hydrogen Abstraction Reactions

In the tests of TST/ZCT and TST/SCT methods on available RD PESs for R1,[112] R2,[109] and R3,[113] quantum tunnelling was found to be important in these hydrogen abstraction reactions especially at low temperatures; the significance of quantum effects decrease as temperature increases. The mapped interpolation procedure was also found to improve TST/ZCT and TST/SCT results by using vibrational frequencies and potential energies of the reactants and products in the construction of the adiabatic ground state potential energy curves and determination of the threshold energy used when evaluating the transmission coefficients. When comparing between TST/ZCT (MI) and TST/SCT (MI), it was found that TST/ZCT (MI) always produced reaction rate constants that were smaller than TST/SCT (MI). This is due to the lack of accounting for reaction path curvature in TST/ZCT (MI) which is present in TST/SCT (MI). As a result, in all three reactions, TST/SCT (MI) reaction rate constants had better agreement to QRS ones especially at low temperatures where quantum effects were important. Therefore, in subsequent reaction rate constants calculations for hydrogen exchange reactions, TST/ZCT (MI) results would not be presented.

Chapter 5

Hydrogen Exchange Reactions

In the previous chapter, reaction rate constants of three hydrogen abstraction reactions were computed using Transition State Theory with multi-dimensional tunnelling (TST/MT) applied to the so-called reduced dimensionality potential energy surfaces (RD PES) and compared with quantum reactive scattering (QRS) results and experimental data. Since hydrogen atoms were transferred between the reactant molecules in hydrogen abstraction reactions, it was found that quantum effects were significant in these reactions. It was also found that TST with small curvature tunnelling (TST/SCT) with mapped interpolation (MI) produced the best agreement to QRS results and experimental data even at low temperatures where such quantum effects were dominant. However, the PESs of the three reactions studied in the previous chapter had small reaction path curvatures. Therefore, it was sufficient for SCT calculations to have good agreement with QRS ones.

In this chapter, the hydrogen exchange reaction,

$$CH_4 + CH_3 \longrightarrow CH_3 + CH_4 \qquad \text{(R4)}$$

was used to study the effects of TST with large curvature tunnelling (TST/LCT). R4 has a heavy-light-heavy (HLH) mass combination due to the two heavy methyl groups involved

in the exchange reaction as compared to the light mass of the exchanged hydrogen atom. Such reactions with a HLH mass combination will be expected to have a large reaction path curvature.[112] As a result, this might lead to significant corner-cutting effects which could be studied using TST/LCT.[39] TST/SCT (MI) and TST/LCT (MI) will be used to test the significance of extreme corner-cutting effects on the RD PES reported by Remmert[110] for the reaction. To our best knowledge, TST/MT calculations have not yet been applied to test the accuracy of the method with respect to QRS calculations on the same PES for the reaction.

In order to study the effects of deuteration for reaction R4, TST/SCT (MI) and TST/LCT (MI) calculations were also performed on the deuterated reactions

$$CH_3D + CH_3 \longrightarrow CH_3 + CH_3D \tag{R5}$$

$$CD_4 + CD_3 \longrightarrow CD_3 + CD_4 \tag{R6}$$

to obtain their reaction rate constants. Reaction R5 was used to study the primary kinetic isotope effect (KIE) when the exchanged hydrogen atom was substituted with its deuterium isotope, and reaction R6 was used to study the secondary KIE with respect to R5 when the hydrogen atoms that were not involved in the exchange reaction directly were substituted with deuterium atoms. The results for reaction R4 will first be presented next.

5.1 $CH_4 + CH_3 \longrightarrow CH_3 + CH_4$

Reaction R4 is the simplest reaction in the reaction class of $RH + CH_3$[110] and has a HLH mass combination due to the heavy methyl groups involved in the exchange of a light hydrogen atom. Reactions with such mass combinations are known to have a large reaction path curvature.[80,153] In these reactions, corner-cutting effects are expected to be significant, and quantum tunnelling occurs along paths that are on the concave side of the minimum

energy path (MEP) on the PES.[145] An extreme case of such tunnelling is to tunnel along straight line paths from the reactant valley to the product valley which are considered in TST/LCT.[39,87] These paths provide the shortest possible tunnelling route between the reactant and product valleys. In this section, the results for TST/SCT (MI) and TST/LCT (MI) will be presented to study the extent of corner-cutting effects.

5.1.1 Transition State Theory with Small-Curvature Tunnelling

5.1.1.1 Minimum Energy Path

For R4, the MEP was calculated on the RD PES reported by Remmert[110] from the transition state (TS) to the reactants and products. The properties of the TS on the RD PES are given in Table 5.1.

Table 5.1: Properties of the TS on the RD PES[110] for $CH_4 + CH_3$.

$\{\rho$/bohr, δ/rad$\}$	Frequency/cm^{-1}
{9.10, 0.178}	498

Comparing Table 5.1 with Tables 4.1, 4.6 and 4.12, the vibrational frequency for the TS of R4 is smaller than those for the hydrogen abstraction reactions. This is attributed to the symmetric HLH mass combination of R4. In a HLH reacting system, a light atom, i.e. a hydrogen atom, is transferred between two heavy groups, which in this case, are the CH_3 pseudo-atoms. Since the reaction is a symmetric one, at the TS, the central hydrogen atom does not move in a symmetric stretch.[79] As a result, this increases the effective mass of the vibrational motion due to the motion of the heavier methyl groups. As described previously in Sec. 2.2.2, the PES was formulated in a way such that the reduced mass was the same on the entire PES.[38,39] Therefore, a larger effective mass for the vibrational motion resulted in a wider potential energy well for the vibrational motion. This led to a lower vibrational frequency at the TS for R4 as compared to R1–R3 which had a light-

light-heavy mass combination.[79] The MEP calculated is shown together with the contour plot of the RD PES in its range of validity (7.4 bohr $\leq \rho \leq$ 15 bohr)[110] in Fig 5.1.

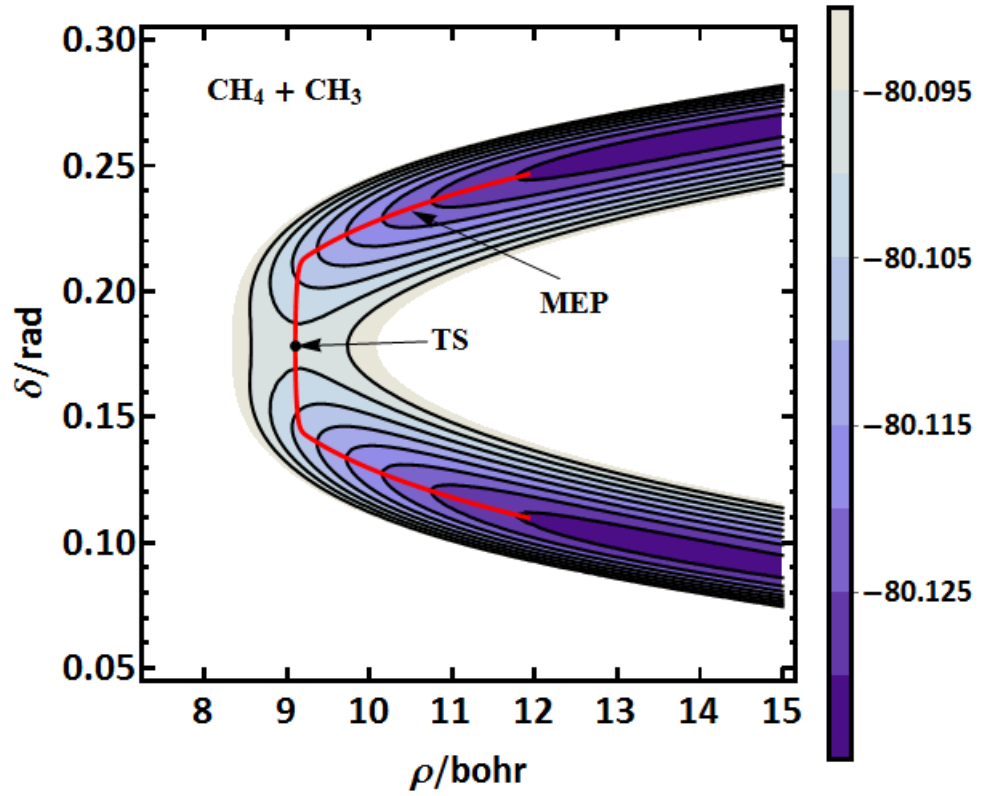


Figure 5.1: The contour plot of the RD PES of R4 by Remmert[110] with the spectator modes treated in curvilinear coordinates. Black dot is the TS on the RD PES and red curve is the MEP calculated from the TS using Euler's steepest descent method. Bar legend on the right gives the energy of the contour plot in E_h.

From Fig 5.1, the δ range for R4 is smaller that those in Figs 4.1, 4.9 and 4.17. This is once again due to the HLH reacting system which results in a larger reaction path curvature for the RD PES. Also, the contour plot is symmetrical since the hydrogen exchange occurs between two CH_3 groups. Similar to reactions R1–R3, the MEP was calculated with a step-size of 0.01 bohr amu$^{1/2}$. In the calculation, the vibrational frequencies became physically not meaningful at $s = \pm$ 5.00 bohr amu$^{1/2}$ in both asymptotic regions due to the symmetry in the reaction. The properties of the reacting system at these points are given in Table 5.2.

Table 5.2: Properties of reacting system at boundaries for MI for $CH_4 + CH_3$.

s/bohr amu$^{1/2}$	$\{\rho$/bohr, δ/rad$\}$	Frequency/cm^{-1}
-5.00	{11.92, 0.247}	3530
5.00	{11.92, 0.110}	3530

From Table 5.2, the ρ values and vibrational frequencies of the reacting system in both asymptotic regions are the same. This is expected since the contour plot is symmetrical and the stepsizes taken in both directions from the TS are the same. Beyond the range -5.00 bohr amu$^{1/2} \leq s \leq$ 5.00 bohr amu$^{1/2}$, MI was used to interpolate information required for the calculation of the TST/SCT (MI) reaction rate constants. Similar to reactions R1–R3, the reactants and products were located by finding the minimum points on the RD PES at the maximum ρ validity, i.e. $\rho = 15$ bohr.[110] The properties of the reactants and products are given in Table 5.3.

Table 5.3: Properties of reactants and products at $\rho = 15$ bohr for $CH_4 + CH_3$.

Direction	$\{\rho$/bohr, δ/rad$\}$	Frequency/cm^{-1}
Reactant	{15, 0.266}	3123
Product	{15, 0.0902}	3123

Similar to Table 5.2, the vibrational frequencies at both reactants and products are the same. This is due to the equivalent C–H vibrational motions that are considered in both reactants and products in the symmetrical reaction. Using MI, the resulting potential energy, adiabatic potential energy and zero point energy (ZPE) curves are given in Fig 5.2. From Fig 5.2, the adiabatic ground state potential energy curve is close to that of the potential energy curve along the MEP at the TS. This is attributed to the small vibrational frequency at the TS which is also shown in the ZPE curve in Fig 5.2 where the ZPE is small (1.42 kcal mol^{-1}). Due to the symmetry in the contour plot, the potential energy, adiabatic ground state potential energy and ZPE curves are all symmetric in Fig 5.2.

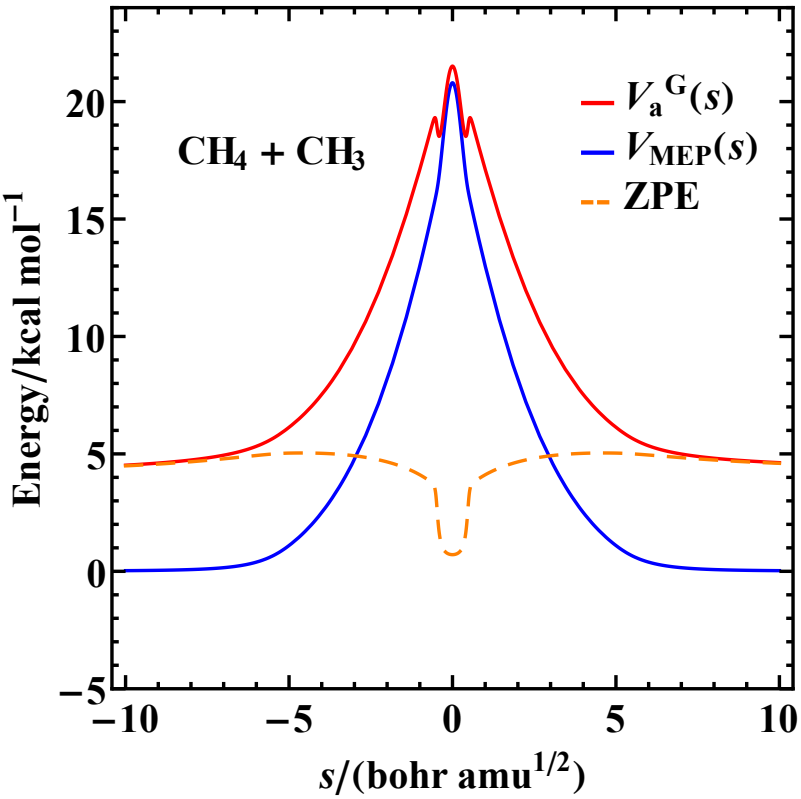


Figure 5.2: Illustration of the adiabatic ground state potential energy (red), MEP potential energy (blue) and ZPE (orange) along the MEP for R4 calculated using MI.

In the calculation of the transmission probability, the threshold energy is 0 eV due to the symmetric reaction. Using the adiabatic ground state potential energy curve in Fig 5.2, the reaction rate constants were evaluated using TST/SCT (MI). The reaction rate constants for TST, TST/SCT (MI) and QRS are given in Table 5.4 and Fig 5.3.

Table 5.4: Reaction rate constants for $CH_4 + CH_3$ in cm^3 $molecule^{-1}$ s^{-1}. Number in parentheses denote the powers of 10. Results for TST/SCT were calculated using the MI method.

Temperature/K	TST	TST/SCT	QRS[110]
250	1.09(-27)	9.48(-26)	2.74(-24)
300	4.02(-25)	1.17(-23)	1.12(-22)
400	7.15(-22)	6.18(-21)	2.30(-20)
500	7.15(-20)	3.30(-19)	8.21(-19)
600	1.69(-18)	5.38(-18)	1.06(-17)
800	1.06(-16)	2.26(-16)	3.29(-16)
1000	1.51(-15)	2.61(-15)	3.06(-15)
1500	7.60(-14)	1.04(-13)	8.11(-14)
2000	7.20(-13)	8.80(-13)	5.29(-13)
2500	3.28(-12)	3.73(-12)	1.88(-12)

From Table 5.4 and Fig 5.3, the TST, TST/SCT (MI) and QRS reaction rate constants converge at high temperatures, i.e. >1000K. Such behaviour is expected due to the decrease in quantum effects at higher temperatures. At low temperatures, the curves in Fig 5.3 diverge, and both TST/SCT (MI) and QRS methods produced much larger reaction rate constants as compared to TST. In particular, the reaction rate constants from TST/SCT (MI) and QRS were 87 and 2514 times larger than that the reaction rate constant obtained from TST at 250K. This showed that quantum tunnelling played a crucial role in the reaction at low temperatures. This was due to the exchange of a light hydrogen atom where quantum effects were important.[22]

Comparing TST/SCT (MI) to QRS results, TST/SCT (MI) did not have excellent agreement to QRS at low temperatures unlike in reactions R1–R3 presented in the previous chapter. At 250K, QRS reaction rate constant was 29 times larger than that of TST/SCT (MI). This is due to the larger reaction path curvature in the PES for reaction R4 as compared to reactions R1–R3 with a light-light-heavy mass combination.[79] In SCT, the MEP was used as the tunnelling path for the reacting system to tunnel through the adiabatic ground state potential energy barrier. This may be less favourable in a reaction like R4 where the

PES has a larger reaction path curvature. This is because the distance between the reactant and product valleys may be sufficiently small such that tunnelling becomes more effective when the reacting system tunnels through a shorter tunnelling path with a larger barrier height than a larger tunnelling path with a smaller barrier height (the adiabatic ground state potential energy along the MEP). Therefore, TST/SCT (MI) underestimated the reaction rate constants as compared to QRS ones at low temperatures.

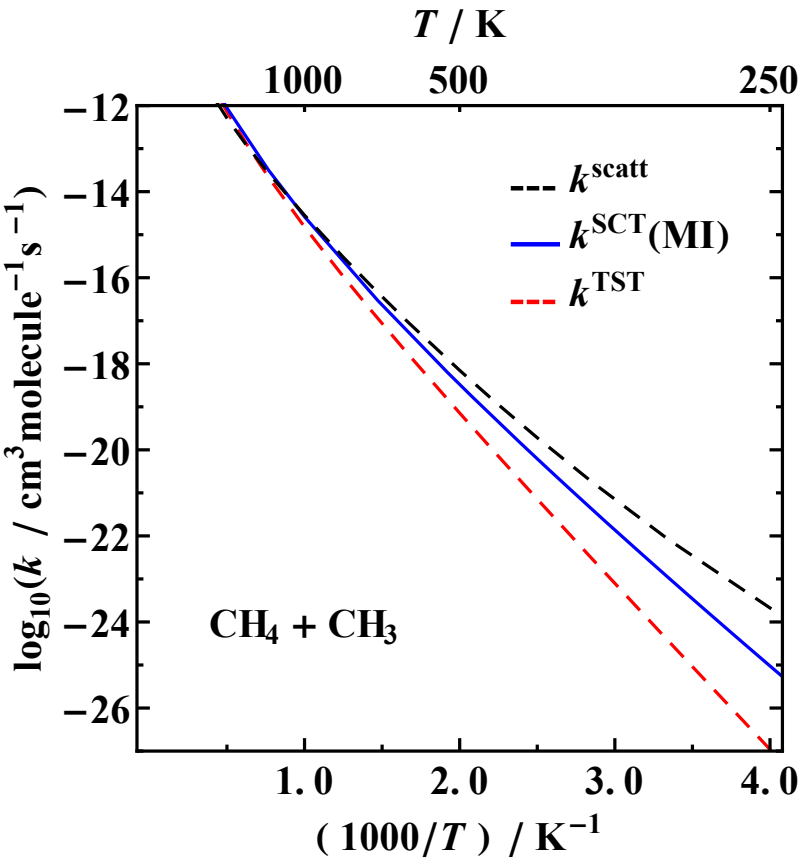


Figure 5.3: Plots of the reaction rate constants in logarithmic scale against 1000/T (where T is the temperature) for R4 using the MI method. Results obtained from QRS,[110] TST/SCT (MI) and TST are in black, blue and red respectively.

Due to the lack of agreement between TST/SCT (MI) and QRS results, TST/LCT (MI) calculations were carried out to study the effects of extreme corner-cutting in LCT to the reaction rate constants. The results for TST/LCT (MI) will be presented in the next section.

5.1.2 Transition State Theory with Large-Curvature Tunnelling

5.1.2.1 Minimum Energy Path

In the TST/LCT (MI) calculations, geometries of the reacting system in the reactant and product valleys were required to calculate the direction vector of the straight-line tunnelling path at each energy (as defined in Eq 2.67).[39] The MEP constructed with the use of MI is shown in Fig 5.4.

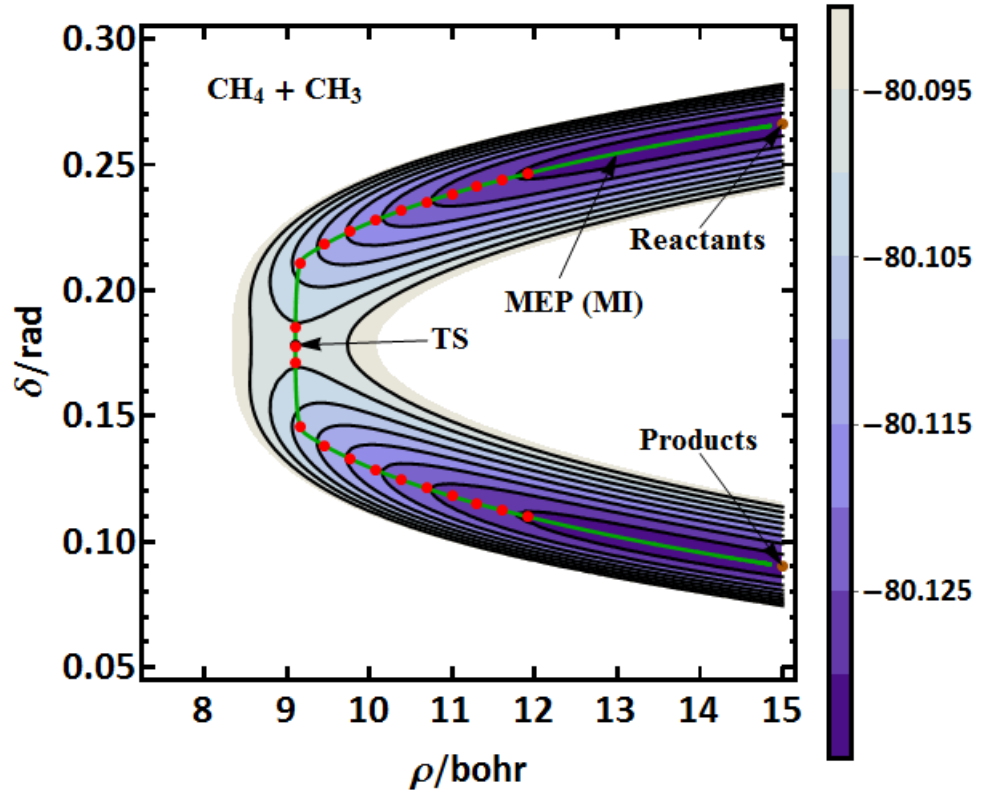


Figure 5.4: The contour plot of the RD PES of R4 by Remmert[110] with the spectator modes treated in curvilinear coordinates. Red dots on the RD PES represent the points along the MEP calculated by Euler's steepest descent method and green curve is the MEP calculated by MI using additional information from the reactants and products on the RD PES (in brown). Bar legend on the right gives the energy of the contour plot in E_h.

From Fig 5.4, the MEP calculated by MI passes through the minimum points on the RD PES in both the reactant and product valleys. This implied that MI was sufficiently accurate to interpolate the geometries of the reacting system beyond the points where the vibrational

frequencies became physically not meaningful. Therefore, the mass-weighted Cartesian coordinates required for LCT calculations obtained from the hyperspherical coordinates on the RD PES would also be accurate for R4. These coordinates were used to define the LCT tunnelling paths from the reactant valley to the product valley. The resulting potential energy curve for each tunnelling path was then used to calculate the LCT barrier penetration integral as described in Sec. 2.2.4. Two of such tunnelling paths will be used as an illustration in the next section.

5.1.2.2 LCT Tunnelling Path

Without any loss of generality, two tunnelling paths were chosen and are shown in Fig 5.5.

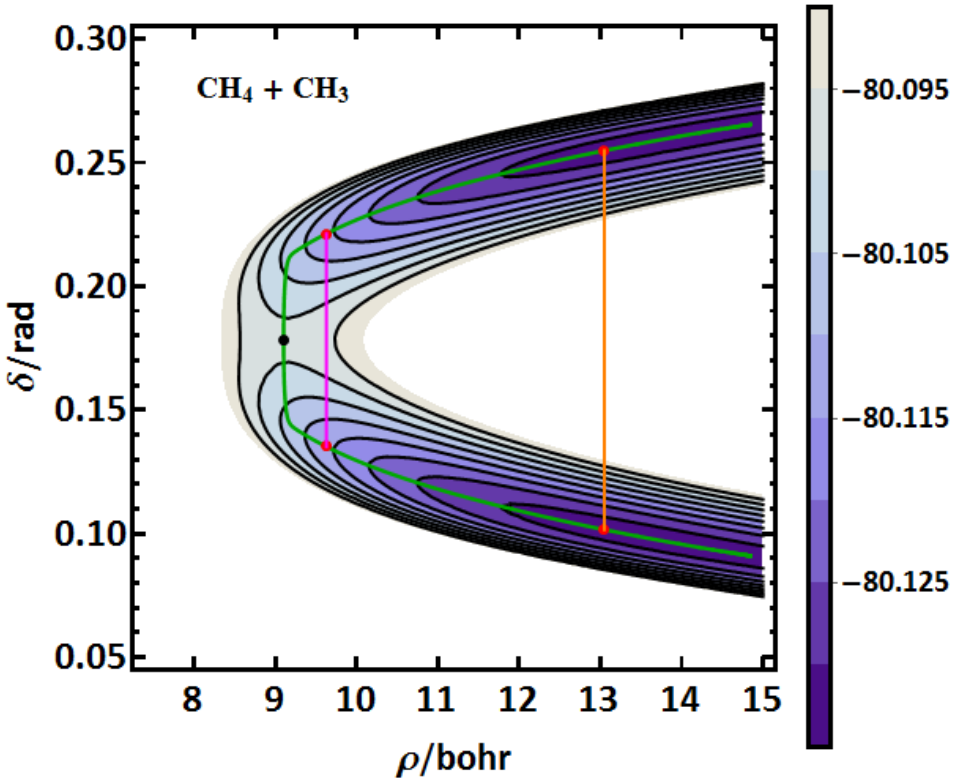


Figure 5.5: The contour plot of the RD PES of R4 by Remmert[110] with the spectator modes treated in curvilinear coordinates. Black dot is the TS on the RD PES and green curve is the MEP calculated by MI. Red dots represent the points in the reactant and product valleys that define the LCT tunnelling paths (in brown and pink). Bar legend on the right gives the energy of the contour plot in E_h.

In Fig 5.5, the brown line represents a straight-line LCT tunnelling path that is far from the MEP on the concave side of the MEP, and the pink line represents a second LCT tunnelling path that is close to the MEP. Due to the shorter path length of the brown LCT tunnelling path with respect to the green MEP in Fig 5.5, tunnelling may be more effective along the LCT tunnelling path than the MEP. The properties of the points represented in red connecting the brown line in Fig 5.5 are given in Table 5.5.

Table 5.5: Properties of reacting system at points defining the brown LCT tunnelling path in Fig 5.5 for $CH_4 + CH_3$.

s/bohr amu$^{1/2}$	$\{\rho$/bohr, δ/rad$\}$	Frequency/cm^{-1}	V/E$_h$
-7.92	{13.05, 0.255}	3178	-80.1322
7.92	{13.05, 0.102}	3178	-80.1322

From Table 5.5, the reaction coordinates of the points having the same energy in the reactant and product valleys have the same magnitude. This is due to the symmetry of the reaction, where the adiabatic ground state potential energy is also symmetric (from Fig 5.2). The symmetry of the reaction is also reflected in the same ρ values, vibrational frequencies and energies of these points. The effective tunnelling potential energy curves along both the brown LCT tunnelling path and the MEP are given in Fig 5.6.

In Fig 5.6, both the LCT effective tunnelling potential energy and the adiabatic ground state potential energy were plotted from the same starting point to the same ending point along the MEP, i.e. the red dots connecting the brown line in Fig 5.5. From Fig 5.6, the LCT potential energy curve has a larger barrier height as compared to the MEP barrier height. However, the LCT potential energy curve is also narrower than the adiabatic ground state potential energy curve due to the shorter tunnelling path. From Eq 2.31, a narrower barrier width leads to a smaller barrier penetration integral. This results in larger transmission probabilities. On the other hand, a larger barrier height leads to larger barrier penetration integrals, hence smaller transmission probabilities. The effects of these competing factors were used to study the reaction rates constants obtained from TST/SCT (MI) and TST/LCT

(MI) which will be presented in the next section.

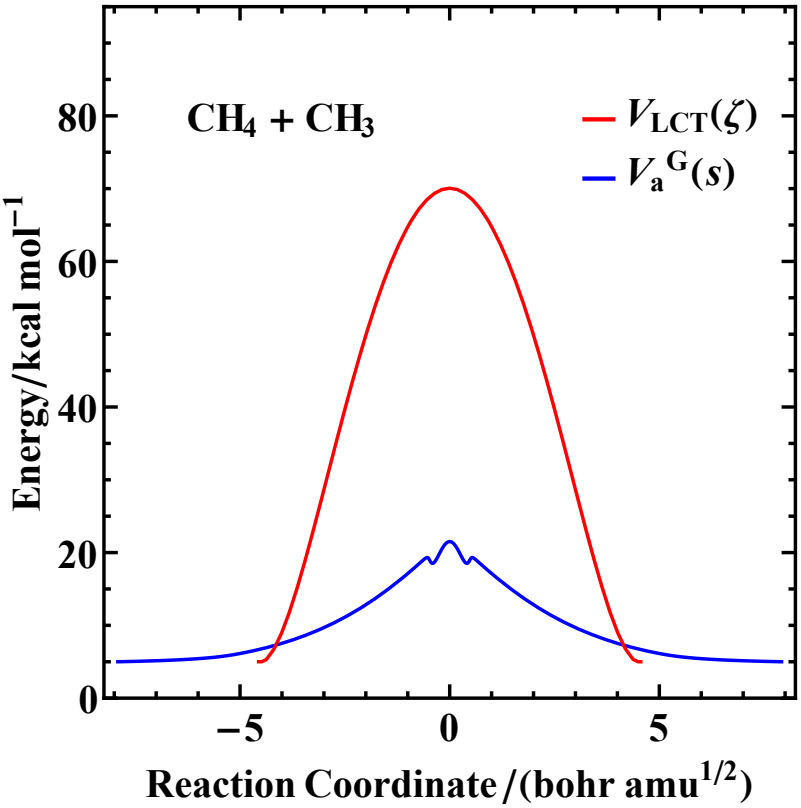


Figure 5.6: The red curve is the LCT potential energy curve along the brown LCT tunnelling path in Fig 5.5 and the blue curve is the adiabatic ground state potential energy along the MEP.

5.1.2.3 Reaction Rate Constants

The reaction rate constants calculated using TST, TST/SCT (MI), TST/LCT (MI), QRS[110] and experimental data[154,155] are given in Table 5.6 and Fig 5.7.

Table 5.6: Reaction rate constants for $CH_4 + CH_3$ in cm^3 $molecule^{-1}$ s^{-1}. Number in parentheses denote the powers of 10. Results for TST/SCT and TST/LCT were calculated using the MI method.

Temperature/K	TST	TST/SCT	TST/LCT	QRS[110]	Experiment[154,155]
250	1.09(-27)	9.48(-26)	5.68(-26)	2.74(-24)	
300	4.02(-25)	1.17(-23)	7.24(-24)	1.12(-22)	2.81(-23)[155]
400	7.15(-22)	6.18(-21)	4.56(-21)	2.30(-20)	1.24(-20)[155]
500	7.15(-20)	3.30(-19)	2.70(-19)	8.21(-19)	4.94(-19)[154]
600	1.69(-18)	5.38(-18)	4.68(-18)	1.06(-17)	5.19(-18)[154]
800	1.06(-16)	2.26(-16)	2.09(-16)	3.29(-16)	9.80(-17)[154]
1000	1.51(-15)	2.61(-15)	2.49(-15)	3.06(-15)	
1500	7.60(-14)	1.04(-13)	1.02(-13)	8.11(-14)	
2000	7.20(-13)	8.80(-13)	8.72(-13)	5.29(-13)	
2500	3.28(-12)	3.73(-12)	3.71(-12)	1.88(-12)	

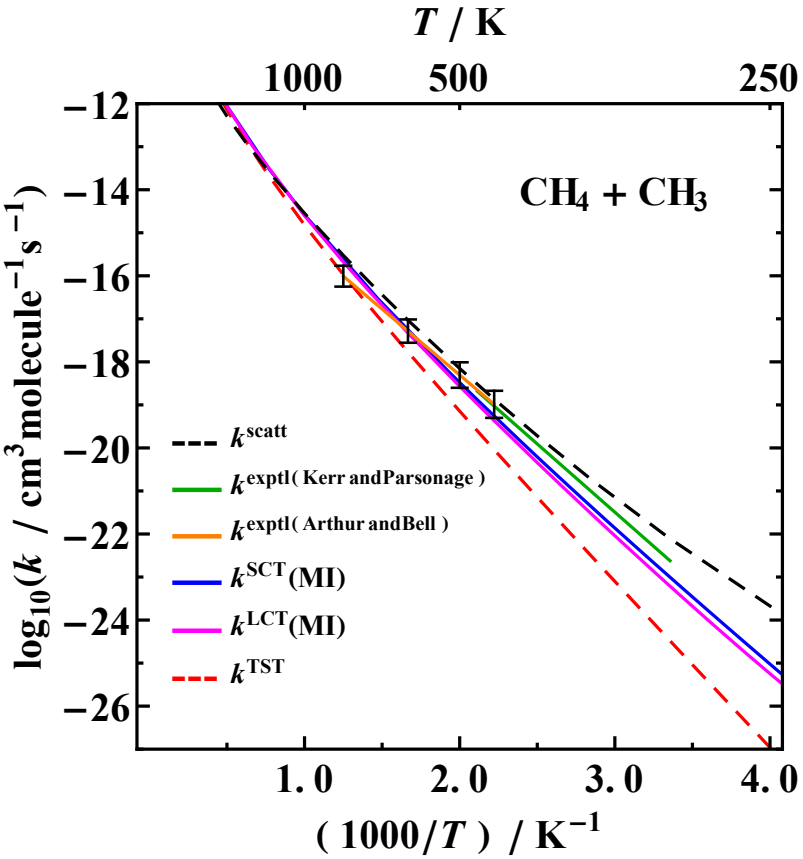


Figure 5.7: Plots of the reaction rate constants in logarithmic scale against 1000/T (where T is the temperature) for R4 using the MI method. Results obtained from QRS,[110] experimental results by Kerr and Parsonage,[154] experimental results by Arthur and Bell,[155] TST/SCT (MI), TST/LCT (MI) and TST are in black, green, orange, blue, pink and red respectively.

From Fig 5.7, it is shown that at high temperatures, similar to reactions R1–R3, all curves converge. This is expected since quantum effects are not significant at high temperatures. The curves also diverge as temperature decreases. The reaction rate constants obtained from the methods that take into account quantum effects were much larger than those obtained from TST. In particular, the reaction rate constants obtained using QRS, TST/SCT (MI) and TST/LCT (MI) were 2514, 87 and 52 times larger than the TST reaction rate constants at 250K. Both TST/SCT (MI) and TST/LCT (MI) also achieved good agreement with respect to experimental data.[154,155]

Comparing TST/SCT (MI) and TST/LCT (MI) reaction rate constants with QRS ones, TST/LCT (MI) did not capture as much quantum tunnelling as TST/SCT (MI) with respect

to QRS when the extreme corner-cutting effects in LCT were taken into account at temperatures lower than 1000K. At higher temperatures, such behaviour was expected. This was because the length of the SCT tunnelling path, i.e. the MEP, would be similar to the length of the LCT tunnelling path as shown by the pink line in Fig 5.5 at higher energies. Also, the effective tunnelling barrier height along the LCT tunnelling path was higher than that along the MEP. Therefore, tunnelling might be favourable along the MEP, resulting in smaller LCT transmission coefficients than SCT ones at higher temperatures. This was reflected in the smaller reaction rate constants obtained by TST/LCT (MI) than TST/SCT (MI) calculations.

At lower temperatures, it was expected that the TST/LCT (MI) reaction rate constants would be larger than TST/SCT (MI) ones, accounting for more tunnelling effects due to the corner-cutting effects resulting from the larger reaction path curvature of the RD PES. However, from Table 5.6 and Fig 5.7, TST/LCT (MI) did not obtain larger reaction rate constants than TST/SCT (MI). Using Fig 5.6 as an illustration, the LCT tunnelling path has a shorter length but a larger barrier height as compared to the MEP. The large barrier height might be a consequence of the intermediate skew angle for the reacting system which led to an intermediate reaction path curvature. Since a shorter tunnelling path and a smaller barrier height reduce the barrier penetration integral hence giving a larger transmission probability, the shorter tunnelling path and larger barrier height of the LCT tunnelling path have competing effects on the transmission probability. From the results obtained from Table 5.6 and Fig 5.7, they seemed to suggest that the smaller barrier height obtained from the adiabatic ground state potential energy curve along the MEP led to the MEP being a better tunnelling path than the straight-line LCT tunnelling paths at low and high energies. As a result, TST/LCT (MI) was less effective in accounting for corner-cutting effects on the RD PES than expected for a reacting system with a HLH mass combination, and the TST/SCT (MI) reaction rate constants were larger than the TST/LCT (MI) ones at all temperatures. The larger barrier height along the LCT tunnelling path might also be due to the

RD nature of the PES. The ZPEs of the spectator modes were included in the construction of the RD PES (previously described in Chapters 2 and 3), unlike in a full-dimensional PES where all vibrational modes were relaxed. Comparison of the reaction rate constants between TST/LCT (MI) and QRS may suggest that the RD nature of the PES affects the RD TST/LCT (MI) calculations more than RD QRS ones when compared against full-dimensional TST/LCT (MI) and QRS calculations respectively since the TST/LCT (MI) reaction rate constants from Table 5.6 and Fig 5.7 were lower than QRS ones at temperatures lower than 1000K.

When comparing TST/SCT (MI) and TST/LCT (MI) reaction rate constants with QRS reaction rate constants, both methods produced smaller reaction rate constants than QRS at low temperatures. In particular, the TST/SCT (MI) and TST/LCT (MI) are 29 and 48 times smaller than QRS ones at 250K. As described previously, the smaller TST/SCT (MI) reaction rate constant as compared to the QRS one was attributed to the lack of consideration of larger reaction path curvature in the TST/SCT (MI) calculations. On the other hand, the results in Table 5.6 and Fig 5.7 seemed to suggest that the case of extreme corner-cutting, where the tunnelling paths are straight-line paths connecting the reactant and product valleys, did not account for sufficient quantum tunnelling as well. Therefore, both the MEP and the straight-line paths do not describe tunnelling in reaction R4 satisfactorily. Instead, a possible tunnelling path that may account for more quantum tunnelling may be an intermediate of the SCT and LCT tunnelling paths such that the effective potential barrier for tunnelling would be smaller than the LCT tunnelling path, and the width of the potential barrier would also be narrower than the MEP used in SCT calculations. A method that could potentially study variable tunnelling paths would be the least-action tunnelling (LAT) method[156] which is not in the scope of this study.

5.1.3 Summary for $CH_4 + CH_3 \longrightarrow CH_3 + CH_4$

In the test of TST/SCT (MI) and TST/LCT (MI) for R4 on the RD PES,[110] it was found that quantum effects were important in the reaction due to the transfer of a hydrogen atom and TST would be inadequate to calculate the reaction rate constants due to the lack of accounting for quantum effects. The comparison between TST/SCT (MI) and TST/LCT (MI) reaction rate constants showed that TST/SCT (MI) recovered more quantum tunnelling than TST/LCT (MI), therefore giving smaller reaction rate constants for TST/LCT (MI). Such results deviated from the expected outcome that TST/LCT (MI) would give larger reaction rate constants than TST/SCT (MI) due to the larger reaction path curvature arising from the HLH mass combination of the reaction. This may be due to the usage of the RD PES that included the ZPEs of the spectator modes, which led to a larger barrier height in the concave region of the RD PES with respect to the MEP. As a result, TST/LCT (MI) was less effective in accounting for tunnelling effects at low temperatures. The lack of agreement of the TST/SCT (MI) and TST/LCT (MI) reaction rate constants with QRS ones may also be due to the non-optimal tunnelling paths used in both SCT and LCT, therefore not accounting for sufficient quantum effects for both methods with respect to QRS. The LAT method could be used to further study intermediate tunnelling paths for the reaction to obtain better agreement to QRS.

5.2 $CH_3D + CH_3 \longrightarrow CH_3 + CH_3D$

In this study, reaction R5 was chosen to study the effects of primary kinetic isotope effect (KIE) of reaction R4. The RD PES used for the reaction treated the spectator modes in curvilinear coordinates and can be found in the literature.[110] With the substitution of the exchanged hydrogen atom with a deuterium atom, it is expected that tunnelling effects may not be as significant in R5 due to the heavier mass of the atom involved in quantum tunnelling.[22] The TST/SCT (MI) and TST/LCT (MI) methods were used to calculate

the reaction rate constants for the reaction which will be compared against results for the unsubstituted reaction to study the primary KIE for reaction R4.

5.2.1 Minimum Energy Path

The MEP for R5 was calculated on the RD PES reported by Remmert[110] from the TS to the reactants and products. The properties of the TS on the RD PES are given in Table 5.7.

Table 5.7: Properties of the TS on the RD PES[110] for $CH_3D + CH_3$.

$\{\rho$/bohr, δ/rad$\}$	Frequency/cm^{-1}
{8.15, 0.246}	503

Comparing Table 5.7 to Table 5.1, the vibrational frequency for the TS of R5 is similar to that of R4 even though the mass of the deuterium atom in R5 transferred is double that of the hydrogen atom in R4. This may be attributed to the symmetric nature of the reaction. In both reactions, there are the central transferred atom, and two methyl groups. Therefore, at the TS, the vibrational frequency would correspond to the movements of the two methyl groups in a symmetric stretch with the central atom being stationary. As a result, the vibrational frequency of the TS in both reactions R4 and R5 are similar.

From the TS, the MEP was calculated to the reaction coordinate of $s = \pm 6.20$ bohr amu$^{1/2}$ using the steepest descent method. The properties of the reacting system at the points $s = \pm 6.20$ bohr amu$^{1/2}$ are given in Table 5.8.

Table 5.8: Properties of reacting system at boundaries for MI for $CH_3D + CH_3$.

s/bohr amu$^{1/2}$	$\{\rho$/bohr, δ/rad$\}$	Frequency/cm^{-1}
-6.20	{11.24, 0.347}	2559
6.20	{11.24, 0.144}	2559

From Table 5.8, the ρ values and vibrational frequencies of the reacting system in both asymptotic regions are the same. This is similar to the results presented previously in Table

5.2. Such result was expected due to the symmetric nature of the reaction. Beyond the range -6.20 bohr amu$^{1/2} \leq s \leq$ 6.20 bohr amu$^{1/2}$ where the vibrational frequencies were physically meaningful, MI was implemented to the maximum range of validity, i.e. $\rho = 13.7$ bohr,[110] of the RD PES. The properties of the reactants and products are given in Table 5.9.

Table 5.9: Properties of reactants and products at $\rho = 13.7$ bohr for $CH_3D + CH_3$.

Direction	$\{\rho$/bohr, δ/rad$\}$	Frequency/cm^{-1}
Reactant	{13.7, 0.370}	2250
Product	{13.7, 0.121}	2250

Comparing Table 5.9 with Table 5.3, the vibrational frequency of the reactants and products for R5 are smaller than that for R4. The vibrational frequency in Table 5.9 corresponds to the vibrational frequency between the carbon atom of the methyl group and the deuterium atom while in Table 5.3, it corresponds to the vibrational frequency between the carbon atom of the methyl group and the transferred hydrogen atom. Since deuterium has a heavier mass than hydrogen, the reduced mass of the diatom CH_3-D is larger than that of CH_3-H. This results in a smaller vibrational frequency. The resulting MEP calculated using steepest descent method and MI is given in Fig 5.8.

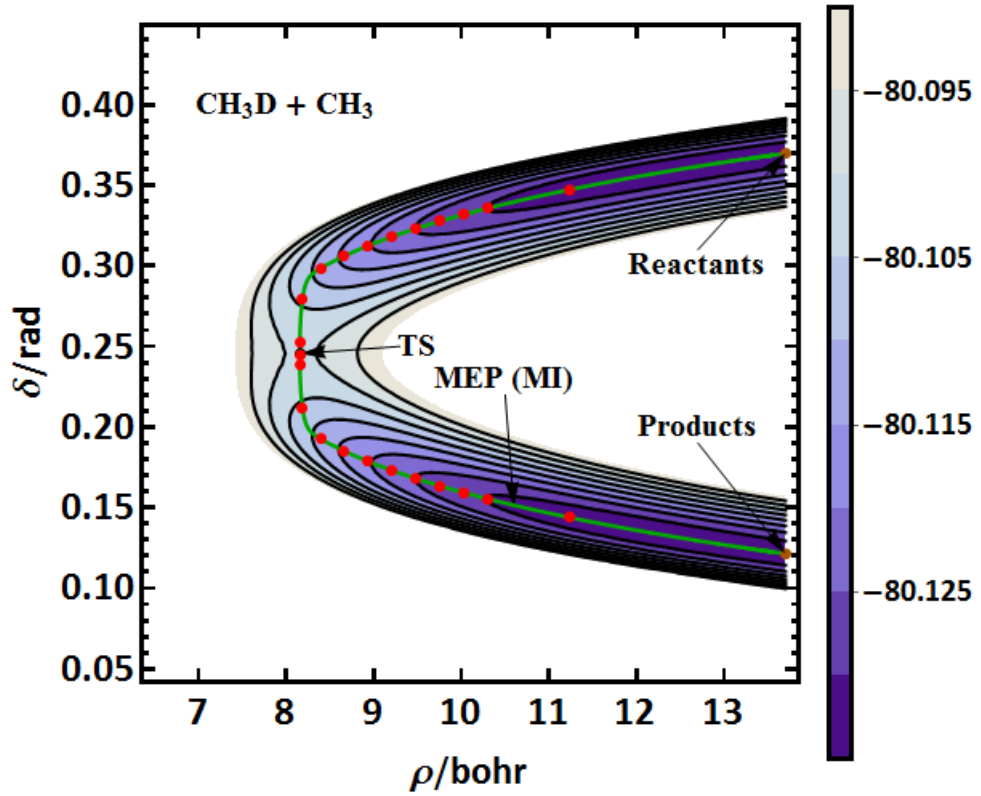


Figure 5.8: The contour plot of the RD PES of R5 by Remmert[110] with the spectator modes treated in curvilinear coordinates. Red dots on the RD PES represent the points along the MEP calculated by Euler's steepest descent method and green curve is the MEP calculated by MI using additional information from the reactants and products on the RD PES (in brown). Bar legend on the right gives the energy of the contour plot in E_h.

From Fig 5.8, the RD PES is symmetric on both sides of the TS which is expected due to the symmetric nature of the reaction. As a result, the MEP calculated was also symmetrical on both sides of the TS. The MEP calculated by MI passes through the minimum of the RD PES as expected. Therefore, the MEP was sufficiently accurate for use in further calculations of the properties required for the computation of the transmission coefficient and reaction rate constants.

Comparison between Fig 5.4 and Fig 5.8 shows that the distance between the reactant and product valleys in Fig 5.8 is larger than that in Fig 5.4, therefore having a smaller reaction path curvature. This is also expected since the difference between the two reactions is the substitution of the exchanged hydrogen atom with a deuterium atom. With a larger

mass of the exchanged atom and the same methyl groups in both the reactants and products, the reaction path curvature for the RD PES of R5 would be smaller as shown in Fig 5.8. With a smaller reaction path curvature, it is expected that TST/LCT would be a less effective tunnelling method in R5 than in R4. On the other hand, it is also expected that TST/SCT would be a more effective tunnelling method in R5 than in R4. The resultant adiabatic ground state potential energy curve calculated along the MEP is given in Fig 5.9.

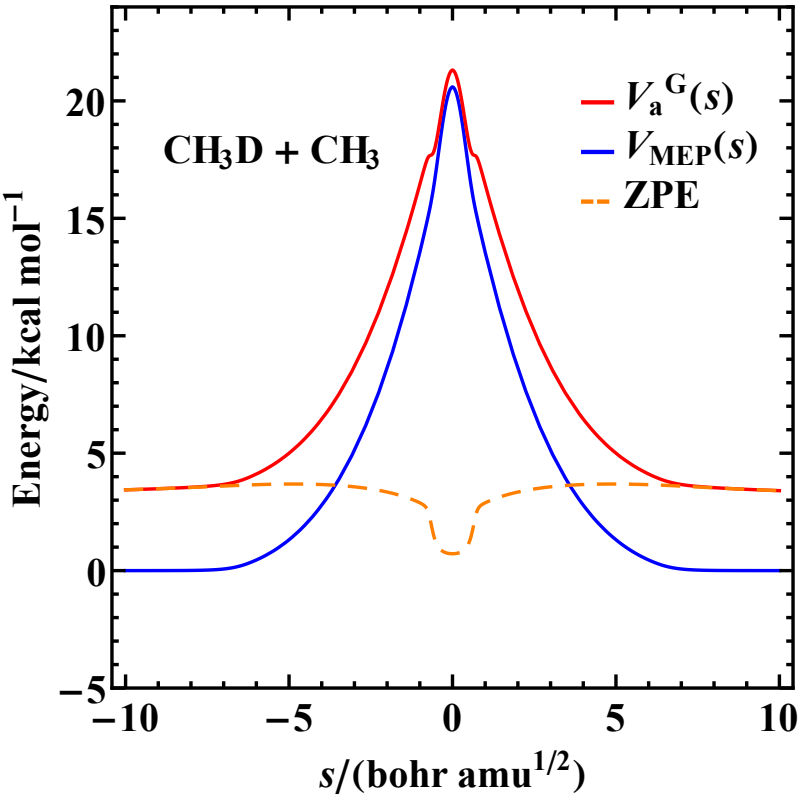


Figure 5.9: Illustration of the adiabatic ground state potential energy (red), MEP potential energy (blue) and ZPE (orange) along the MEP for R5 calculated using MI.

Comparison between Fig 5.2 and Fig 5.9 shows that the ZPE at the reactant and product asymptotic regions are smaller for R5 than for R4. This is due to the smaller vibrational frequency of the CH_3-D bond as compared to the CH_3-H bond as presented previously in Table 5.9. From Fig 5.9, the potential energy and adiabatic ground state potential energy along the MEP are also symmetrical which is due to the symmetric RD PES used in the

calculations reported by Remmert.[110] Using the adiabatic ground state potential energy curve and the additional properties required to calculate the LCT transmission coefficient, the reaction rate constants will be presented next.

5.2.2 Reaction Rate Constants

The reaction rate constants calculated using TST, TST/SCT (MI), TST/LCT (MI), QRS,[110] and experimental data[154] are given in Table 5.10 and Fig 5.10.

Table 5.10: Reaction rate constants for $CH_3D + CH_3$ in cm^3 $molecule^{-1}$ s^{-1}. Number in parentheses denote the powers of 10. Results for TST/SCT and TST/LCT are calculated using the MI method.

Temperature/K	TST	TST/SCT	TST/LCT	QRS[110]	Experiment[154]
250	3.66(-29)	2.03(-27)	7.83(-28)	3.72(-27)	
300	1.82(-26)	3.09(-25)	1.67(-25)	4.41(-25)	
400	4.79(-23)	2.54(-22)	1.88(-22)	3.31(-22)	1.29(-21)[154]
500	6.09(-21)	1.90(-20)	1.59(-20)	2.43(-20)	4.68(-21)[154]
600	1.70(-19)	3.94(-19)	3.52(-19)	4.96(-19)	5.16(-19)[154]
800	1.31(-17)	2.24(-17)	2.12(-17)	2.65(-17)	
1000	2.09(-16)	3.08(-16)	2.99(-16)	3.37(-16)	
1500	1.17(-14)	1.46(-14)	1.44(-14)	1.32(-14)	
2000	1.11(-13)	1.28(-13)	1.28(-13)	9.93(-14)	
2500	4.88(-13)	5.34(-13)	5.34(-13)	3.71(-13)	

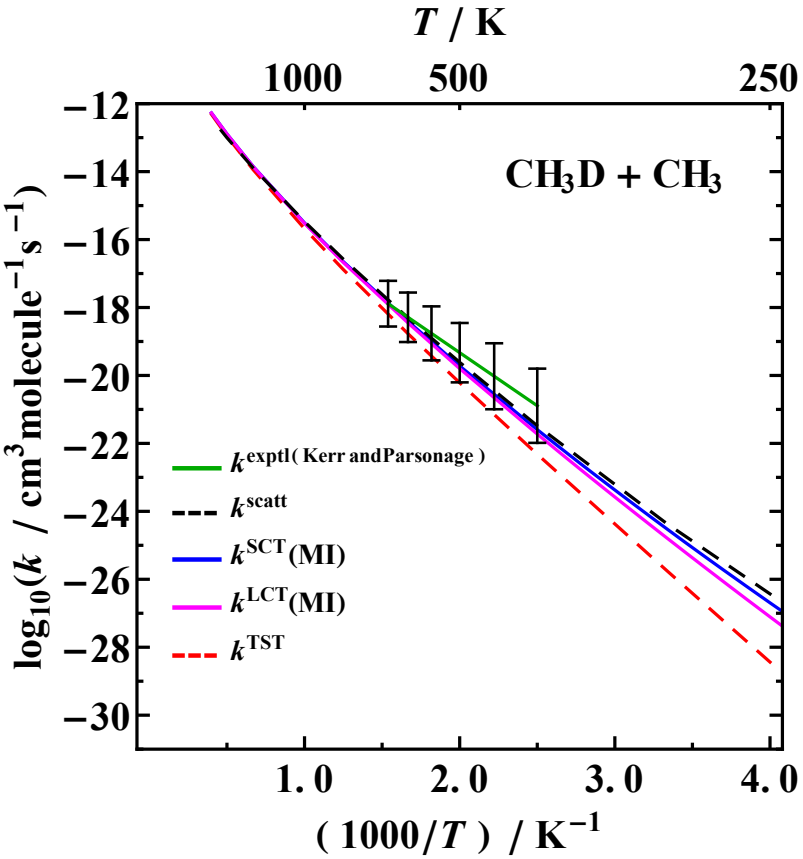


Figure 5.10: Plots of the reaction rate constants in logarithmic scale against 1000/T (where T is the temperature) for R5 using the MI method. Results obtained from experimental data,[154] QRS,[110] TST/SCT (MI), TST/LCT (MI) and TST are in green, black, blue, pink and red respectively.

From Fig 5.10, the reaction rate constants obtained from QRS,[110] TST/LCT (MI) and TST/SCT (MI) converge with those obtained from TST calculations at high temperatures, i.e. >1000K. Such behaviour is once again expected as quantum effects become less significant at higher temperatures. At low temperatures, the curves start to diverge, and the reaction rate constants calculated by QRS, TST/LCT (MI) and TST/SCT (MI) are much larger than those from TST. In particular, at 250K, the QRS, TST/LCT (MI) and TST/SCT (MI) reaction rate constants are 102, 21 and 55 times larger than TST reaction rate constants. However, comparing Table 5.6 with Table 5.10, the quantum effects for R5 is much less significant than for R4. This is due to the transfer of a much heavier deuterium atom in R5 than a hydrogen atom in R4.[22] When comparing with experimental data[154] with the temperature range 400K–650K, TST/SCT (MI) and TST/LCT (MI) lie within the range of

error and therefore have good agreement with experiment.

The reaction rate constants obtained from TST/LCT (MI) are consistently lower than those calculated by TST/SCT (MI) in the temperature range 250K–1500K. Such behaviour may be attributed to the smaller reaction path curvature due to the substitution of the exchanged atom. When the reaction path curvature is reduced, the length of the LCT tunnelling path is no longer sufficiently small such that the increase in transmission probability by tunnelling through a shorter path outweighs the decrease in transmission probability due to the much larger barrier height as compared to the adiabatic ground state potential energy curve.

Comparing TST/SCT (MI) and TST/LCT (MI) with QRS results, there is excellent agreement between TST/SCT (MI) and QRS results. This is expected due to the smaller reaction path curvature due to the heavier exchanged deuterium atom. This is similar to the results obtained in the hydrogen abstraction reactions presented in the previous chapter. In particular, the QRS reaction rate constant is about twice the value of the TST/SCT (MI) reaction rate constant at 250K which is considered to be in good agreement.[86] TST/LCT (MI), on the other did not have as good an agreement with QRS as compared with TST/SCT (MI) at low temperatures due to the small reaction path curvature.

5.2.2.1 Primary Kinetic Isotope Effect

The primary KIE can be studied with the substitution of the exchanged hydrogen atom with its respective isotope. In reaction R5, the exchanged hydrogen atom is substituted with a deuterium atom. The reaction rate constants obtained by TST/SCT (MI) for R4 and for R5 and the KIE are given in Table 5.11.

Table 5.11: Reaction rate constants for $CH_4 + CH_3$ and for $CH_3D + CH_3$ calculated using TST/SCT (MI) in cm^3 $molecule^{-1}$ s^{-1}, and KIE. Number in parentheses denote the powers of 10.

Temperature/K	$CH_4 + CH_3$	$CH_3D + CH_3$	KIE(D/H)
250	9.48(-26)	2.03(-27)	0.0214
300	1.17(-23)	3.09(-25)	0.0264
400	6.18(-21)	2.54(-22)	0.0411
500	3.30(-19)	1.90(-20)	0.0576
600	5.38(-18)	3.94(-19)	0.0732
800	2.26(-16)	2.24(-17)	0.0991
1000	2.61(-15)	3.08(-16)	0.118
1500	1.04(-13)	1.46(-14)	0.140
2000	8.80(-13)	1.28(-13)	0.145
2500	3.73(-12)	5.34(-13)	0.143

From Table 5.11, it is shown that the substitution of the exchanged hydrogen atom with the much heavier deuterium atom reduces the reaction rate constant to a large extent. In particular, the reaction rate constant for reaction R5 is 0.0214 times that of the reaction rate constant for the unsubstituted R4 reaction at 250K. Since quantum effects are much more prominent at lower temperatures, the KIE ratio increases as temperature increases. Also, in CH_3D, there is only one deuterium atom that can be exchanged in the reaction whereas in CH_4, due to the symmetry of the molecule, all four of the hydrogen atoms can be exchanged. However, since the symmetry would reduce the reaction rate constants of R5 by four times, the much smaller reaction rate constants were attributed to the primary KIE due to the substitution.

5.2.3 Summary for $CH_3D + CH_3 \longrightarrow CH_3 + CH_3D$

In the test of TST/SCT (MI) and TST/LCT (MI) on the RD PES reported by Remmert[110] for R5, it was found that the quantum effects were still important in the reaction especially at low temperatures even though the substitution of the exchanged hydrogen atom

was made with a deuterium atom that was double its mass. However, such quantum effects were smaller for reaction R5 than it was for R4. Therefore, even though a deuterium atom was transferred between the methyl groups in the reaction, TST would still be inadequate to calculate the reaction rate constants due to the lack of accounting for quantum effects. Across the temperature range of 250K–1500K, TST/LCT (MI) reaction rate constants were consistently lower than TST/SCT (MI), suggesting that TST/LCT (MI) captured less tunnelling effects than TST/SCT (MI) for the reaction. This was expected since TST/LCT (MI) did not account for more quantum effects than TST/SCT (MI) in the unsubstituted reaction where the reaction path curvature was larger than reaction R5. Due to the smaller reaction path curvature in R5 than its unsubstituted reaction R4, there was excellent agreement between TST/SCT (MI) and QRS results. Comparison between the reaction rate constants of reactions R5 and R4 showed that the effect of primary KIE was large. This was due to the much heavier deuterium atom as compared to the hydrogen atom and symmetry considerations. Therefore, the deuterium is a much less effective atom in quantum tunnelling as compared to a hydrogen atom.

5.3 $CD_4 + CD_3 \longrightarrow CD_3 + CD_4$

Reaction R6 was chosen to study the effects of secondary KIE of reaction R5 where the hydrogen atoms that were not involved in the exchange reaction were substituted by deuterium atoms. With the substitution of the hydrogen atoms that were not exchanged in the reaction, the difference between R6 and R5 would be reflected in the ZPE of the spectator modes that were included in the construction of the RD PES.[110] To study these effects, TST/SCT (MI) and TST/LCT (MI) were applied to the RD PES reported by Remmert.[110]

5.3.1 Minimum Energy Path

For the calculation of the MEP for R6 from the TS to the reactants and products, the properties of the TS on the RD PES are given in Table 5.12.

Table 5.12: Properties of the TS on the RD PES[110] for $CD_4 + CD_3$.

$\{\rho$/bohr, δ/rad$\}$	Frequency/cm^{-1}
{8.17, 0.226}	465

Comparing Table 5.12 with Table 5.1 and Table 5.7, the vibrational frequency of the TS for R6 is smaller than that for R4 and R5. In all three reactions, the vibrational motion at the TS involved the motion of the unsubstituted or substituted methyl groups due to the symmetric nature of the reaction. Therefore, with the larger mass of the substituted methyl group, the vibrational frequency of the TS for R6 was reduced with respect to R4 and R5. From the TS, the MEP of the RD PES was calculated using the steepest descent method in the range -6.50 bohr amu$^{1/2} \leq s \leq$ 6.50 bohr amu$^{1/2}$ and then using MI to the maximum range of validity of the RD PES, i.e. ρ = 13.5 bohr.[110] The properties of the reacting system at the points $\pm$ 6.50 bohr amu$^{1/2}$ are given in Table 5.13.

Table 5.13: Properties of reacting system at boundaries for MI for $CD_4 + CD_3$.

s/bohr amu$^{1/2}$	$\{\rho$/bohr, δ/rad$\}$	Frequency/cm^{-1}
-6.50	{11.07, 0.315}	2573
6.50	{11.07, 0.137}	2573

Similar to Table 5.2 and Table 5.8, the ρ values and vibrational frequencies of the reacting system in both asymptotic regions are the same which is expected of a symmetrical reaction. The reactants and products were defined as the minimum points at the maximum validity of the RD PES, i.e. ρ = 13.5 bohr, and the properties are given in Table 5.14.

Table 5.14: Properties of reactants and products at $\rho = 13.5$ bohr for $CD_4 + CD_3$.

Direction	$\{\rho$/bohr, δ/rad$\}$	Frequency/cm^{-1}
Reactant	{13.5, 0.337}	2267
Product	{13.5, 0.115}	2267

The vibrational frequency of the reactants and products in Table 5.14 are the same since they correspond to the same motion of the CD_3-D bond. Comparing between Table 5.9 and Table 5.14 shows that the vibrational frequencies at the reactants and products are similar. This is expected since the vibrational mode corresponds to a similar stretching of the C–D bond. The resultant MEP computed using the steepest descent and MI method is given in Fig 5.11.

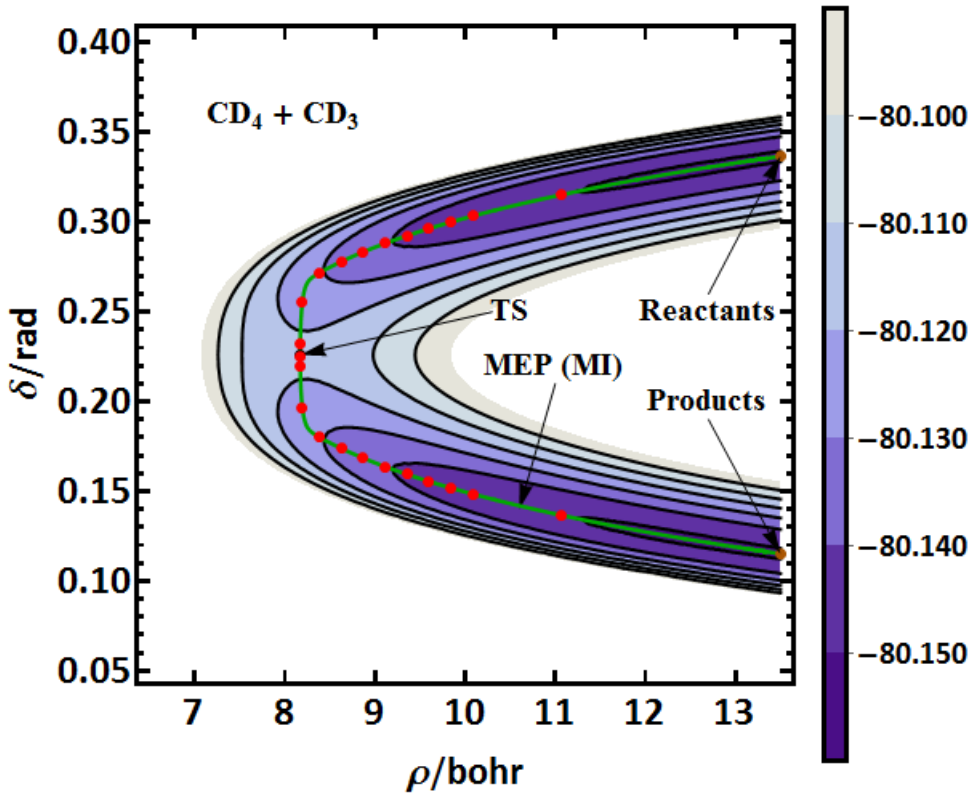


Figure 5.11: The contour plot of the RD PES of R6 by Remmert[110] with the spectator modes treated in curvilinear coordinates. Red dots on the RD PES represent the points along the MEP calculated by Euler's steepest descent method and green curve is the MEP calculated by MI using additional information from the reactants and products on the RD PES (in brown). Bar legend on the right gives the energy of the contour plot in E_h.

From Fig 5.11, it is seen that the contour plot and the MEP calculated are symmetric which is once again expected due to the symmetric nature of the reaction. Also, the MEP passes through the minimum of the RD PES in the area of interpolation between the red dots on the RD PES in Fig 5.11 with the largest ρ value to the reactants and products on the RD PES as labelled. The resultant potential energy and adiabatic ground state potential energy curves along the MEP are shown in Fig 5.12.

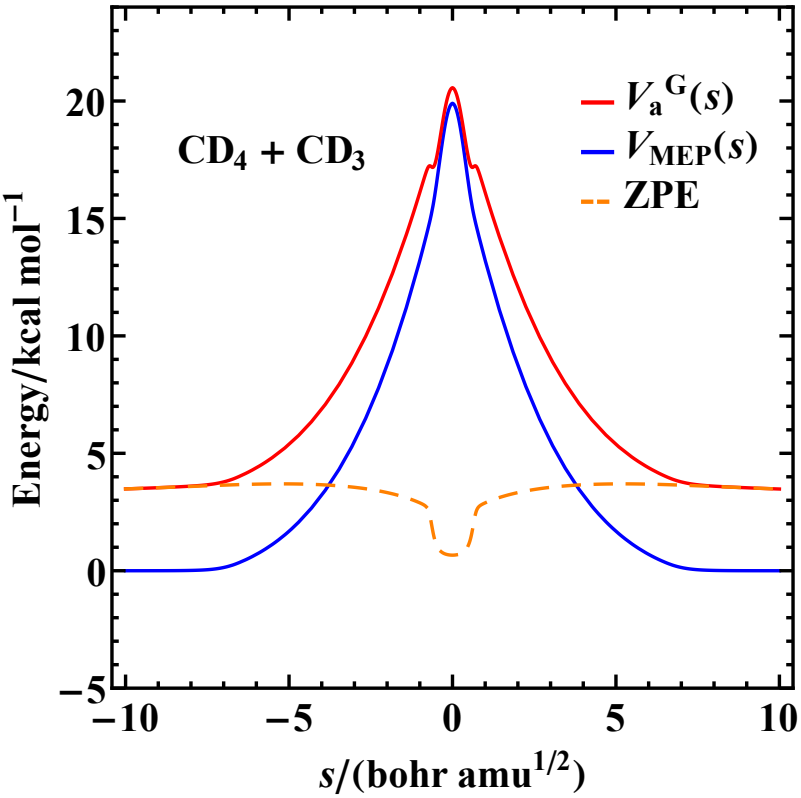


Figure 5.12: Illustration of the adiabatic ground state potential energy (red), MEP potential energy (blue) and ZPE (orange) along the MEP for R6 calculated using MI.

The potential energy, adiabatic ground state potential energy and ZPE curves in Fig 5.12 are symmetrical which is expected due to the symmetrical RD PES. Comparing Fig 5.9 and Fig 5.12, the shape of the potential energy curves are similar. This is due to the similarity in the reactions R5 and R6. In both reactions, a deuterium atom was exchanged between two identical groups. Since the vibrational frequencies of the other vibrational modes other than those corresponding to the bond forming and bond breaking between the

exchanged deuterium and the pseudo-atom groups were included as spectator modes in the construction of the RD PES reported by Remmert,[110] the differences in the vibrational frequencies would not be included directly in the ZPE curves in Fig 5.9 and Fig 5.12. The remaining vibrational frequency corresponds to a similar motion of the CH_3-D-CH_3 or CD_3-D-CD_3 complexes with similar effective reduced masses. Therefore, the ZPE curves in both Fig 5.9 and Fig 5.12 are similar which results in a similar shape of the adiabatic ground state potential energy curves used in subsequent calculations.

5.3.2 Reaction Rate Constants

Using the adiabatic ground state potential energy along the MEP and the properties required to do LCT calculations from the RD PES,[110] the resultant reaction rate constants calculated using TST, TST/SCT (MI), TST/LCT (MI), QRS[110] and experimental data[157] are given in Table 5.15 and Fig 5.13.

Table 5.15: Reaction rate constants $CD_4 + CD_3$ in cm^3 $molecule^{-1}$ s^{-1}. Number in parentheses denote the powers of 10. Results for TST/SCT and TST/LCT are calculated using the MI method.

Temperature/K	TST	TST/SCT	TST/LCT	QRS[110]	Experiment[157]
250	2.21(-28)	9.01(-27)	1.44(-27)	1.93(-26)	
300	9.57(-26)	1.33(-24)	3.64(-25)	2.12(-24)	
400	2.18(-22)	1.04(-21)	5.08(-22)	1.42(-21)	
500	2.59(-20)	7.48(-20)	4.84(-20)	9.89(-20)	1.10(-19)[157]
600	7.00(-19)	1.53(-18)	1.14(-18)	1.95(-18)	2.18(-18)[157]
800	5.26(-17)	8.63(-17)	7.44(-17)	1.00(-16)	
1000	8.37(-16)	1.19(-15)	1.09(-15)	1.23(-15)	
1500	4.83(-14)	5.88(-14)	5.64(-14)	4.36(-14)	
2000	4.86(-13)	5.49(-13)	5.26(-13)	3.00(-13)	
2500	2.28(-12)	2.45(-12)	2.30(-12)	1.03(-12)	

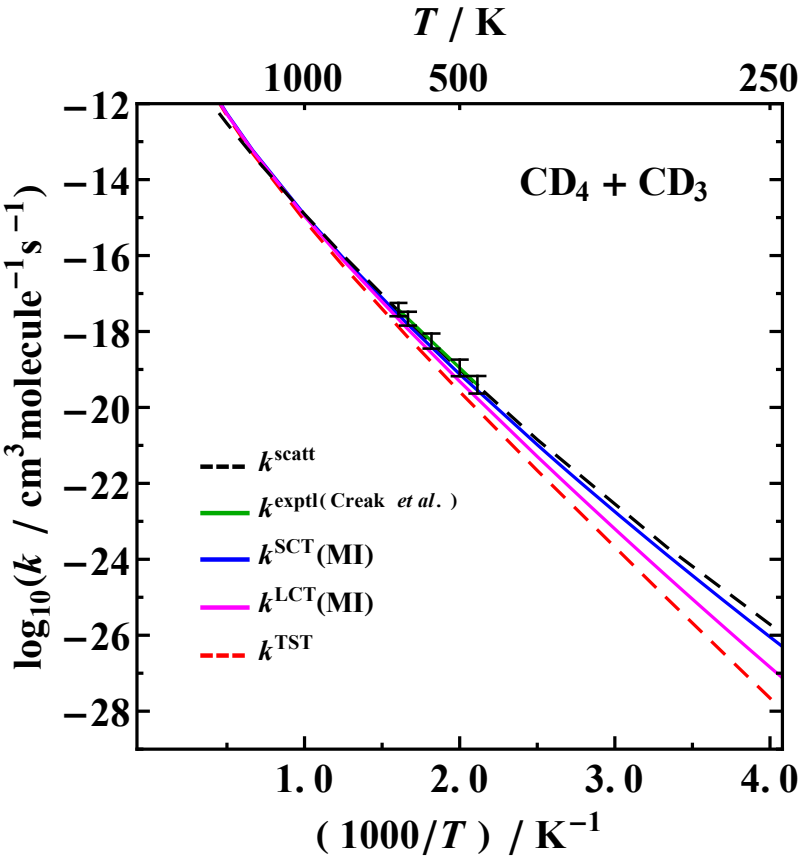


Figure 5.13: Plots of the reaction rate constants in logarithmic scale against 1000/T (where T is the temperature) for R6 using the MI method. Results obtained from QRS,[110] experimental data,[157] TST/SCT (MI), TST/LCT (MI) and TST are in black, green, blue, pink and red respectively.

From Table 5.15 and Fig 5.13, it is shown that at high temperatures, the reaction rate constants computed from TST, TST/SCT (MI), TST/LCT (MI) and QRS[110] converge. This is expected as quantum effects become less significant at these temperatures. At lower temperatures, similar to reactions R4–R5, the curves diverge and the reaction rate constants obtained by TST is much lower than the reaction rate constants obtained by the other methods that take into account the quantum effects. In particular, the QRS,[110] TST/SCT (MI) and TST/LCT (MI) reaction rate constants are 87, 41 and 7 times larger than the TST reaction rate constant at 250K. This shows that for reaction R6, TST is also inadequate to produce accurate reaction rate constants at low temperatures due to the lack of accounting for quantum effects in the method. When comparing the TST/SCT (MI) and TST/LCT (MI) results to experimental ones, the reaction rate constants are in good agreement with

experimental data.[157]

Similar to reaction R5, the TST/LCT (MI) reaction rate constants in Table 5.15 are consistently lower than the TST/SCT (MI) ones across the entire temperature range of 250K–2500K. This is attributed to the smaller reaction path curvature due to the transfer of a heavier deuterium atom than a light hydrogen atom in reaction R4.

Comparing TST/SCT (MI) reaction rate constants with QRS ones, there is excellent agreement between TST/SCT (MI) and QRS. In particular, the QRS reaction rate constant is about twice the value of the TST/SCT (MI) reaction rate constant at 250K which is considered to be good agreement.[86] This is similar to the results presented previously for reaction R5. Since both reactions R5 and R6 are of similar nature where a deuterium atom is exchanged between two symmetric groups that are similar for both reactions, the agreement between TST/SCT (MI) and QRS is expected for this reaction.

5.3.2.1 Secondary Kinetic Isotope Effect

The secondary KIE can be studied with the substitution of the hydrogen atoms of the methyl groups in reaction R5 with deuterium. The reaction rate constants obtained by TST/SCT (MI) for both R5 and R6 and the KIE are given in Table 5.16.

Table 5.16: Reaction rate constants for $CH_3D + CH_3$ and $CD_4 + CD_3$ calculated using TST/SCT (MI) in cm^3 $molecule^{-1}$ s^{-1}, and KIE. Number in parentheses denote the powers of 10.

Temperature/K	$CH_3D + CH_3$	$CD_4 + CD_3$	KIE(D/H)
250	2.03(-27)	9.01(-27)	4.44
300	3.09(-25)	1.33(-24)	4.30
400	2.54(-22)	1.04(-21)	4.09
500	1.90(-20)	7.48(-20)	3.94
600	3.94(-19)	1.53(-18)	3.88
800	2.24(-17)	8.63(-17)	3.85
1000	3.08(-16)	1.19(-15)	3.86
1500	1.46(-14)	5.88(-14)	4.03
2000	1.28(-13)	5.49(-13)	4.29
2500	5.34(-13)	2.45(-12)	4.59

From Table 5.16, the reaction rate constant for R6 is consistently about 4 times larger than the reaction rate constant for R5 throughout the entire temperature range of 250K–2500K. This was attributed to the symmetry of the CD_4 molecule where there are 4 possible deuterium atoms to exchange in R6 whereas only one such deuterium atom is present in the CH_3D molecule. Due to the consistency in the ratio of the reaction rate constants, the secondary KIE may not be as important in affecting the reaction rate constant, unlike the primary KIE, in which the results had been presented previously in Table 5.11.

5.3.3 Summary for $CD_4 + CD_3 \longrightarrow CD_3 + CD_4$

In the test of TST/SCT (MI) and TST/LCT (MI) on the RD PES reported by Remmert[110] for R6, similar results as reaction R5 was obtained. At low temperatures, TST was inadequate to calculate the reaction rate constants for R6 due to the lack of accounting of quantum effects even though quantum effects were less prominent than R4 due to the much heavier deuterium atom that was transferred. Also, across the entire temperature range of 250K–2500K, TST/LCT (MI) reaction rate constants were lower than TST/SCT (MI) due to the

smaller reaction path curvature since the distance between the reactant and product valleys were larger. Both TST/LCT (MI) and TST/SCT (MI) have good agreement to QRS[110] and experimental data,[157] with TST/SCT (MI) having excellent agreement with QRS even at low temperatures. Comparison between R6 and R5 also showed that the secondary KIE were much less important in affecting the quantum effects and their only contribution to the reaction were in the inclusion of the vibrational frequencies as spectator modes in the construction of the RD PES. The differences between the reaction rate constants of reaction R5 and R6 were due to symmetry considerations.

5.4 Conclusion for Hydrogen Exchange Reactions

In the tests of TST/SCT (MI) and TST/LCT (MI) methods on available RD PESs for R4–R6,[110] quantum tunnelling was found to be important in these exchange reactions especially at low temperatures, and decreases with increasing temperature. In contrast to reactions studied in the previous chapter, TST/SCT (MI) reaction R4 did not yield excellent agreement to QRS results. This could be due to the MEP being a less effective tunnelling path in a reaction that had a larger reaction path curvature. However, TST/LCT (MI) recovered less quantum tunnelling effects than TST/SCT (MI) when extreme corner-cutting effects were taken into consideration. The lack of agreement between TST/LCT (MI) and QRS might be due to the RD nature of the PES which increased the barrier height of the effective tunnelling potential energy curve along the LCT tunnelling paths which lay on the concave side of the MEP. Intermediate tunnelling paths may also be further studied using the LAT method to obtain better agreement to QRS. TST/SCT (MI) results for R5 showed that primary KIEs were important for reaction R4 where the reaction rate constants were significantly reduced when the exchanged hydrogen atom was substituted with the much heavier deuterium atom. Secondary KIEs were found to be less significant for reaction R5.

Chapter 6

Conclusion

The test of the Transition State Theory with multi-dimensional tunnelling methods with quantum reactive scattering on the same constructed potential energy surfaces had been extended to more complicated polyatomic reactions over a wider temperature range. In this thesis, previously constructed reduced dimensionality PESs (RD PES) were used,[109,110,112,113] such that TST/MT were applied to pseudo diatom-atom reacting systems.

In order to adapt to the RD nature of the PES and to have more control over the intermediate steps in the calculations, the RDPOLY code was written to perform the TST/MT calculations. Chapter 3 presented the description of RDPOLY and its test against the available code POLYRATE.[116] Such calculations were similar to a previous study conducted which tested the TST/MT methods against accurate QRS calculations on the same PESs for diatom-atom reactions,[86] but increased the number and complexity of reactions to the current list of reactions tested.

The two main groups of reactions studied were the hydrogen abstraction and hydrogen exchange reactions. The results for the hydrogen abstraction reactions were presented in Chapter 4. The reactions studied in this set of reactions were $CH_4 + H$, $C_2H_6 + H$ and cyc-$C_3H_6 + H$. TST with zero- and small-curvature tunnelling (TST/ZCT and TST/SCT respectively) were applied to these reactions to study their reaction rate constants. For

all 3 reactions, it was found that implementation of the mapped interpolation (MI) method improved the agreement of the TST/ZCT and TST/SCT reaction rate constants with respect to QRS ones and experimental data. TST/SCT (MI) had excellent agreement to QRS due to the small reaction path curvature of the RD PES for these reactions.

In Chapter 5, the results for the hydrogen exchange reactions were presented. For reactions with a heavy-light-heavy (HLH) mass combination, the larger reaction path curvature rendered the TST/SCT (MI) results less adequate to reproduce the QRS reaction rate constants on the same surface. The $CH_4 + CH_3$ hydrogen exchange reaction was used as an example where a light hydrogen atom was exchanged between two heavy methyl groups. Due to the larger reaction path curvature, TST/SCT (MI) results for the $CH_4 + CH_3$ reaction underestimated the QRS reaction rate constants as it did not sufficiently account for corner-cutting effects. However, implementation of the TST with large-curvature tunnelling with the mapped interpolation (TST/LCT (MI)) method which took into account extreme corner-cutting effects accounted for less quantum tunnelling effects than TST/SCT (MI). This could be due to the intermediate reaction path curvature of the reaction. More work could be carried out in the future to search for a tunnelling path using the LAT method[156] which would be an intermediate between the MEP used in TST/SCT (MI) calculations and the straight-line LCT tunnelling paths in TST/LCT (MI) calculations to improve the agreement to QRS results. The lower TST/LCT (MI) reaction rate constants might also be due to the inclusion of the ZPEs of the spectator modes in the RD PESs, which could affect RD TST/LCT (MI) calculations when comparing to full-dimensional TST/LCT (MI) calculations more than RD QRS calculations when comparing to full-dimensional QRS calculations.

The primary kinetic isotope effect (KIE) was also studied for $CH_4 + CH_3$ using the reaction $CH_3D + CH_3$ where the exchanged hydrogen atom was substituted with a deuterium atom. It was found that the primary KIE was significant and important in altering the reaction rate constants since the deuterium atom was much heavier than a hydrogen atom.

This led to a reduction in the reaction path curvature and tunnelling contributions since the deuterium atom, being heavier, was less effective in tunnelling. The secondary KIE for the reaction $CH_3D + CH_3$ was studied using the reaction $CD_4 + CD_3$ where the hydrogen atoms not directly involved in the reaction were substituted with deuterium atoms. It was found that secondary KIE was much less significant and its contribution to the reaction rate constants was attributed to the vibrational frequencies of the spectator modes included as ZPEs in the construction of the RD PES.

Bibliography

[1] Truhlar, D. G.; Garrett, B. C. Variational Transition State Theory. *Annual Review of Physical Chemistry* **1984**, *35*, 159–189.

[2] Garrett, B. C. Perspective on "The Transition State Method". *Theoretical Chemistry Accounts* **2000**, *103*, 200–204.

[3] Pechukas, P. Transition State Theory. *Annual Review of Physical Chemistry* **1981**, *32*, 159–177.

[4] Eyring, H. The Activated Complex in Chemical Reactions. *Journal of Chemical Physics* **1935**, *3*, 107–115.

[5] Eyring, H. The Theory of Absolute Reaction Rates. *Transactions of the Faraday Society* **1938**, *34*, 41–48.

[6] Laidler, K. J.; King, M. C. The Development of Transition-State Theory. *Journal of Physical Chemistry* **1983**, *87*, 2657–2664.

[7] Evans, M. G.; Polanyi, M. Some Applications of the Transition State Method to the Calculation of Reaction Velocities, Especially in Solution. *Transactions of the Faraday Society* **1935**, *31*, 875–894.

[8] Wigner, E. The Transition State Method. *Transactions of the Faraday Society* **1938**, *34*, 29–41.

[9] Horiuti, J. On the Statistical Mechanical Treatment of the Absolute Rate of Chemical Reaction. *Bulletin of the Chemical Society of Japan* **1938**, *13*, 210–216.

[10] Nakamura, T. Dividing Surface in Transition State Theory of Reaction Rates: Note on Horiuti's Paper, "On the Statistical Mechanical Treatment of the Absolute Rate of Chemical Reaction". *Journal of the Research Institute for Catalysis Hokkaido University* **1980**, *28*, 293–304.

[11] Hirschfelder, J.; Eyring, H.; Topley, B. Reactions Involving Hydrogen Molecules and Atoms. *Journal of Chemical Physics* **1936**, *4*, 170–177.

[12] Wheeler, A.; Topley, B.; Eyring, H. The Absolute Rates of Reaction of Hydrogen with the Halogens. *Journal of Chemical Physics* **1936**, *4*, 178–187.

[13] Altar, W.; Eyring, H. Absolute Rates of Four-Atom Reactions. *Journal of Chemical Physics* **1936**, *4*, 661–673.

[14] Gershinowitz, H.; Eyring, H. The Theory of Trimolecular Reactions. *Journal of the American Chemical Society* **1935**, *57*, 985–991.

[15] Farkas, A.; Farkas, L. Experiments on Heavy Hydrogen. V. The Elementary Reactions of Light and Heavy Hydrogen. The Thermal Conversion of Ortho-Deuterium and the Interaction of Hydrogen and Deuterium. *Proceedings of the Royal Society of London. Series A, Mathematical and Physical Sciences* **1935**, *152*, 124–151.

[16] Rodebush, W. H.; Klingelhoefer, J. W. C. Atomic Chlorine and its Reaction with Hydrogen. *Journal of the American Chemical Society* **1933**, *55*, 130–142.

[17] Bonner, W. D.; Gore, W. L.; Yost, D. M. The Thermal Reaction Between Gaseous Iodine Monochloride and Hydrogen. *Journal of the American Chemical Society* **1935**, *57*, 2723–2724.

[18] Miller, W. H. Spiers Memorial Lecture Quantum and Semiclassical Theory of Chemical Reaction Rates. *Faraday Discussions* **1998**, *110*, 1–21.

[19] Porter, G. Kinetics of Reactions in Gases. *Annual Review of Physical Chemistry* **1956**, *7*, 207–230.

[20] Pechukas, P.; McLafferty, F. J. On Transition-State Theory and the Classical Mechanics of Collinear Collisions. *Journal of Chemical Physics* **1973**, *58*, 1622–1625.

[21] Stern, M. J.; Persky, A.; Klein, F. S. Force Field and Tunneling Effects in the H−H−Cl Reaction System. Determination from Kinetic-Isotope-Effect Measurements. *Journal of Chemical Physics* **1973**, *58*, 5697–5706.

[22] Bell, R. P. The Application of Quantum Mechanics to Chemical Kinetics. *Proceedings of the Royal Society of London. Series A, Containing Papers of a Mathematical and Physical Character* **1933**, *139*, 466–474.

[23] Miller, W. H. Quantum Mechanical Transition State Theory and a New Semiclassical Model for Reaction Rate Constants. *Journal of Chemical Physics* **1974**, *61*, 1823–1834.

[24] Bell, R. P. Quantum Mechanical Effects in Reactions Involving Hydrogen. *Proceedings of the Royal Society of London. Series A, Mathematical and Physical Sciences* **1935**, *148*, 241–250.

[25] Bell, R. P. Exact and Approximate Expressions for the Permeability of Potential Barriers to Light Particles. *Proceedings of the Royal Society of London. Series A, Mathematical and Physical Sciences* **1937**, *158*, 128–136.

[26] Truhlar, D. G.; Garrett, B. C. Variational Transition-State Theory. *Accounts of Chemical Research* **1980**, *13*, 440–448.

[27] Hansen, N. F.; Andersen, H. C. A New Formulation of Quantum Transition State Theory for Adiabatic Rate Constants. *Journal of Chemical Physics* **1994**, *101*, 6032–6037.

[28] Tromp, J. W.; Miller, W. H. New Approach to Quantum Mechanical Transition-State Theory. *Journal of Physical Chemistry* **1986**, *90*, 3482–3485.

[29] Miller, W. H.; Schwartz, S. D.; Tromp, J. W. Quantum Mechanical Rate Constants for Bimolecular Reactions. *Journal of Chemical Physics* **1983**, *79*, 4889–4898.

[30] Lewars, E. G. *Computational Chemistry: Introduction to the Theory and Applications of Molecular and Quantum Mechanics*; Springer: Dordrecht, 2011; pp 175–390.

[31] Siegbahn, P.; Liu, B. An Accurate Three-Dimensional Potential Energy Surface for H_3. *Journal of Chemical Physics* **1978**, *68*, 2457–2465.

[32] Keck, J. C. Variational Theory of Chemical Reaction Rates Applied to Three-Body Recombinations. *Journal of Chemical Physics* **1960**, *32*, 1035–1050.

[33] Garrett, B. C.; Truhlar, D. G. Generalized Transition State Theory. Quantum Effects for Collinear Reactions of Hydrogen Molecules and Isotopically Substituted Hydrogen Molecules. *Journal of Physical Chemistry* **1979**, *83*, 1079–1112.

[34] Maczek, A. *Statistical Thermodynamics*; Oxford University Press: Oxford, 2005; pp 35–69.

[35] McQuarrie, D. A.; Simon, J. D. *Physical Chemistry: A Molecular Approach*; University Science Books: Sausalito, CA, 1997; pp 157–179.

[36] McQuarrie, D. A. *Quantum Chemistry*; University Science Books: Sausalito, CA, 2008; pp 97–114.

[37] Grätzel, M.; Infelta, P. *The Bases of Chemical Thermodynamics*; Universal: Boca Raton, FL, 2000; pp 388–401.

[38] Truhlar, D. G.; Isaacson, A. D.; Garrett, B. C. *Theory of Chemical Reaction Dynamics*; CRC Press: Boca Raton, FL, 1985; pp 65–137.

[39] Fernández-Ramos, A.; Ellingson, B. A.; Garrett, B. C.; Truhlar, D. G. *Reviews in Computational Chemistry*; Wiley-VCH: Hoboken, NJ, 2007; pp 125–232.

[40] Nyman, G.; Yu, H. Quantum Theory of Bimolecular Chemical Reactions. *Reports on Progress in Physics* **2000**, *63*, 1001–1059.

[41] Cao, J.; Voth, G. A. The Formulation of Quantum Statistical Mechanics Based on the Feynman Path Centroid Density. II. Dynamical Properties. *Journal of Chemical Physics* **1994**, *100*, 5106–5117.

[42] Jang, S.; Voth, G. A. A Derivation of Centroid Molecular Dynamics and Other Approximate Time Evolution Methods for Path Integral Centroid Variables. *Journal of Chemical Physics* **1999**, *111*, 2371–2384.

[43] Craig, I. R.; Manolopoulos, D. E. Quantum Statistics and Classical Mechanics: Real Time Correlation Functions from Ring Polymer Molecular Dynamics. *Journal of Chemical Physics* **2004**, *121*, 3368–3373.

[44] Craig, I. R.; Manolopoulos, D. E. Chemical Reaction Rates from Ring Polymer Molecular Dynamics. *Journal of Chemical Physics* **2005**, *122*, 084106.

[45] Craig, I. R.; Manolopoulos, D. E. A Refined Ring Polymer Molecular Dynamics Theory of Chemical Reaction Rates. *Journal of Chemical Physics* **2005**, *123*, 034102.

[46] Braams, B. J.; Manolopoulos, D. E. On the Short-Time Limit of Ring Polymer Molecular Dynamics. *Journal of Chemical Physics* **2006**, *125*, 124105.

[47] Miller, W. H. Semiclassical Limit of Quantum Mechanical Transition State Theory for Nonseparable Systems. *Journal of Chemical Physics* **1975**, *62*, 1899–1906.

[48] Miller, W. H. Semi-Classical Theory for Non-Separable Systems: Construction of "Good" Action-Angle Variables for Reaction Rate Constants. *Faraday Discussions of the Chemical Society* **1977**, *62*, 40–46.

[49] Miller, W. H.; Hernandez, R.; Handy, N. C.; Jayatilaka, D.; Willetts, A. *Ab Initio* Calculation of Anharmonic Constants for a Transition State, with Application to Semiclassical Transition State Tunneling Probabilities. *Chemical Physics Letters* **1990**, *172*, 62–68.

[50] Wagner, A. F. Improved Multidimensional Semiclassical Tunneling Theory. *Journal of Physical Chemistry A* **2013**, *117*, 13089–13100.

[51] Meyer, H.-D.; Manthe, U.; Cederbaum, L. S. The Multi-Configurational Time-Dependent Hartree Approach. *Chemical Physics Letters* **1990**, *165*, 73–78.

[52] Manthe, U.; Meyer, H.-D.; Cederbaum, L. S. Wave-Packet Dynamics Within the Multiconfiguration Hartree Framework: General Aspects and Application to NOCl. *Journal of Chemical Physics* **1992**, *97*, 3199–3213.

[53] Meyer, H.-D.; Manthe, U.; Cederbaum, L. S. *Numerical Grid Methods and their Application to Schrödinger's Equation*; Kluwer Academic Publishers: Dordrecht, 1993; pp 141–152.

[54] Meyer, H.-D. *The Encyclopedia of Computational Chemistry*; John Wiley and Sons: Chichester, 1998; pp 3011–3018.

[55] Truhlar, D. G.; Garrett, B. C.; Klippenstein, S. J. Current Status of Transition-State Theory. *Journal of Physical Chemistry* **1996**, *100*, 12771–12800.

[56] Garrett, B. C.; Truhlar, D. G.; Grev, R. S.; Magnuson, A. W. Improved Treatment of Threshold Contributions in Variational Transition-State Theory. *Journal of Physical Chemistry* **1980**, *84*, 1730–1748.

[57] Dunitz, J. D. Chemical Reaction Paths. *Philosophical Transactions of the Royal Society of London. Series B, Biological Sciences* **1975**, *272*, 99–108.

[58] Truhlar, D. G.; Kuppermann, A. Exact Tunneling Calculations. *Journal of the American Chemical Society* **1971**, *93*, 1840–1851.

[59] Garrett, B. C.; Truhlar, D. G. Improved Canonical Variational Theory for Chemical Reaction Rates. Classical Mechanical Theory and Applications to Collinear Reactions. *Journal of Physical Chemistry* **1980**, *84*, 805–812.

[60] Marcus, R. A. Analytical Mechanics of Chemical Reactions. IV. Classical Mechanics of Reactions in Two Dimensions. *Journal of Chemical Physics* **1968**, *49*, 2617–2631.

[61] Truhlar, D. G.; Isaacson, A. D.; Skodje, R. T.; Garrett, B. C. Incorporation of Quantum Effects in Generalized-Transition-State Theory. *Journal of Physical Chemistry* **1982**, *86*, 2252–2261.

[62] Garrett, B. C.; Truhlar, D. G. Generalized Transition State Theory Calculations for the Reactions $D + H_2$ and $H + D_2$ using an Accurate Potential Energy Surface: Explanation of the Kinetic Isotope Effect. *Journal of Chemical Physics* **1980**, *72*, 3460–3471.

[63] Miller, W. H.; Handy, N. C.; Adams, J. E. Reaction Path Hamiltonian for Polyatomic Molecules. *Journal of Chemical Physics* **1980**, *72*, 99–112.

[64] Marcus, R. A. Local Approximation of Potential-Energy Surfaces by Surfaces Permitting Separation of Variables. *Journal of Chemical Physics* **1964**, *41*, 610–616.

[65] Marcus, R. A. Generalization of the Activated Complex Theory of Reaction Rates. I. Quantum Mechanical Treatment. *Journal of Chemical Physics* **1964**, *41*, 2614–2623.

[66] Marcus, R. A.; Coltrin, M. E. A New Tunneling Path for Reactions such as $H + H_2 \longrightarrow H_2 + H$. *Journal of Chemical Physics* **1977**, *67*, 2609–2613.

[67] Garrett, B. C.; Truhlar, D. G. Accuracy of Tunneling Corrections to Transition State Theory for Thermal Rate Constants of Atom Transfer Reactions. *Journal of Physical Chemistry* **1979**, *83*, 200–203.

[68] Skodje, R. T.; Truhlar, D. G.; Garrett, B. C. A General Small-Curvature Approximation for Transition-State-Theory Transmission Coefficients. *Journal of Physical Chemistry Letters* **1981**, *85*, 3019–3023.

[69] Skodje, R. T.; Truhlar, D. G.; Garrett, B. C. Vibrationally Adiabatic Models for Reactive Tunneling. *Journal of Chemical Physics* **1982**, *77*, 5955–5976.

[70] Marcus, R. A. On the Analytical Mechanics of Chemical Reactions. Quantum Mechanics of Linear Collisions. *Journal of Chemical Physics* **1966**, *45*, 4493–4499.

[71] Griffiths, D. J. *Introduction to Quantum Mechanics*; Pearson Education: Upper Saddle River, NJ, 2005; pp 327–351.

[72] Lu, D.; Truong, T. N.; Melissas, V. S.; Lynch, G. C.; Liu, Y.; Garrett, B. C.; Steckler, R.; Isaacson, A. D.; Rai, S. N.; Hancock, G. C.; Lauderdale, J. G.; Joseph, T.; Truhlar, D. G. Polyrate 4: A New Version of a Computer Program for the Calculation of Chemical Reaction Rates for Polyatomics. *Computer Physics Communications* **1992**, *71*, 235–262.

[73] Garrett, B. C.; Truhlar, D. G. Reliable *Ab Initio* Calculation of a Chemical Reaction Rate and a Kinetic Isotope Effect: $H + H_2$ and $^2H + {}^2H_2$. *Proceedings of the National Academy of Sciences of the United States of America* **1979**, *76*, 4755–4759.

[74] Garrett, B. C.; Truhlar, D. G.; Grev, R. S. Application of Variational Transition-State Theory and the Unified Statistical Model to $H + Cl_2 \longrightarrow HCl + Cl$. *Journal of Physical Chemistry* **1980**, *84*, 1749–1752.

[75] Bondi, D. K.; Clary, D. C.; Connor, J. N. L.; Garrett, B. C.; Truhlar, D. G. Kinetic Isotope Effects in the $Mu + H_2$ and $Mu + D_2$ Reactions: Accurate Quantum Calculations for the Collinear Reactions and Variational Transition State Theory Predictions for One and Three Dimensions. *Journal of Chemical Physics* **1982**, *76*, 4986–4995.

[76] Isaacson, A. D.; Truhlar, D. G. Polyatomic Canonical Variational Theory for Chemical Reaction Rates. Separable-Mode Formalism with Application to $OH + H_2 \longrightarrow H_2O + H$. *Journal of Chemical Physics* **1982**, *76*, 1380–1391.

[77] Garrett, B. C.; Truhlar, D. G.; Wagner, A. F.; Dunning, T. H., Jr. Variational Transition State Theory and Tunneling for a Heavy-Light-Heavy Reaction Using an *Ab Initio* Potential Energy Surface. $^{37}Cl + H(D)\ ^{35}Cl \longrightarrow H(D)\ ^{37}Cl + {}^{35}Cl$. *Journal of Chemical Physics* **1983**, *78*, 4400–4413.

[78] Ovchinnikova, M. Y. The Tunneling Dynamics of the Low Temperature H Exchange Reactions. *Chemical Physics* **1979**, *36*, 85–95.

[79] Bondi, D. K.; Connor, J. N. L.; Garrett, B. C.; Truhlar, D. G. Test of Variational Transition State Theory with a Large-Curvature Tunneling Approximation Against Accurate Quantal Reaction Probabilities and Rate Coefficients for Three Collinear Reactions with Large Reaction-Path Curvature: $Cl + HCl$, $Cl + DCl$, $Cl + MuCl$. *Journal of Chemical Physics* **1983**, *78*, 5981–5989.

[80] Babamov, V. K.; Marcus, R. A. Dynamics of Hydrogen Atom and Proton Transfer Reactions. Symmetric Case. *Journal of Chemical Physics* **1981**, *74*, 1790–1798.

[81] Garrett, B. C.; Truhlar, D. G. A Least-Action Variational Method for Calculating Multidimensional Tunneling Probabilities for Chemical Reactions. *Journal of Chemical Physics* **1983**, *79*, 4931–4938.

[82] Blais, N. C.; Truhlar, D. G.; Garrett, B. C. Temperature Dependence of the Activation Energy: $D + H_2$. *Journal of Chemical Physics* **1982**, *76*, 2768–2770.

[83] Garrett, B. C.; Abusalbi, N.; Kouri, D. J.; Truhlar, D. G. Test of Variational Transition State Theory and the Least-Action Approximation for Multidimensional Tunneling Probabilities Against Accurate Quantal Rate Constants for a Collinear Reaction Involving Tunneling into an Excited State. *Journal of Chemical Physics* **1985**, *83*, 2252–2258.

[84] Garrett, B. C.; Joseph, T.; Truong, T. N.; Truhlar, D. G. Application of the Large-Curvature Tunneling Approximation to Polyatomic Molecules: Abstraction of H or D by Methyl Radical. *Chemical Physics* **1989**, *136*, 271–283.

[85] Liu, Y.; Lu, D.; Gonzalez-Lafont, A.; Truhlar, D. G.; Garrett, B. C. Direct Dynamics Calculation of the Kinetic Isotope Effect for an Organic Hydrogen-Transfer Reaction, Including Corner-Cutting Tunneling in 21 Dimensions. *Journal of the American Chemical Society* **1993**, *115*, 7806–7817.

[86] Allison, T. C.; Truhlar, D. G. *Modern Methods for Multidimensional Dynamics Computations in Chemistry*; World Scientific: Singapore, 1998; pp 618–712.

[87] Fernández-Ramos, A.; Truhlar, D. G. Improved Algorithm for Corner-Cutting Tunneling Calculations. *Journal of Chemical Physics* **2001**, *114*, 1491–1496.

[88] Joseph, T.; Steckler, R.; Truhlar, D. G. A New Potential Energy Surface for the $CH_3 + H_2 \longleftrightarrow CH_4 + H$ Reaction: Calibration and Calculations of Rate Constants and Kinetic Isotope Effects by Variational Transition State Theory and Semiclassical Tunneling Calculations. *Journal of Chemical Physics* **1987**, *87*, 7036–7049.

[89] Kim, Y. Dynamics and Kinetic Isotope Effect for the Double Proton Transfer in Formamidine Monohydrated Complex Using Direct Semiempirical Dynamics Calculation. *Journal of Physical Chemistry A* **1998**, *102*, 3025–3036.

[90] Pu, J.; Truhlar, D. G. Tests of Potential Energy Surfaces for $H + CH_4 \longleftrightarrow CH_3 + H_2$: Deuterium and Muonium Kinetic Isotope Effects for the Forward and Reverse Reaction. *Journal of Chemical Physics* **2002**, *117*, 10675–10687.

[91] Lin, H.; Pu, J.; Albu, T. V.; Truhlar, D. G. Efficient Molecular Mechanics for Chemical Reactions: Multiconfiguration Molecular Mechanics Using Partial Electronic Structure Hessians. *Journal of Physical Chemistry A* **2004**, *108*, 4112–4124.

[92] Lin, H.; Ellingson, B. A.; Pu, J.; Truhlar, D. G. Temperature Dependence of Carbon-13 Kinetic Isotope Effects of Importance to Global Climate Change. *Journal of the American Chemical Society* **2005**, *127*, 2830–2831.

[93] Pu, J.; Gao, J.; Truhlar, D. G. Multidimensional Tunneling, Recrossing, and the Transmission Coefficient for Enzymatic Reactions. *Chemical Reviews* **2006**, *106*, 3140–3169.

[94] Kim, Y.; Marenich, A. V.; Zheng, J.; Kim, K. H.; Kołodziejska-Huben, M.; Rostkowski, M.; Paneth, P.; Truhlar, D. G. Mechanistic Analysis of the Base-Catalyzed HF Elimination from 4-Fluoro-4-(4′-nitrophenyl)butane-2-one Based on Liquid-Phase Kinetic Isotope Effects Calculated by Dynamics Modeling with Multidimensional Tunneling. *Journal of Chemical Theory and Computation* **2009**, *5*, 59–67.

[95] Yu, T.; Zheng, J.; Truhlar, D. G. Multipath Variational Transition State Theory: Rate Constant of the 1,4-Hydrogen Shift Isomerization of the 2-Cyclohexylethyl Radical. *Journal of Physical Chemistry A* **2012**, *116*, 297–308.

[96] Clary, D. C. Four-Atom Reaction Dynamics. *Journal of Physical Chemistry* **1994**, *98*, 10678–10688.

[97] Althorpe, S. C.; Clary, D. C. Quantum Scattering Calculations on Chemical Reactions. *Annual Review of Physical Chemistry* **2003**, *54*, 493–529.

[98] Czakó, G.; Bowman, J. M. Accurate *Ab Initio* Potential Energy Surface, Thermochemistry, and Dynamics of the $Cl(^2P,^2P_{3/2}) + CH_4 \longrightarrow HCl + CH_3$ and $H + CH_3Cl$ Reactions. *Journal of Chemical Physics* **2012**, *136*, 044307.

[99] Welsch, R.; Manthe, U. Fast Shepard Interpolation on Graphics Processing Units: Potential Energy Surfaces and Dynamics for $H + CH_4 \longrightarrow H_2 + CH_3$. *Journal of Chemical Physics* **2013**, *138*, 164118.

[100] Welsch, R.; Manthe, U. Full-Dimensional and Reduced-Dimensional Calculations of Initial State-Selected Reaction Probabilities Studying the $H + CH_4 \longrightarrow H_2 + CH_3$ Reaction on a Neural Network PES. *Journal of Chemical Physics* **2015**, *142*, 064309.

[101] Clary, D. C. Quantum Theory of Chemical Reaction Dynamics. *Science* **1998**, *279*, 1879–1882.

[102] Bowman, J. M. Reduced Dimensionality Theory of Quantum Reactive Scattering. *Journal of Physical Chemistry* **1991**, *95*, 4960–4968.

[103] Ohsaki, A.; Nakamura, H. Hyperspherical Coordinate Approach to Atom-Diatom Chemical Reactions in the Sudden and Adiabatic Approximations. *Physics Reports* **1990**, *187*, 1–62.

[104] Brooks, A. N.; Clary, D. C. Application of Hyperspherical Coordinates to Four-Atom Reactive Scattering: $H_2 + CN \longrightarrow H + HCN$. *Journal of Chemical Physics* **1990**, *92*, 4178–4190.

[105] Bowman, J. M. Overview of Reduced Dimensionality Quantum Approaches to Reactive Scattering. *Theoretical Chemistry Accounts* **2002**, *108*, 125–133.

[106] Remmert, S. M.; Banks, S. T.; Clary, D. C. Reduced Dimensionality Quantum Dynamics of $CH_3 + CH_4 \longrightarrow CH_4 + CH_3$: Symmetric Hydrogen Exchange on an *Ab Initio* Potential. *Journal of Physical Chemistry A* **2009**, *113*, 4255–4264.

[107] Kerkeni, B.; Clary, D. C. *Ab Initio* Rate Constants from Hyperspherical Quantum Scattering: Application to $H + CH_4 \longrightarrow H_2 + CH_3$. *Journal of Chemical Physics* **2004**, *120*, 2308–2318.

[108] Walker, R. B.; Hayes, E. F. *The Theory of Chemical Reaction Dynamics*; Reidel: Dordrecht, 1986; pp 105–135.

[109] Kerkeni, B.; Clary, D. C. *Ab Initio* Rate Constants from Hyperspherical Quantum Scattering: Application to $H + C_2H_6$ and $H + CH_3OH$. *Journal of Chemical Physics* **2004**, *121*, 6809–6821.

[110] Remmert, S. M. Reduced Dimensionality Quantum Dynamics of Chemical Reactions. DPhil Thesis, University of Oxford, 2011.

[111] Banks, S. T.; Clary, D. C. Chemical Reaction Surface Vibrational Frequencies Evaluated in Curvilinear Internal Coordinates: Application to $H + CH_4 \rightleftharpoons H_2 + CH_3$. *Journal of Chemical Physics* **2009**, *130*, 024106.

[112] Banks, S. T.; Tautermann, C. S.; Remmert, S. M.; Clary, D. C. An Improved Treatment of Spectator Mode Vibrations in Reduced Dimensional Quantum Dynamics:

Application to the Hydrogen Abstraction Reactions $\mu + CH_4$, $H + CH_4$, $D + CH_4$, and $CH_3 + CH_4$. *Journal of Chemical Physics* **2009**, *131*, 044111.

[113] Shan, X.; Clary, D. C. Quantum Dynamics of the Abstraction Reaction of H with Cyclopropane. *Journal of Physical Chemistry A* **2014**, *118*, 10134–10143.

[114] Stechel, E. B.; Walker, R. B.; Light, J. C. *R*-matrix Solution of Coupled Equations for Inelastic Scattering. *Journal of Chemical Physics* **1978**, *69*, 3518–3531.

[115] Nyman, G.; Clary, D. C. Quantum Scattering Calculations on the $CH_4 + OH \longrightarrow CH_3 + H_2O$ Reaction. *Journal of Chemical Physics* **1994**, *101*, 5756–5771.

[116] Zheng, J. et al. POLYRATE, version 2010-A; University of Minnesota: Minneapolis, 2010.

[117] Maczek, A. *Statistical Thermodynamics*; Oxford University Press: Oxford, 2005; pp 7–9.

[118] McLauchlan, K. A. *Molecular Physical Chemistry*; Royal Society of Chemistry: Cambridge, 2004; pp 30–58.

[119] Fukui, K. The Path of Chemical Reactions - The IRC Approach. *Accounts of Chemical Research* **1981**, *14*, 363–368.

[120] Jackels, C. F.; Gu, Z.; Truhlar, D. G. Reaction-Path Potential and Vibrational Frequencies in Terms of Curvilinear Internal Coordinates. *Journal of Chemical Physics* **1995**, *102*, 3188–3201.

[121] Lu, D.; Truhlar, D. G. Bond-Distance and Bond-Angle Constraints in Reaction-Path Dynamics Calculations. *Journal of Chemical Physics* **1993**, *99*, 2723–2738.

[122] Wilson, E. B., Jr.; Decius, J. C.; Cross, P. C. *Molecular Vibrations: The Theory of Infrared and Raman Vibrational Spectra*; Dover: New York, 1980; pp 54–76.

[123] Miller, W. H.; Ruf, B. A.; Chang, Y. A Diabatic Reaction Path Hamiltonian. *Journal of Chemical Physics* **1988**, *89*, 6298–6304.

[124] Corchado, J. C.; Coitiño, E. L.; Chuang, Y.; Fast, P. L.; Truhlar, D. G. Interpolated Variational Transition-State Theory by Mapping. *Journal of Physical Chemistry A* **1998**, *102*, 2424–2438.

[125] Brown, R. L. A Method of Calculating Tunneling Corrections for Eckart Potential Barriers. *Journal of Research of the National Bureau of Standards* **1981**, *86*, 357–359.

[126] Pu, J.; Truhlar, D. G. Validation of Variational Transition State Theory with Multidimensional Tunneling Contributions Against Accurate Quantum Mechanical Dynamics for $H + CH_4 \longrightarrow H_2 + CH_3$ in an Extended Temperature Interval. *Journal of Chemical Physics* **2002**, *117*, 1479–1481.

[127] Fernández-Ramos, A.; Truhlar, D. G. A New Algorithm for Efficient Direct Dynamics Calculations of Large-Curvature Tunneling and Its Application to Radical Reactions with 9-15 Atoms. *Journal of Chemical Theory and Computation* **2005**, *1*, 1063–1078.

[128] Mathematica, version 9.0; Wolfram Research: Champaign, IL, 2004.

[129] Frisch, M. J. et al. Gaussian 09, Revision E.01. Gaussian Inc., Wallingford CT, 2009.

[130] Werner, H.-J. et al. MOLPRO, version 2015.1; a package of *ab initio* programs; see http://www.molpro.net; Cardiff, UK, 2015.

[131] Dunning, T. H., Jr. Gaussian Basis Sets for use in Correlated Molecular Calculations. I. The Atoms Boron Through Neon and Hydrogen. *Journal of Chemical Physics* **1989**, *90*, 1007–1023.

[132] Adler, T. B.; Knizia, G.; Werner, H.-J. A Simple and Efficient CCSD(T)-F12 Approximation. *Journal of Chemical Physics* **2007**, *127*, 221106.

[133] Peterson, K. A.; Adler, T. B.; Werner, H.-J. Systematically Convergent Basis Sets for Explicitly Correlated Wavefunctions: The Atoms H, He, B-Ne, and Al-Ar. *Journal of Chemical Physics* **2008**, *128*, 084102.

[134] Gardiner, W. C., Jr. *Gas-Phase Combustion Chemistry*; Springer: Dordrecht, 2000; pp 138–141.

[135] Kurylo, M. J.; Hollinden, G. A.; Timmons, R. B. ESR Study of the Kinetic Isotope Effect in the Reaction of H and D Atoms with CH_4. *Journal of Chemical Physics* **1970**, *52*, 1778–1781.

[136] Sutherland, J. W.; Su, M.-C.; Michael, J. V. Rate Constants for $H + CH_4$, $CH_3 + H_2$, and CH_4 Dissociation at High Temperature. *International Journal of Chemical Kinetics* **2001**, *33*, 669–684.

[137] Arai, H.; Nagai, S.; Matsuda, K.; Hatada, M. Effect of Irradiation Temperature on the Radiolysis of Methane. *Radiation Physics and Chemistry* **1981**, *17*, 151–157.

[138] Nyman, G.; van Harrevelt, R.; Manthe, U. Thermochemistry and Accurate Quantum Reaction Rate Calculations for H_2/HD/$D_2 + CH_3$. *Journal of Physical Chemistry A* **2007**, *111*, 10331–10337.

[139] van Harrevelt, R.; Nyman, G.; Manthe, U. Accurate Quantum Calculations of the Reaction Rates for H/D $+ CH_4$. *Journal of Chemical Physics* **2007**, *126*, 084303.

[140] Takayanagi, T. Reduced Dimensionality Calculations of Quantum Reactive Scattering for the $H + CH_4 \longrightarrow H_2 + CH_3$ Reaction. *Journal of Chemical Physics* **1996**, *104*, 2237–2242.

[141] Wang, M. L.; Li, Y.; Zhang, J. Z. H.; Zhang, D. H. Application of Semirigid Vibrating Rotor Target Model to Reaction of $H + CH_4 \longrightarrow CH_3 + H_2$. *Journal of Chemical Physics* **2000**, *113*, 1802–1806.

[142] Schiffel, G.; Manthe, U. Quantum Dynamics of the $H + CH_4 \longrightarrow H_2 + CH_3$ Reaction in Curvilinear Coordinates: Full-Dimensional and Reduced Dimensional Calculations of Reaction Rates. *Journal of Chemical Physics* **2010**, *132*, 084103.

[143] Wang, D. A Time-Dependent Quantum Dynamics Study of the $H_2 + CH_3 \longrightarrow H + CH_4$ Reaction. *Journal of Chemical Physics* **2002**, *117*, 9806–9810.

[144] Kurylo, M. J.; Timmons, R. B. ESR Study of the Kinetics of the Reaction of H Atoms with Methane. *Journal of Chemical Physics* **1969**, *50*, 5076–5082.

[145] Greene, S. M.; Shan, X.; Clary, D. C. Reduced-Dimensionality Semiclassical Transition State Theory: Application to Hydrogen Atom Abstraction and Exchange Reactions of Hydrocarbons. *Journal of Physical Chemistry A* **2015**, *119*, 12015–12027.

[146] Bryukov, M. G.; Slagle, I. R.; Knyazev, V. D. Kinetics of Reactions of H Atoms with Ethane and Chlorinated Ethanes. *Journal of Physical Chemistry A* **2001**, *105*, 6900–6909.

[147] Jones, D.; Morgan, P. A.; Purnell, J. H. Mass Spectrometric Study of the Reaction of Hydrogen Atoms with Ethane. *Journal of the Chemical Society, Faraday Transactions 1: Physical Chemistry in Condensed Phases* **1977**, *73*, 1311–1318.

[148] Arnold, P. A.; Carpenter, B. K. Computational Studies on the Ring Openings of Cyclopropyl Radical and Cyclopropyl Cation. *Chemical Physics Letters* **2000**, *328*, 90–96.

[149] Greig, G.; Thynne, J. C. J. Reactions of Cyclic Alkyl Radicals. Part 2. – Photolysis of Cyclopropane Carboxaldehyde. *Transactions of the Faraday Society* **1967**, *63*, 1369–1374.

[150] Oh, C. Y.; Shin, S. K.; Kim, H. L.; Park, C. R. Photodissociation of Cyclopropyl Cyanide at 193 nm. *Chemical Physics Letters* **2002**, *363*, 404–408.

[151] Marshall, R. M.; Purnell, H.; Satchell, P. W. Reaction of Hydrogen Atoms with Cyclopropane in the Temperature Range from 628 to 779K. *Journal of the Chemical Society, Faraday Transactions 1: Physical Chemistry in Condensed Phases* **1984**, *80*, 2395–2403.

[152] Marshall, R. M.; Purnell, H.; Sheppard, A. Reaction of Hydrogen Atoms with Cyclopropane in the Temperature Range 358-550K. *Journal of the Chemical Society, Faraday Transactions 2: Molecular and Chemical Physics* **1986**, *82*, 929–935.

[153] Truhlar, D. G.; Gordon, M. S. From Force Fields to Dynamics: Classical and Quantal Paths. *Science* **1990**, *249*, 491–498.

[154] Kerr, J. A.; Parsonage, M. J. *Evaluated Kinetic Data on Gas Phase Hydrogen Transfer Reactions of Methyl Radicals*; Butterworths: London, 1976.

[155] Arthur, N. L.; Bell, T. N. An Evaluation of the Kinetic Data for Hydrogen Abstraction from Silanes in the Gas Phase. *Reviews on Chemical Intermediates* **1978**, *2*, 37–74.

[156] Meana-Pañeda, R.; Truhlar, D. G.; Fernández-Ramos, A. Least-Action Tunneling Transmission Coefficient for Polyatomic Reactions. *Journal of Chemical Theory and Computation* **2010**, *6*, 6–17.

[157] Creak, G. A.; Dainton, F. S.; Ivin, K. J. Kinetics of the Exchange Reaction $CD_3 + CD_4 \longrightarrow CD_4 + CD_3$ using ^{14}C as Tracer. *Transactions of the Faraday Society* **1962**, *58*, 326–332.